

Laser Interference Lithography

Micropatterning of Polymer Surface for Cell Adhesion

Dissertation

zur Erlangung des ingenieurwissenschaftlichen Doktorgrades
der Naturwissenschaftlich-Technischen Fakultät III
Chemie, Pharmazie, Bio- und Werkstoffwissenschaften
der Universität des Saarlandes



vorgelegt von

Fayou Yu

Saarbrücken 2006

Tag des Kolloquiums: 12.06.2006

Dekan: Prof. Dr. K. Hegetschweiler

Berichterstatter: Prof. Dr. F. Mücklich
Prof. Dr. C.-M. Lehr

Content

<u>Acknowledgement.....</u>	<u>4</u>
<u>Kurzzusammenfassung.....</u>	<u>8</u>
<u>Abstract.....</u>	<u>10</u>
<u>1 Introduction.....</u>	<u>12</u>
1.1 Tasks of this work	15
<u>2 Fundamentals</u>	<u>17</u>
2.1 Laser-material interactions	17
2.1.1 Light propagation	17
2.1.2 Laser-metal interactions	18
2.1.3 Laser-insulator interactions	19
2.1.4 Evolution of temperature induced by laser	23
2.2 Laser ablation of polymers	24
2.2.1 Laser ablation mechanisms	24
2.2.2 Methods for studying laser ablation of polymers.....	27
2.2.3 Applications of laser ablation of polymers	29
2.3 Laser interference lithography	32
2.4 Cell-substrate interactions	35
2.4.1 Cell adhesion to extracellular matrix	35
2.4.2 Cell migration.....	37
2.4.3 Contact guidance	40
<u>3 Experimental.....</u>	<u>42</u>
3.1 Laser	42
3.1.1 Working principle of Nd:YAG laser	42

3.1.2	Construction of the Q-switched Nd:YAG laser	44
3.1.3	Properties of Nd:YAG laser used in this experiment.....	45
3.2	Materials.....	47
3.3	Characterization of the micropatterns and ablation craters.....	49
3.3.1	White light interferometry.....	49
3.3.2	Atomic force microscopy	49
3.3.3	Scanning electron microscopy	50
3.4	Laser ablation of polymers.....	50
3.4.1	Ablation curves	51
3.4.2	XPS analysis.....	51
3.4.3	Contact angle.....	52
3.4.4	Time of flight mass spectroscopy.....	53
3.5	Laser ablation of thin polymer solution	54
3.6	Laser interference lithography	55
3.7	Cell culturing on micropatterned polymer surfaces	56
3.7.1	Culturing of mouse fibroblasts on micropatterned Thermanox	56
3.7.2	Culturing of human pulmonary fibroblasts on patterned PET and TXL.....	58
3.7.3	Culturing human pulmonary fibroblasts on patterned PC.....	59
3.7.4	E-selectin expression.....	61
4	<u>Results.....</u>	<u>62</u>
4.1	Laser ablation polymer films.....	62
4.1.1	Laser ablation curves.....	62
4.1.2	Morphology of laser ablation craters	64
4.1.3	Contact angle.....	66
4.1.4	XPS analysis.....	67
4.2	Time of flight mass spectrometry.....	71
4.2.1	ToF-MS of PET and Thermanox	71
4.2.2	ToF-MS of PC.....	73
4.3	Laser ablation of thin polymer solution	75
4.4	Micropatterning of polymer surface by laser interference lithography.....	77
4.4.1	Micropatterning of poly(ethylene terephthalate) and Thermanox	77
4.4.2	Micropatterning of polycarbonate.....	83

4.5	Cell culturing on micropatterned polymer surface.....	86
4.5.1	Mouse fibroblasts cultured on micropatterned Thermanox	86
4.5.2	Human pulmonary fibroblasts cultured on patterned PET and TXL	89
4.5.3	Human pulmonary fibroblast cultured on patterned PC.....	90
4.6	Inflammation of cells on cultured polymer surface	93
4.6.1	E-selectin expression.....	93
4.6.2	Quantitative measurement of E-selectin expression by FACS	96
<u>5</u>	<u>Discussion</u>	<u>98</u>
5.1	Light excitation of PET and PC	98
5.1.1	Calculation of the molecular orbitals by using CAChe.....	98
5.2	Mechanisms of laser ablation of polymers.....	102
5.2.1	Significance of laser ablation curves.....	102
5.2.2	Surface topography	104
5.2.3	Chemical surface modification.....	105
5.2.4	Species emitted during laser ablation.....	106
5.2.5	Evidence of photochemical laser ablation of polymers	107
5.2.6	Summary of laser ablation mechanisms and processes.....	111
5.3	Laser interference lithography	112
5.3.1	Mechanism	112
5.3.2	Period and depth.....	113
5.3.3	Surface topography and chemical modification.....	115
5.4	Cell adhesion on micropatterned polymer surface.....	116
5.4.1	Mechanism of contact guidance.....	116
5.4.2	Cell inflammation on micropatterned polymer surface.....	119
<u>6</u>	<u>Conclusion and outlook</u>	<u>122</u>
<u>7</u>	<u>Reference</u>	<u>124</u>

Acknowledgement

This thesis was finished at Saarland University under supervision of Prof. Dr. Frank Mücklich from July 2001 to October 2004.

First of all, I am very grateful to Prof. Mücklich for giving me this opportunity to work on this interesting project in his group. I am forever indebted to Prof. Mücklich, not only for his considerable mentoring, invaluable suggestions and fruitful discussions, but also for his kindness and help whatever I need. This work would never have been possible if it were not for the freedom I was given to pursue my own research interests.

I want to express my special thanks to Prof. Dr. C-M. Lehr, Prof. Dr. U. Bakowsky and P. Li, Department of Biopharmaceutics and Pharmaceutical Technology, Saarland University, for their close and friendly cooperation on cell adhesion experiments and discussions. Prof. Bakowsky is also thankful for measuring the AFM photographs.

My special thanks go to Dr. H. Shen, Institute of New Materials, for the XPS measurements which were usually performed at weekend because of the special time requirements. I would like to thank Prof. J. Grotemeyer, University of Kiel, for giving me the opportunity to use his ToF-MS instrument and Mr. D. Walbrodt for performing the measurements. I thank Mr. S. Winter for measuring the contact angle and Ms. A. Kasten for doing GPC and UV/VIS measurements. I wish also to thank Prof Dr. X. Li, Jinan University, for his help to take AFM photographs and find necessary literature.

I'd also like to thank all of the colleagues at Department of Functional Materials who have made it such a great place to work. I have benefited greatly from their support and help. It's always my pleasure to remember the time we shared together.

In particular, I acknowledge German Federal Ministry for Education and Research (BMBF) who has sponsored my reseach work in large part under agreement number NMT-M2QN03149500-03N8020.

In the last, I would like to thank my parents for having given me the chance to carry out my studies and my wife and two daughters for their long-time patience, understanding and support. I dedicate this dissertation to them.

Abbreviation

AFM	atomic force microscopy
amu	atomic mass unit
ATR-FTIR	attenuated total reflection Fourier transformation infrared spectroscopy
BSA	bovine serum albumin
CLMS	confocal laser scanning microscopy
DMEM	Dulbecco's modified Eagle medium
ECM	extracellular matrix
ESCA	electron spectroscopy for chemical analysis
FACS	fluorescence activated cell sorting
FCS	fetal calf serum
FIP	focused ion beam
FITC	fluorescein isothiocyanate
FWHM	full width at half maximum
GC-MS	gas chromatography/mass spectroscopy
GPC	gel permeation chromatography
HBSS	Hanks' balanced salt solution
HOMO	highest occupied molecular orbital
HPF	human pulmonary fibroblast
IR	infrared light
LIL	laser interference lithography
LUMO	lowest unoccupied molecular orbital
MMA	methylmethacrylate
MO	molecular orbital
NUV	near ultraviolet

PBS	phosphate buffered saline
PC	polycarbonate
PET	poly(ethylene terephthalate)
PMMA	polymethylmethacrylate
PP	polypropylene
PI	polyimide
PTFE	polytetrafluorethylene
RGD	Arg-Gly-Asp
SEM	scanning electron microscopy
THF	tetrahydrofuran
ToF-MS	time-of-flight mass spectroscopy
TXB	Thermanox [®] , more hydrophobic side
TXL	Thermanox [®] , more hydrophilic side
UV	ultraviolet
UV/VIS	ultraviolet/visible spectroscopy
VIS	visible light
VUV	vacuum ultraviolet
WLI	white light interferometry
WLM	white light microscopy
XPS	X-ray photoelectron spectroscopy

Symbol

A	absorbance	α	absorption coefficient
C_p	specific heat capacity	ε	dielectric constant
c	light velocity	ε_0	dielectric constant of vacuum
d	etching rate	ϕ_s	quantum yield
E	activation energy	κ	extinction coefficient
E	electronic field	κ	thermal conductivity
F	laser fluence	λ	wavelength
F_{th}	threshold fluence	ν	light frequency
h	Plank constant	$\Delta\nu$	linewidth
H	magnetic field	θ	angle
I	light intensity	ρ	Mass density
I_0	incident light intensity	$\Delta\tau$	full width at half maximum
k	wave number	ω	angular angle
l_a	optical penetration depth	ω_p	plasma frequency
L_c	coherence length	ψ	wavefunction
l_d	diffusion length		
M	molar concentration		
M_n	number average molecular weight		
n	refraction index		
P	period of the interference pattern		
R	reflectivity		
R_z	Rayleigh length		

Kurzzusammenfassung

Wechselwirkungen zwischen Zellen und fremden Oberflächen sind die grundlegenden Aspekte, um die Funktionen der Oberflächenchemie und -Topographie der Biomaterialien zu verstehen. Wenn sich die Zellen in ihren Reaktionen zu den topographischen Veränderungen unterscheiden, kann dieses Phänomen ausgenutzt werden, die Zellfunktionen zu regulieren und Materialien für Implantate zu entwickeln. Zellreaktionen zur Oberflächentopographie, insbesondere die Orientierung und Differenzierung, die durch Oberflächenmikrostrukturen induziert werden, werden als „Contact Guidance“ genannt.

In dieser Arbeit wurde die Laserinterferenzlithographie eingesetzt, um periodische lineare und punktförmige Mikrostrukturen zur Untersuchung von „Contact Guidance“ der Säugetierzellen aufzubereiten. Dieser Prozess gewährleistet eine direkte Mikrostrukturierung, die auf gezielter Laserabtragung der Polymerwerkstoffe basiert, welche die periodische Energieverteilung der Interferenzmuster von zwei oder mehr Laserstrahlen ausnutzt. Die Laserablations-Mechanismen wurden mit Flugzeitmassenspektroskopie, Röntgenelektronenspektroskopie, bzw. durch Laserablation einer Dünnpolymerlösung untersucht. Der Mikrostrukturierungsprozess wurde in Bezug auf Polymereigenschaften, Energiedichte und Pulsanzahl optimiert. Die Mikrostrukturen wurden durch Atomkraftmikroskopie, Rasterelektronenmikroskopie und Weißlichtinterferometrie charakterisiert.

Mäusefibroblasten und menschliche Lungenfibroblasten wurden auf 2D- und 3D-Mikrostrukturen mit unterschiedlichen Perioden gezüchtet, die durch Laserinterferenzlithographie angefertigt wurden. Die Morphologie der gezüchteten Zellen wurde direkt mit Atomkraftmikroskopie oder nach Färbung und Lufttrocknung mit Weißlichtmikroskopie aufgenommen. Die Zellen, die auf 2D-Mikrostrukturen von Polyethylenterephthalat, Thermanox und Polycarbonat gezüchtet wurden, waren länglich orientiert und entlang der Linie ausgerichtet. Demgegenüber dehnten sich die Zellen auch aus, die auf 3D-Punktmustern

gezüchtet wurden, aber zeigten nur einigermaßen Ausrichtung. Die physiologische Reaktion wurde durch E-Selectin-Expression untersucht. Schließlich wurden die Ergebnisse und die verbleibenden Fragen in Bezug auf Laserablations- und Zellentzündungsmechanismen zusammengefasst.

Abstract

Cell-surface interactions are fundamental aspects to understand the role of surface chemistry and topography of biomaterials. If cells differ in their response to topographic variations, this phenomenon may be exploited to regulate cell functions and to design implant materials. Cell responses to surface topography, especially the orientation and differentiation induced by surface micropatterns, are called contact guidance.

In this work laser interference lithography was introduced to prepare periodic linear and point micropatterns for study of contact guidance of mammalian cells. This process provides a straightforward micropatterning technique based on selective laser ablation of polymers utilizing the periodic energy distribution of two or more beam interference patterns. The ablation mechanisms of polymers were studied with time of flight mass spectroscopy, X-ray photoelectron spectroscopy, and by using thin polymer solution followed by spectroscopic analysis and molecular weight measurement. The micropatterning process was optimised with respect to polymer properties, laser fluence and pulse number. The micropatterns were characterized by atomic force microscopy, scanning electron microscopy and white light interferometry.

Mouse fibroblasts and human pulmonary fibroblasts were cultured on linear and point patterns with different periods induced by laser interference lithography. Photographs were taken by using atomic force microscopy directly or with white light microscopy after being stained and air-dried. The cells cultured on linear micropatterns of poly(ethylene terephthalate), Thermanox™ and polycarbonate were elongated, spindle-like, and aligned along the linear patterns with all different groove widths. In contrast, cells cultured on point patterns were also bipolar but showed only limited orientation. The physiological responses have also been studied by E-selectin expression. At last the results are summarized and the

remaining questions with respect to laser ablation and inflammation mechanisms were discussed.

1 Introduction

In the past few decades, there has been an enormous increase in both the variety and the number of implants used in medicine and dentistry [1]. For example, ceramics and metals have been used as knee joints or teeth prostheses, polymer heart valves were implanted into diseased heart. These man-made materials are bio-inert, although surface and bulk modifications were made considering the biocompatibility. Most implants in use today continue to suffer from problems of interfacial stability with host tissues, biomechanical compatibility of elastic moduli, production of wear debris, and maintenance of stable blood supply [2]. These problems have been more and more overcome through development of new materials, in particular, through chemical and topographical surface modifications, as well as new characterization and evaluation technologies.

Nevertheless, all implants still lack at least two of the most critical characteristics of living tissues: (1) ability to self-repair and (2) ability to modify their structure and properties in response to environmental factors such as mechanical load or blood flow [2]. In order to overcome these disadvantages of implants and the shortages of organs available for transplantation, new ideas towards creating artificial constructions to direct tissue regeneration have attracted many scientists and surgeons with hope to treat patients via self-repairing. These ideas are called tissue engineering which applies methods of engineering and life science to control the cell growth and proliferation on the scaffold and provide the biofunctions of the repaired organ or tissue as a native one [3-4]. The real tissue regeneration is only feasible under the successful design of the biocompatible and biodegradable materials with controlled textures and surface micropatterns. Problems with this approach include insufficient cell migration into the scaffolds and inflammatory reactions to by-products of scaffold biodegradation.

The design of biomaterials is based on understanding of cell-surface interactions and the role of surface chemistry and topography. If cells differ in their response to topographic variations of the substrate, this phenomenon may be exploited to regulate cell functions, and to design implant materials. It is supposed that an important factor in the final tissue reaction towards an implanted device is the “initial” reaction of cells towards the device [1]. Therefore, many studies performed during the past two decades have focused on gaining an understanding of the interactions among different cells, tissues and the implant materials, and improving the biocompatibility of biomaterials through chemical and physical modifications. One example is the endothelialization of prosthetic grafts [5]. Studies have been focusing on seeding endothelial cells on artificial blood vessel since it is thought to help the healing process after the artificial blood vessel is implanted into a host body. However, this operation has engaged several problems or failures. For instance, the endothelial cells couldn't resist the shear force under normal physiological conditions, and always detached from the artificial vascular wall. In addition, inflammation frequently occurred after endothelial cells were seeded on the biomaterials for some unknown reasons, and the artificial blood vessel failed to achieve what was expected. Although attentions have been paid in investigating the induction of inflammation by chemically modifying the surface of biomaterials, fewer considerations have been made to focus the effects of micropatterning on inflammation. In short, the interactions between cells and biomaterials are still not yet clearly understood; lots of questions remain unsolved.

One of the methods often used to investigate cell-surface interactions is to vary the surface properties by producing chemical and topographical surface micropatterns, especially the so-called ridge-groove patterns, in order to control the spreading and spatial orientation of cells. For this purpose, polymer-based biomaterials are mostly used because they can be easily micropatterned with different conventional and unconventional methods such as photolithography, micro-moulding, and etching through electrons, ions, laser beams or plasma.

Such studies were mostly carried out on vertical patterns because it is relatively easy to make patterns with vertical walls, and much more difficult to make arbitrary patterns on a micron scale [1].

Researches have shown that biomaterials bearing some kinds of surface micropatterns could direct the cellular growth in a particular orientation known as contact guidance [6-8]. Various strategies, such as lithographic and chemical techniques have been utilized to produce such surface micropatterns with defined and controlled dimensions. These processes and the results of cell cultures were reviewed by Curtis and Wilkinson [9], Singhvi et al. [10], Walboomers and Jensen [1], Ito [11], Geissler and Xia [12].

Photolithography [13] is a well-established method in semiconductor technology to fabricate lateral micropatterns, which are also used to study the cellular orientation influenced by the different topographies of silicon surfaces. Incorporating micro-molding or embossing technologies, various patterns can be copied from silicon onto polymer surfaces. Electron [14] and ion [15] beams are used to prepare linear and point-like structures directly. Furthermore, phase separation of polymers provides another possibility to produce random dots in nano-scale. Besides, the plasma is often used to chemically modify and micropattern the polymer surfaces [16-17].

Lasers have attracted more and more attention, and become one of the commonly used techniques to prepare surface micropatterns, and to modify surface chemical properties because of their versatility, monochromaticity as well as high power density [18]. Using a focused laser beam, lines or cavities can be directly written onto the surface; however, only one line or cavity can be produced each time [19]. Monolayer or photosensitive films such as photoresist or thin gold film can be patterned by means of a laser projection process through a mask [20]. Laser interference Lithography (LIL) provides another straightforward and efficient technique to prepare micropatterns on ceramic [21], metal [22] and polymer surface [23]. This method is based on selective laser ablation of polymers by two or more high power

laser beams, which superimpose on the polymer surface, and form the interference patterns there. No further wet development is necessary, which makes this method efficient, cost-effective and environmental friendly for systematic research of the relations between cell and substrate topography.

1.1 Tasks of this work

The aim of this study is to micropattern polymer surfaces by means of laser interference lithography in order to investigate the topographical and chemical influence on cell reactions *in vivo*. Since laser interference lithography is based on laser ablation of polymers, laser ablation mechanisms should be first investigated systematically. The main contents in this thesis include:

- Study of laser ablation mechanisms of polymers. The ablation rate is measured under different laser fluence, the chemical surface modification is characterized by X-ray photoelectron spectroscopy (XPS), and the species emitted during laser ablation are investigated by means of time-of-flight mass spectroscopy (ToF-MS). In order to study if the molecular decomposition occurs under irradiation of 266 nm laser without thermal effect, thin polymer solution is also used and molecular decomposition is characterized with gel permeation chromatography (GPC).
- Micropatterning polymer surfaces by means of laser interference lithography. This process is optimised concerning the laser fluence, laser pulse number as well as polymer properties. The LIL-induced micropatterns are characterized with white light interferometry (WLI), atomic force microscopy (AFM) and scanning electron microscopy (SEM).
- Contact guidance of cells on polymer surfaces micropatterned by laser interference lithography. *In vitro* cellular responses to various linear and point-like micropatterns

are studied. Cells cultured on LIL-induced micropatterns are characterized with AFM and white light microscopy (WLM). The inflammatory response is studied by means of E-selectin expression.

2 Fundamentals

2.1 Laser-material interactions

2.1.1 Light propagation

Light is an electromagnetic wave which consists of electric and magnetic field. The electric field of a wave propagating in a homogeneous and non-absorbing medium can be represented as

$$\mathbf{E} = E_0 e^{i(2\pi z/\lambda - \omega t)}, \quad \text{Eq. 2-1}$$

where z is the coordinate along the direction of propagation, ω is the angular frequency, and λ is the wavelength [24]. An expression analogous to Eq. 2-1 also holds for magnetic field \mathbf{H} . Electric and magnetic field amplitudes are related by

$$\mathbf{H} = n_1 \epsilon_0 c \mathbf{E}_0, \quad \text{Eq. 2-2}$$

where ϵ_0 is the dielectric constant of vacuum and n_1 is the refraction index of the medium.

The energy flux per unit area of the wave is termed intensity and given by

$$I = |\mathbf{E} \times \mathbf{H}| = n_1 \epsilon_0 c E_0^2. \quad \text{Eq. 2-3}$$

When a light beam with intensity I_0 goes from a medium to another, the light will be divided into three fractions: reflected (I_R), absorbed (I_A) and transmitted (I_T) light.

$$I_0 = I_R + I_A + I_T \quad \text{Eq. 2-4}$$

Absorption is the precondition of the laser materials processing. In order to cause any lasting effect on a material, laser light must be absorbed. The energy absorbed by the medium is described by Lambert-Beer-Law

$$A = \lg \frac{I_0}{I} = \kappa l M \quad \text{Eq. 2-5}$$

where A is called absorbance, I_0 is incident intensity, I is the light intensity transmitted through the film or solution, κ is the extinction coefficient in $\text{Lmol}^{-1}\text{cm}^{-1}$, l is the sample thickness (cm) and M is molar concentration (molL^{-1}) [25]. In solid state physics the absorption coefficient α (cm^{-1}) is usually used and given by

$$T = \frac{I}{I_0} = e^{-\alpha l} . \quad \text{Eq. 2-6}$$

α^{-1} is often denoted as optical penetration depth l_a . α is wavelength- and temperature-dependent. For uniform materials, the attenuation function $f(z)$ of a laser beam in z direction can be written as

$$f(z) = \alpha(T(z)) \exp[-\int_0^z \alpha(T(z')) dz'] \quad \text{Eq. 2-7}$$

If α is finite but independent of temperature, we obtain

$$f(z) = \alpha \exp(-\alpha z) . \quad \text{Eq. 2-8}$$

With absorption of light, the materials are excited, heated, which then results in a series of reactions, such as ablation, chemical and physical surface modifications, phase inversion, and so on. To understand these reactions, the interactions between laser and materials must be discussed at first. The UV/VIS radiation can only interact with the electrons of the atoms because the much heavier nuclei are not able to follow the high frequencies of UV/VIS radiation.

2.1.2 Laser-metal interactions

Metals are characterized by their free electrons which dominate their optical response because their inner electrons interact only weakly with the applied electromagnetic field [26]. The free

electrons are accelerated in the electrical field and gain energy. Due to the periodic change of the field vector, the oscillating electrons will transfer the dynamic energy to the lattice or reradiate it as reflected light which causes the high reflectivity of metals. Drude theory can be used to describe the interactions of laser radiation with metals, where the complex dielectric index $\varepsilon = \varepsilon_1 + i\varepsilon_2$ is given by:

$$\varepsilon_1 = n^2 - \kappa^2 = 1 - \frac{\omega_p^2 t_c^2}{1 + \omega^2 t_c^2} \quad \text{Eq. 2-9}$$

$$\varepsilon_2 = 2n\kappa = \frac{\omega_p^2 t_c^2}{\omega(1 - \omega^2 t_c^2)} \quad \text{Eq. 2-10}$$

where n and κ are the refraction index and the extinction coefficient respectively, t_c is the mean time between two collisions. Plasma frequency ω_p is given by the density of free electrons with mass m and dielectric constant ε_0 :

$$\omega_p = \sqrt{\frac{Ne^2}{m\varepsilon_0}} \quad \text{Eq. 2-11}$$

The reflectivity R and absorption coefficient α are obtained via n and κ :

$$R = \frac{(n-1)^2 + \kappa^2}{(n+1)^2 + \kappa^2} \quad \text{Eq. 2-12}$$

$$\alpha = \frac{2\omega\kappa}{c} = \frac{4\pi\kappa}{\lambda} \quad \text{Eq. 2-13}$$

The plasma frequency is connected to the specific electrical resistant (ρ_{el}) of the metal:

$$\frac{1}{\rho_{el}} = \frac{Ne^2 t_c}{m} = \omega_p^2 t_c \varepsilon_0 \quad \text{Eq. 2-14}$$

2.1.3 Laser-insulator interactions

Insulators, including most polymers and ceramics, contain no free electrons. They are transparent except in the vicinity of resonance of the electrons with the electric field. In the

classical model a resonance means that the frequency of the electric field matches the resonance frequency ω_0 of the harmonic oscillator, a resonance in quantum mechanics corresponds to a transition between two states separated by the energy difference $\Delta E = \omega_0 h / 2\pi$. In other words, an atom or molecule can absorb energy from light if the frequency of the light oscillation and the frequency of the electron or molecular "transition motion" match,

$$\Delta E = E_2 - E_1 = h\nu \quad \text{Eq. 2-15}$$

where E_2 and E_1 are different energy levels, h is Plank constant and ν is the frequency of the light. Since the energy level is discontinuous, the absorption of light under this mechanism is also selective. The electromagnetic spectrum has a tremendous range of energy and, therefore, gives rise to different excitations corresponding to transitions between fixed energy levels of the molecules. The various light-insulator interactions are schematically described in Fig. 1.

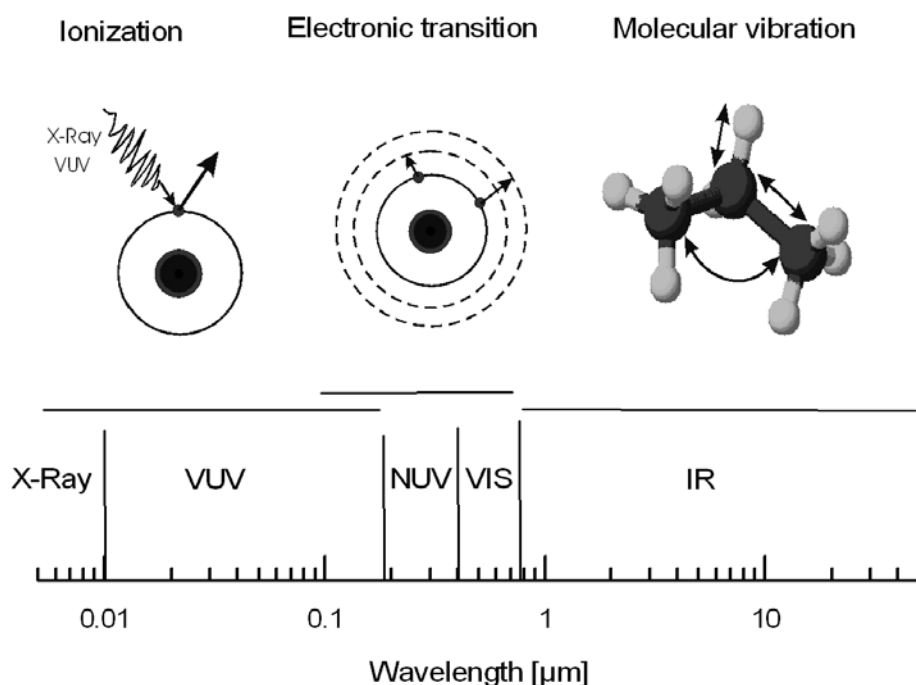


Fig. 1 Fundamental responses of the insulator molecules excited by light with different wavelengths

The energy irradiation in the infrared region (IR: 760 nm - 1 mm) corresponds to the energy levels of different vibrational states in a molecule [27]. When infrared light passes through a sample (solid, liquid or gas), the radiation with certain frequencies is absorbed by the molecules of the substance when the frequency matches the natural vibrational frequency of the molecules. The absorbed energy leads to the molecular vibrations. Consequently, a change in dipole moment of the molecule occurs. Vibrations giving rise to changes in bond length are called stretching vibrations, while those resulting in bond angles are called bending vibrations. A simple molecule can possess a large number of possible molecular vibrations that are expressed as the absorption bands in the IR spectrum. The photon energy of IR light is about 0.0012 - 1.65 eV, not enough to break chemical bond or cause chemical reactions unless more than one photon is absorbed by the same chemical bond. The absorbed energy is ultimately dissipated to the environment as heat or radiation.

Absorption of light energy corresponding to ultraviolet (UV) and visible (VIS) regions of the electromagnetic spectrum results in transitions between electronic energy levels in molecules, which is usually explained as transition between two molecular orbitals (MOs) [27]. The organic molecules may contain σ , π and/or n orbitals. The σ MOs are formed by overlap of two atomic orbitals when they are symmetrical around the axis joining the atomic nuclei. Within the benzene ring a large π orbital is formed through overlapping an unhybridized p orbital perpendicular to the ring of the 6 C-atoms. π electrons are delocalized evenly above and below plane of ring. C- and O-atoms contain also lone-pair nonbonding electrons which form n orbitals. σ orbitals possess the lowest energy and can only be excited by photons with the shortest wavelength, normally shorter than 200 nm. A variety of possible MO transitions are shown in Fig. 2, depending upon the photon energy of the UV/VIS light impinging to the molecules.

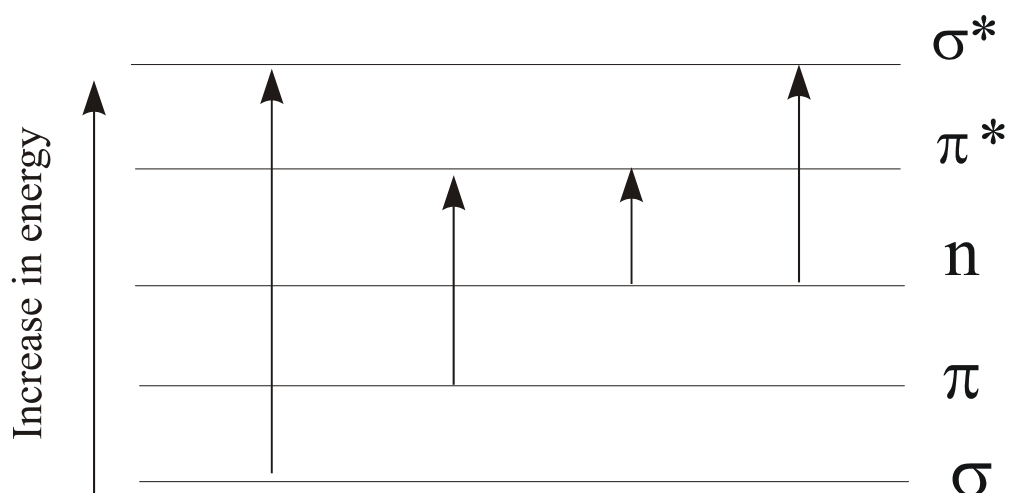


Fig. 2 UV/VIS excited electronic transitions between the bonding and antibonding molecular orbitals in a molecule [28]

$\pi \rightarrow \pi^*$ and $n \rightarrow \pi^*$ absorptions occur in the near ultraviolet (NUV: 400-190 nm) and the visible (VIS: 400-760 nm) region. Many organic molecules with double bonds, particularly those in which one of the double bonded atoms has at least one lone pair electrons, absorb radiation in the near UV region. Examples include polymers with benzyl group, such as PET, PC, polystyrene (PS) and Polyimide (PI), as well as polymers with carbon-oxygen groups. These functional groups are called chromophores. Originally it was used for visibly colored molecules, but it applies also to UV- and IR-absorbing molecules.

Molecules containing strong sigma bonds and no lone pair electrons tend to absorb far ultraviolet light (<190nm) to excite $\sigma \rightarrow \sigma^*$ transitions. The only excitable electrons are those forming the single bonds, and they must receive a large amount of energy in order to undergo a transition to the empty orbital from the lowest energy level of the molecules. Polymers such as polyethylene (PE) and polypropylene (PP) have no absorptions at wavelengths longer than 190 nm. Strongly single bonded molecules with lone pair electrons on electronegative atoms also tend only absorbing light with very short wavelength (high

energy). Thus water, HF, NH₃, and the like have no absorptions in the visible or near-UV regions of the electromagnetic spectrum.

Since the quantum energies (>124 eV) of X-ray photons (<10 nm) are too high to be absorbed for electronic transitions, they can interact with an electron only by knocking it completely out of the atom to produce a fragment with a net positive charge (positive ion). Therefore, all x-rays are classified as ionizing radiation. This can occur by giving all of the energy to an electron (photoionization) or by giving part of the energy to the photon and the rest to a lower energy photon (Compton scattering). At sufficiently high energies, the x-ray photon can create an electron positron pair.

2.1.4 Evolution of temperature induced by laser

Providing that all laser energy absorbed is transferred to heat by which the bulk material is heated to higher temperature, the time evolution of the temperature induced by laser pulse may be obtained by solving the one-dimensional heat equation

$$C_p(T)\rho(T)\frac{\partial T(z,t)}{\partial t} = G(z,t) + \frac{\partial}{\partial z}(\kappa(T)\frac{\partial T(z,t)}{\partial z}) \quad \text{Eq. 2-16}$$

where $T(z, t)$ [T] is the temperature at point z and instant t , $\rho(T)$ [g/cm³] the density, $C_p(T)$ [J/g·K] the specific heat capacity, and $\kappa(T)$ [J/cm·s·K] the thermal conductivity [29]. The heat generation $G(z, t)$ [J/cm³·s] may be expressed in terms of the light absorption coefficient α and surface reflectivity, as

$$G(z,t) = I(t)\alpha e^{-\alpha z} (1 - R), \quad \text{Eq. 2-17}$$

where $I(t)$ is the pulse shape, approximately given by a Gaussian

$$I(t) = \frac{E}{\sigma(2\pi)^{1/2}} \exp\left[-\frac{1}{2}\left(\frac{t-t_0}{\sigma}\right)^2\right], \quad \text{Eq. 2-18}$$

where E [J/cm²] is the pulse energy density, and σ is related to the Gaussian full width at half maximum (FWHM) $\Delta\tau$ by

$$\sigma = \frac{\Delta\tau}{2(2\ln 2)^{1/2}}. \quad \text{Eq. 2-19}$$

The temperature distribution induced by laser irradiation can be simulated by solving Eq.2-16 when the parameters of the laser and the substrate are known. Yet this partial differential equation can only be solved numerically with the help of mathematical software, such as Maple, Mathematica and so on.

2.2 Laser ablation of polymers

2.2.1 Laser ablation mechanisms

When a polymer is excited by laser, the energy may be dissipated by the following processes [25]:

- a) radiative process: luminescence;
- b) radiationless process;
- c) dissociation process, which occurs when absorption of a radiation raises a molecule from the ground state (S_0) to repulsive excited state;
- d) bimolecular deactivation process (energy transfer process).

Through process a) the polymer is excited by the photon energy first, and then relaxes to lower electronic levels by emitting electromagnetic waves with shorter wavelengths. The polymer remains unchanged and there is also no temperature increase in the bulk material.

Through process b) the excited state goes back to ground state by transferring the absorbed laser energy into thermal energy so that the bulk material is heated to a higher temperature.

When the laser intensity is high enough, the polymer will be heated to pyrolytic temperature

and the ablation occurs. This process is called photothermal ablation. Through process c) the polymer chain breaks in the excited state. The absorbed laser energy is transferred into potential and dynamic energy of the species emitted during bond breaking while the temperature of polymer remains unchanged. This process is called photochemical ablation. Through process d), the absorbed laser energy is transferred only from one molecule to another. Therefore, it can be summed up in photothermal and photochemical effects when polymer decomposition after laser irradiation occurs.

However, the practice is not so simple. Following pioneer works of Srinivasan et al. [18, 31] and Kawamura et al. [31], numerous studies were performed to elucidate the laser ablation mechanisms on polymers. But over twenty years, there is still no generally accepted explanation [32]. Srinivasan et al. [18] first used the ablative photodecomposition to describe the cleavage of solid polymers in the electronically excited state based on the fact that the photon energy of an excimer laser (193 nm) is high enough to break the chemical bonds of the polymers and the smooth ablation crater shows that there is no significant thermal experience. Lambert-Beer's law has often been used to describe the fluence dependence of the etch depth (d) per pulse slightly above threshold of the chemical laser ablation

$$d = \frac{1}{\alpha} \ln(F / F_{th}) \quad \text{Eq. 2-20}$$

where F and F_{th} designate the laser fluence and threshold fluence, respectively. Many experimental ablation curves (d against F) satisfy this equation when F is slightly higher than F_{th} . Disagreements have also been found between the slopes of the curves and the $1/\alpha$ of the spectrometry since the depth is normally the average of a number of successive pulses and the absorption properties of the polymer surface have been altered by the former laser irradiation [33].

At longer wavelength, especially at IR region, photothermal effect is considered to contribute to laser ablation of polymers predominantly. This model can be described by a simplified Arrhenius equation

$$d = Ae^{-E/RT}, \quad \text{Eq. 2-21}$$

where A is a constant and E is the activation energy.

In fact, neither photochemical nor photothermal mechanism has successfully explained the experimental results. For this reason Srinivasan et al. [34] suggested an extended model assuming that both mechanisms are effective on laser ablation

$$d = \frac{1}{\alpha} \ln(F / F_{th}) + Ae^{-E/RT}. \quad \text{Eq. 2-22}$$

Under high laser fluence, large amounts of ablation species are produced within a short time (ps to ns). The species possess higher dynamic energy and exercise high pressure against the substrate. The materials may be therefore carried out of the crater explosively [35]. The ablation products may contain relatively long polymer segments, sometimes small melting polymer drops. This effect is called photomechanical ablation. The ablation products with higher boiling point will resolidify around the ablation crater.

In general, laser ablation of polymers is governed by the interactions between laser and polymers. The chemical structure determines laser absorption and the bond breaking behavior, and thus the removal of the materials [36]. Besides, the thermal conductivity and melting point of the polymers will dedicate to thermal influence of the dissipated heat energy on the morphology of the ablation craters. The ablation mechanisms of a definite polymer are determined by laser wavelength and fluence by means of different excitation process [37-38]. In addition, the laser pulse width and repetition rate can impact the heat dissipation (and thus the effect of desorption) of the materials.

2.2.2 Methods for studying laser ablation of polymers

In order to study the laser ablation process and elucidate the ablation mechanisms, different methods have been used to analyse the etching rate, ablation products, as well as the temperature increase and surface modification induced by laser irradiation. Topographical modification can help to deduce what happens during laser ablation. Smooth craters indicate that the ablation is a layer-by-layer process and can be considered as photochemical ablation [37]. On the other hand, coarse craters demonstrate a photothermal process. A very famous example is that regular ripples were formed on PET surface when the laser fluence and wavelength are suitable [39]. They are formed during resolidification of the layer melted by photothermal energy.

X-ray photoelectron spectroscopy (XPS), also known as electron spectroscopy for chemical analysis (ESCA), is a widely used technique to investigate the chemical surface modification after laser ablation. Watanabe and Yamamoto [40] analysed the PET surface irradiated by a KrF excimer laser (248 nm) in Argon and found that the C-content increased while the O-content decreased with the increase of the irradiation energy. Wong et al. [41] analysed the surface chemical composition of PET samples treated with the same laser but under normal atmosphere. At higher fluence the same results were observed as in [40], while reverse effect was found when PET was irradiated with low laser fluence.

Species induced by laser irradiation can be analysed by mass spectroscopy (MS). Srinivasan et al. [33] collected the ablated species of polymethylmethacrylate (PMMA) cryogenically and performed the MS analysis by which methylmethacrylate (MMA) and CO₂ were identified. Watanabe and Yamamoto [40] characterized the ablated PET species by using gas chromatography/mass spectroscopy (GS-MS). The ablation was carried out in the atmosphere purged with argon gas, and then the gas was sampled with a syringe and immediately fed into a GC-MS. They have detected CO, CO₂, and C₆H₆. A more convenient and also important

method is the time of flight mass spectroscopy (ToF-MS) by which the ablated ions, radicals, small molecules and polymer segments can be detected immediately after laser irradiation [42-43].

Calorimetric studies revealed that the photothermal effect contribute also to ablation of polyamide at 193 nm [44]. It was observed that as the fluence was increased, the pyroelectric detector voltage, which is a measure of the temperature of the sample surface, continues to increase, starting even when the fluence is below the threshold. The temperature increase is estimated to lie between 330 and 870 °C for polyamide. Since an exact temperature measurement is impossible, especially for pico and femto laser ablation, mathematical simulation provides another possibility to understand laser ablation mechanisms. Castex and Bityurin [45] calculated the temperature increase of laser ablation at VUV and concluded that both stationary and adiabatic VUV ablation hardly can be considered as pure photochemical if $\kappa > 10^{21} \text{ cm}^{-3}$. κ is defined as the number density of photons which should be absorbed at a particular point to produce critical number density of broken bonds at this point [46].

All these studies can't give direct evidences if photochemical ablation occurs at relatively longer wavelength (e.g. >248 nm). Theoretically, photochemical decomposition can also occur in IR region when the fluence is high enough to excite non-linear absorption. Photochemistry studies have shown that multiphoton absorption and ionisation is possible to initiate photochemical reaction without significant temperature increase when the light intensity is high enough [47]. Even in infrared area, number of photons can be absorbed to result in a photochemical bond breaking [48]. Such experiments are impossible with condensed polymers.

To investigate laser ablation mechanisms of polymers, Tipert et al. [47-50] synthesized new polymers containing triazene groups. These tailor-made polymers can help to explain the ablation mechanisms of polymers. Furthermore, they show a higher quality with respect to size and resolution and have potential applications to microstructures or micro devices.

A commercial polymer can only be excited by the light of several narrow bands and thus can be ablated only by lasers with corresponding wavelengths. Polymers containing no chromophores have no absorption in VIS and NUV region. To avoid these limitations, such polymers have been doped with chromophore compounds or inorganic fillers [51]. The doped polymers show specific ablation behavior depending on the properties of the dopants and fillers which may result in different ablation mechanisms. The resolution can be improved by means of carefully selected dopants.

2.2.3 Applications of laser ablation of polymers

Laser ablation has been used to modify polymer surfaces chemically and topographically. Through laser-polymer interactions and thus induced reactions within polymers or with environmental substances, the surface properties are modified while the bulk material remains unchanged [52-53]. Dadsetan et al. have promoted platelet adhesion to PET by using direct laser ablation [54] and laser induced graftpolymerization [55]. Laser treatment of polymers can also improve the properties of metallization by means of increasing the adhesion between metal film and polymer substrate [56-58].

Laser ablation provides a versatile process to micropattern and micromachine polymers. Using a polarized laser beam below the ablation threshold for a polymer, the so-called laser induced periodic surface structure (LIPSS) can be formed. The mechanism of LIPSS is shown in Fig. 3a. The polarized laser beam with fluence below the ablation threshold interferes with the surface scattered radiation, giving rise to grating-like pattern (Fig. 3b) because of periodic oxidation or photolysis [59]. Periodical structures in submicron range can be produced by this way. The orientation of the structures is determined by the direction of the polarization and the period varies with the incident angle. But this process needs up to one thousand laser pulses and has difficulties in reproducing the structures with exact the same spacing.

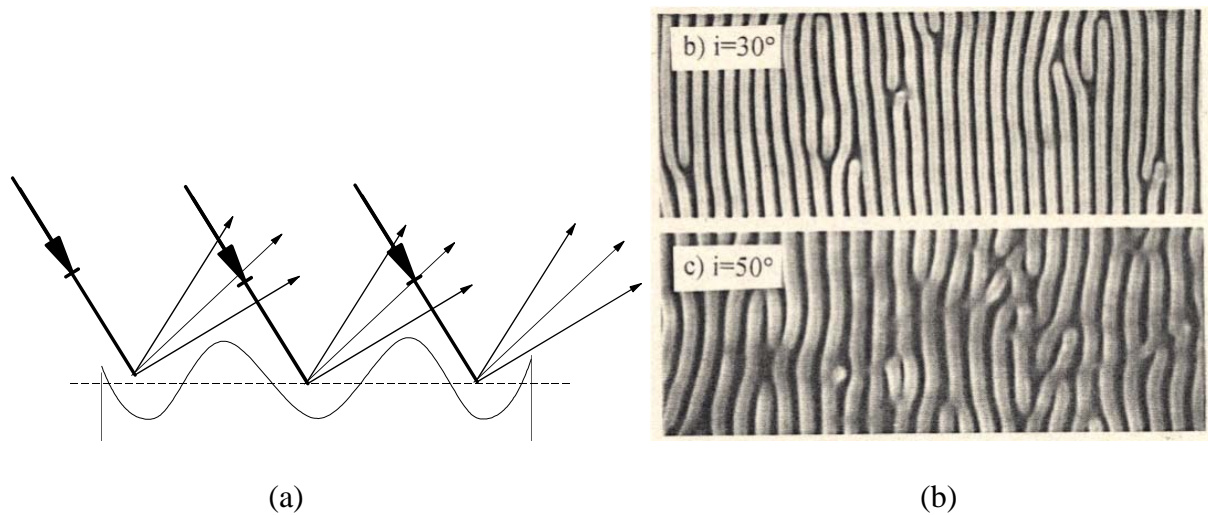


Fig. 3 a) Principle of laser induced periodic surface structures (LIPSS) and b) submicron periodic structures on polycarbonate obtained by irradiation with the polarized KrF laser in air (1000 pulses, $10\text{mJ}/\text{cm}^2$). [59]

A well-focused laser beam possesses energy density far beyond the ablation threshold, giving rise to large ablation rate. Thus cavities, lines or holes can be written to polymer surface directly. Incorporating with a micropositioning stage, the micropatterning can be performed automatically (Fig. 4) [61].

Similar to normal photolithography, micropatterns can be projected to substrates through a mask (Fig. 5) [62]. Since the energy density must be controlled to low level in order to protect the mask, this process is only suitable for photosensitive materials, such as photoresists, monolayers, thin gold films and so on. Sometimes the miropattern must be processed further as shown in Fig. 5.

Laser ablation of biological tissues is another special application which has been used to correct nearsightedness. Another very interesting application is micropatterning of polymer surface by laser interference lithography (LIL) which will be discussed in detail in chapter 2.3.

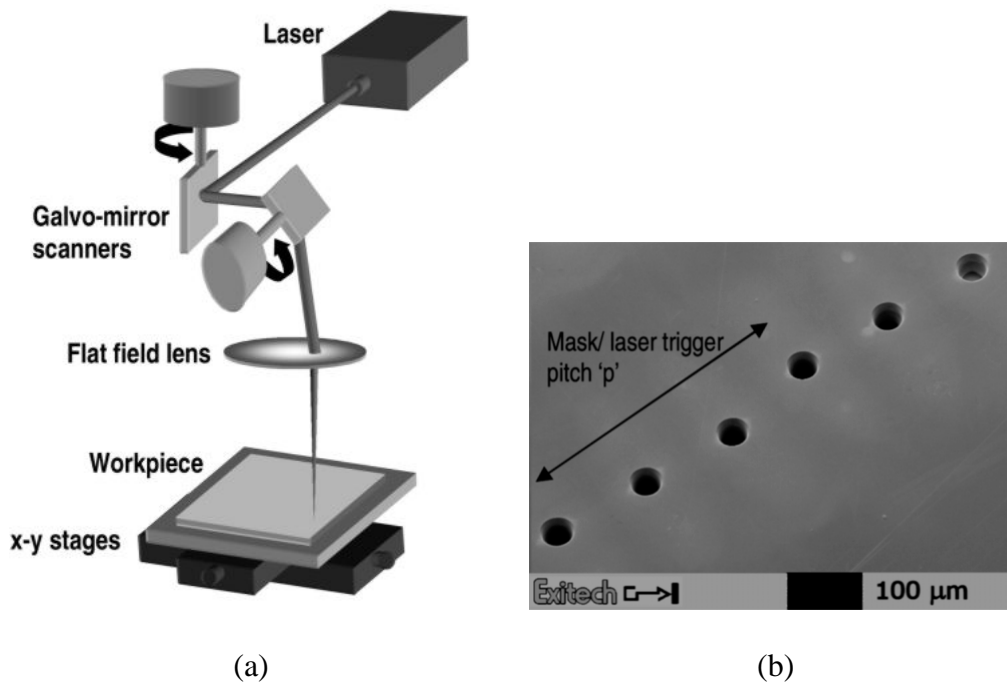


Fig. 4 (a) Schematic diagram of the direct machining using a galvo-scanner and motorised x - y translation stages and (b) SEM photograph of nozzles drilled by synchronised image scanning (SIS) techniques [61].

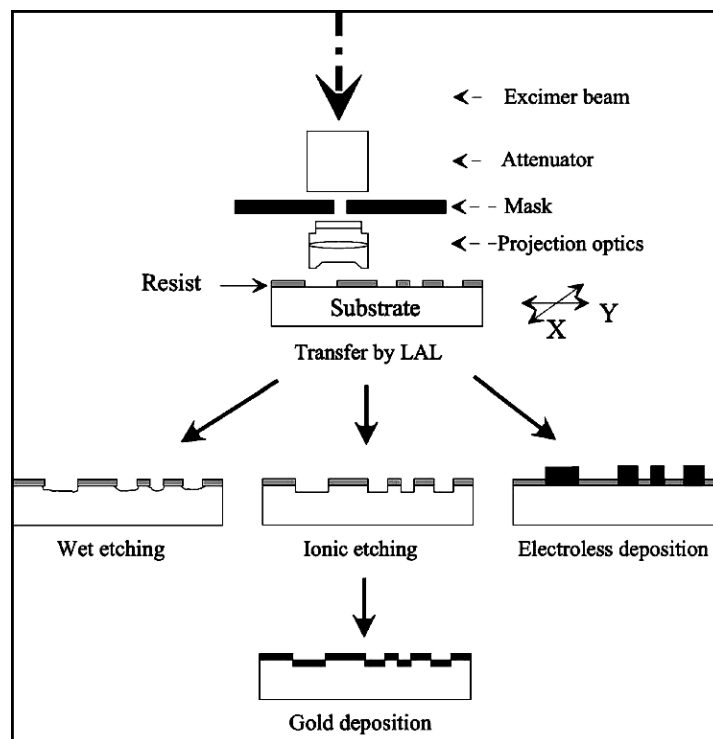


Fig. 5 Principle of laser ablation lithography and the different methods for etching binary kinoform [62].

2.3 Laser interference lithography

Interference is the interaction of two or more coherent waves passing the same point. Constructive interference occurs when the waves add in phase, producing a larger peak than any wave alone, whereas destructive interference occurs when waves add out of phase, producing smaller peaks than one of the waves alone.

Consider two monochromatic waves with wavefunctions ψ_1 and ψ_2 ,

$$\psi_1 = \sqrt{I_1} e^{i(kr + \phi_1)} \quad \text{Eq. 2-23}$$

$$\psi_2 = \sqrt{I_2} e^{i(kr + \phi_2)} \quad \text{Eq. 2-24}$$

If they interfere coherently, then

$$\psi = \psi_1 + \psi_2 = \sqrt{I_1} e^{i(kr_1 + \phi_1)} + \sqrt{I_2} e^{i(kr_2 + \phi_2)} \quad \text{Eq. 2-25}$$

$$\bar{\psi} = \sqrt{I_1} e^{-i(kr_1 + \phi_1)} + \sqrt{I_2} e^{-i(kr_2 + \phi_2)} \quad \text{Eq. 2-26}$$

where $\bar{\psi}$ is the complex conjugate of ψ . The intensity is then given by

$$\begin{aligned} I &= |\psi|^2 = \psi \bar{\psi} \\ &= I_1 + I_2 + \sqrt{I_1 I_2} e^{i[k(r_1 - r_2) + (\phi_1 - \phi_2)]} + \sqrt{I_1 I_2} e^{-i[k(r_1 - r_2) + (\phi_1 - \phi_2)]} , \\ &= I_1 + I_2 + 2\sqrt{I_1 I_2} \cos \delta \end{aligned} \quad \text{Eq. 2-27}$$

where

$$\delta = k(r_2 - r_1) + (\phi_2 - \phi_1) = k\Delta r + \Delta\phi. \quad \text{Eq. 2-28}$$

A special case is $I_1 = I_2 = I_0$. In this case the intensities from both sources are equal, so Eq.

2-28 can then be written as

$$I = 2I_0(1 + \cos \delta) = 4I_0 \cos^2\left(\frac{1}{2}\delta\right). \quad \text{Eq. 2-29}$$

The maximum and minimum intensity of the pattern will be $I_{\max} = 4I_0$ and $I_{\min} = 0$.

Laser interference Lithography (LIL) is based on Eq. 2-29, utilizing the laser energy maximum to ablate the polymers selectively. The period (P) and energy distribution ($I(x)$) of a two-beam interference pattern are given by

$$P = \frac{\lambda}{2\sin(\theta/2)} \quad \text{Eq. 2-30}$$

$$I(x) = 2I_0[1 + \cos(\frac{2\pi x}{P})] \quad \text{Eq. 2-31}$$

where I_0 is intensity amplitude of the partial beams, λ is the wavelength, and θ is the angle between two partial beams. According to Eq. 2-30, the period depends only on θ and λ .

The LIL principle is shown in Fig. 6 schematically. The red curve represents the energy distribution on a two-beam interference pattern. Polymers under the energy maxima will be most ablated and those under energy minima (theoretically 0 J/cm²) will remain unchanged to

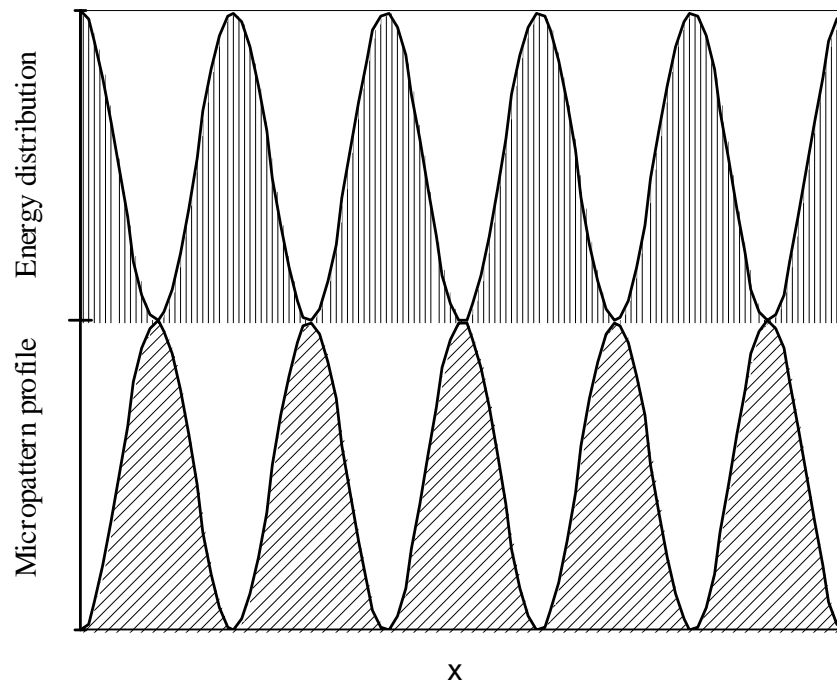


Fig. 6 Schematic representation of the energy distribution on the interference pattern and the induced microstructure

form the top of the micropattern ridges. Thus, the interference pattern is duplicated onto the polymer surface reversibly. No further wet development is necessary, which makes this method efficient, cost-effective and environmental friendly for systematic research of the interactions between cell and substrate topography.

Based on this principle, Phillips et al. [23] used a Talbot Interferometer to ablate the periodical patterns onto the polymer surface directly (Fig. 7a). S- and p-polarized KrF laser beam was attenuated by 45°-coated reflector placed under 66°, and then passed through a quartz block onto a grating. The vertical sides of the quartz block were interferometrically polished, so that when the diffracted +1 and -1 orders from the grating reenter the quartz block, they are reflected internally and recombine on the sample with no optical path difference. The interference pattern created by the recombined beams has a period equal to one half of the period of the grating. The ablated patterns on Polyimide (PI) were measured with a period of 167 ± 3 nm in agreement with the expected value of 164 nm. No information about the depth was reported.

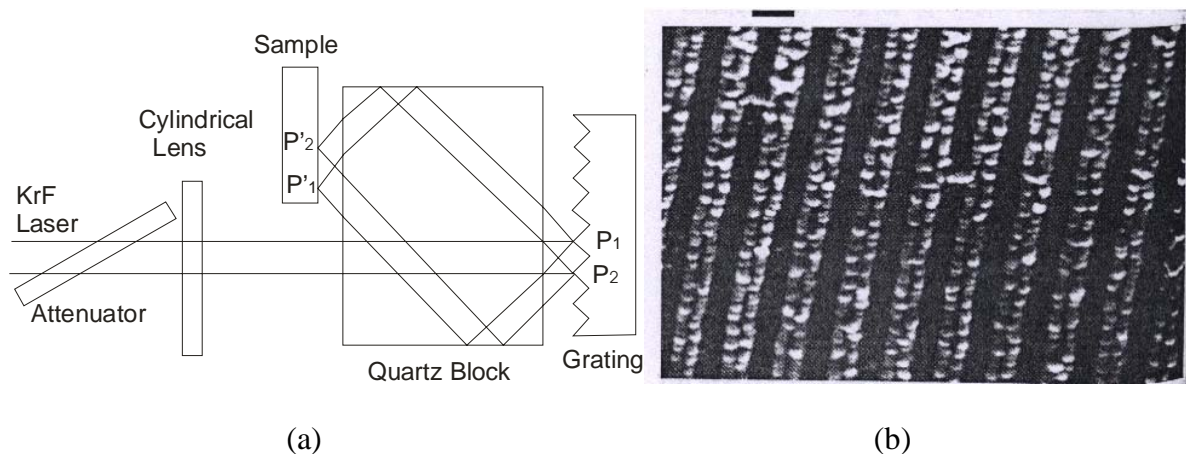


Fig. 7 (a) Experimental setup for laser interference lithography (according to [23]). (b) The micropatterns prepared on PI.

With a frequency tripled Nd:YAG laser, Lippert et al. [63] micropatterned a photosensitive polymer using a Michelson setup (shown in Fig. 8). Well-defined gratings from sub- to

micrometer were obtained with one pulse ablation, while problems were encountered with multiple pulses because of the grating quality. Using similar setup as shown in Fig. 8, periodical linear, point and hole micropatterns were prepared on metal, ceramic and polymer surfaces in the group of Mücklich [21-22].

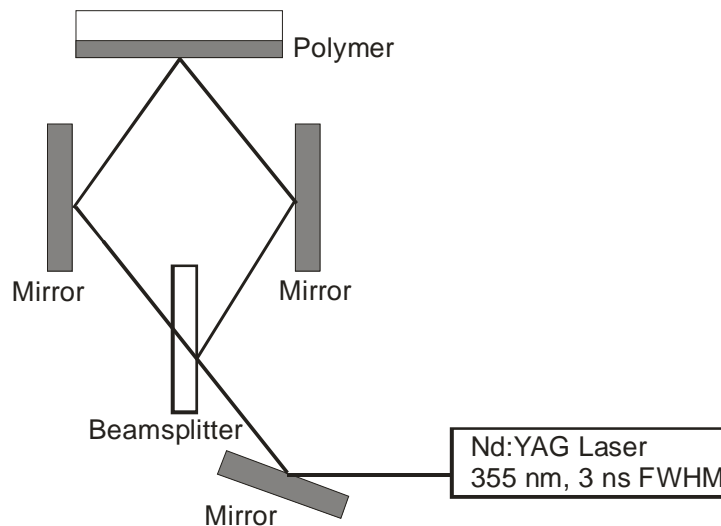


Fig. 8 Experimental setup for LIL used by Lippert et al. (according to [63])

2.4 Cell-substrate interactions

2.4.1 Cell adhesion to extracellular matrix

Cell-surface interactions are fundamental aspects to understand the role of surface chemistry and topography of biomaterials. Cells experience complicated interactions with the substrate during culturing, proliferation, migration and differentiation. Cell adhesion can be divided into two phases: the attachment phase and the adhesion phase [65]. Cellular attachment takes place rapidly with short-term events, like physicochemical linkages between the cell and the material, while the adhesion phase occurs in a long term. After attachment cells extend their plasma membrane in every direction to sense the cell environment and to make initial, dynamic adhesions to extracellular matrix (ECM) and other cells [67]. Cues received are

relayed back to the cell body by cell-signalling mechanisms and influence subsequent cell behavior, e.g. in guiding the direction of cell migration or in the activation of transmembrane transporters or receptors. The cell adhesion involves three types of proteins: ECM proteins, cell membrane proteins, and cytoskeletal proteins. The primary family of cell membrane proteins that mediate the adhesion of cells to substrates are the integrins, a widely expressed family of heterodimeric surface receptors [68].

The closest cell substrate contacts are called focal adhesions which are a 10-20 nm gap between cell membrane and the substrate [1]. At these foci, the end of an actin filament is connected to an integrin (Fig. 9). Integrin is a transmembrane glycoprotein that can bind to ECM components, such as fibronectin, vitronectin, or laminin. An integrin is built as a noncovalently associated complex of two high-molecular weight polypeptides: the α - and β -chain. The integrins are divided into three families according to their β -chain. The proteins in the ECM often contain an RGD (Arg-Gly-Asp) sequence, i.e., a sequence of the amino acids, arginine, glycine, and aspartic acid. This sequence is the part of the matrix protein that is bound by the integrin. In the connection between actin filaments and integrin, several proteins play a role: among others, capping proteins, α -actinin, vinculin, talin, paxillin, and paxillin.

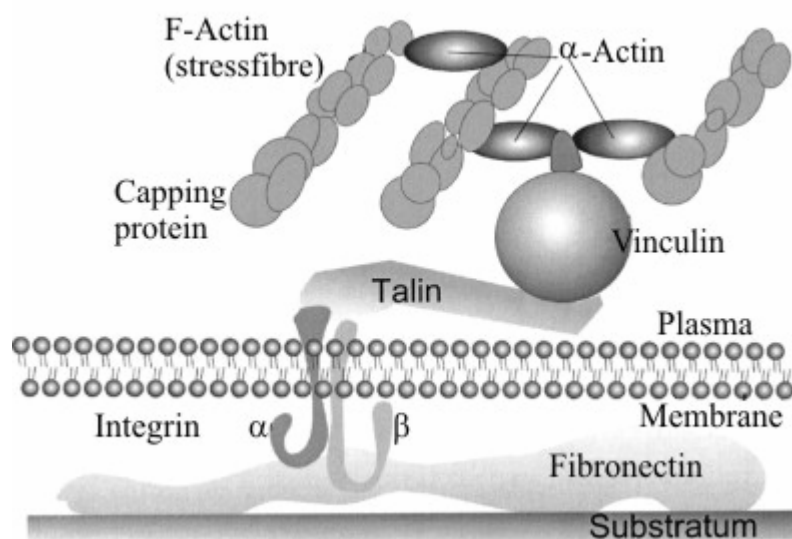


Fig. 9 Schematic representation of a focal adhesion and several of the associated proteins [1].

The adhesion and proliferation of mammalian cells is strongly influenced by the chemistry of a surface, such as hydrophilicity, surface topography, surface free energy, electric charges at the surface, pH value, and receptors associated with cell adhesion. In the absence of surface-bound ligands or hydrogels, surface free energy is strongly correlated to the rate of cellular attachment. It is generally found that high-energy surfaces promote rapid cellular adhesion and spreading, whereas low-energy surfaces do not favour such behavior [69]. Because the primary adsorbates in culture media are extracellular proteins, the reasons for this discrimination are not obvious. It is possible that the characteristics of the adsorbed protein layer are affected by the surface chemistry, e.g. through differential orientation, rates of adsorption or denaturing of proteins at the surface, or that the cell is able to displace at least partially the adsorbed protein layer. Although the mechanism of cellular adhesion is poorly understood, the marked discrimination between surfaces with different surface energy may be used to regulate the attachment of cells at an interface.

Huang et al. reported that the surface roughness (R_a : 0.05–1.20 μm) of ground Ti has a highly significant influence on the attachment of osteoblast-like U-2 OS cells after 2 h incubation. The ground Ti specimen with an R_a value of 0.15 μm has the best cell adhesion and spreading appearance as compared with either the smoother (R_a : 0.05 and 0.07 μm) or rougher (R_a : 0.33 and 1.20 μm) specimens [70].

2.4.2 Cell migration

Cell migration plays a central role in many processes, including embryonic development, wound healing and the immune response [71]. In culturing cell migration occurs on the substrate only with successful cell adhesion. The migration mechanism is similar to that of cell adhesion discussed in 2.4.1. The process consists of a series of alternative adhesion and release between cell and substrate, which is shown schematically in Fig. 10.

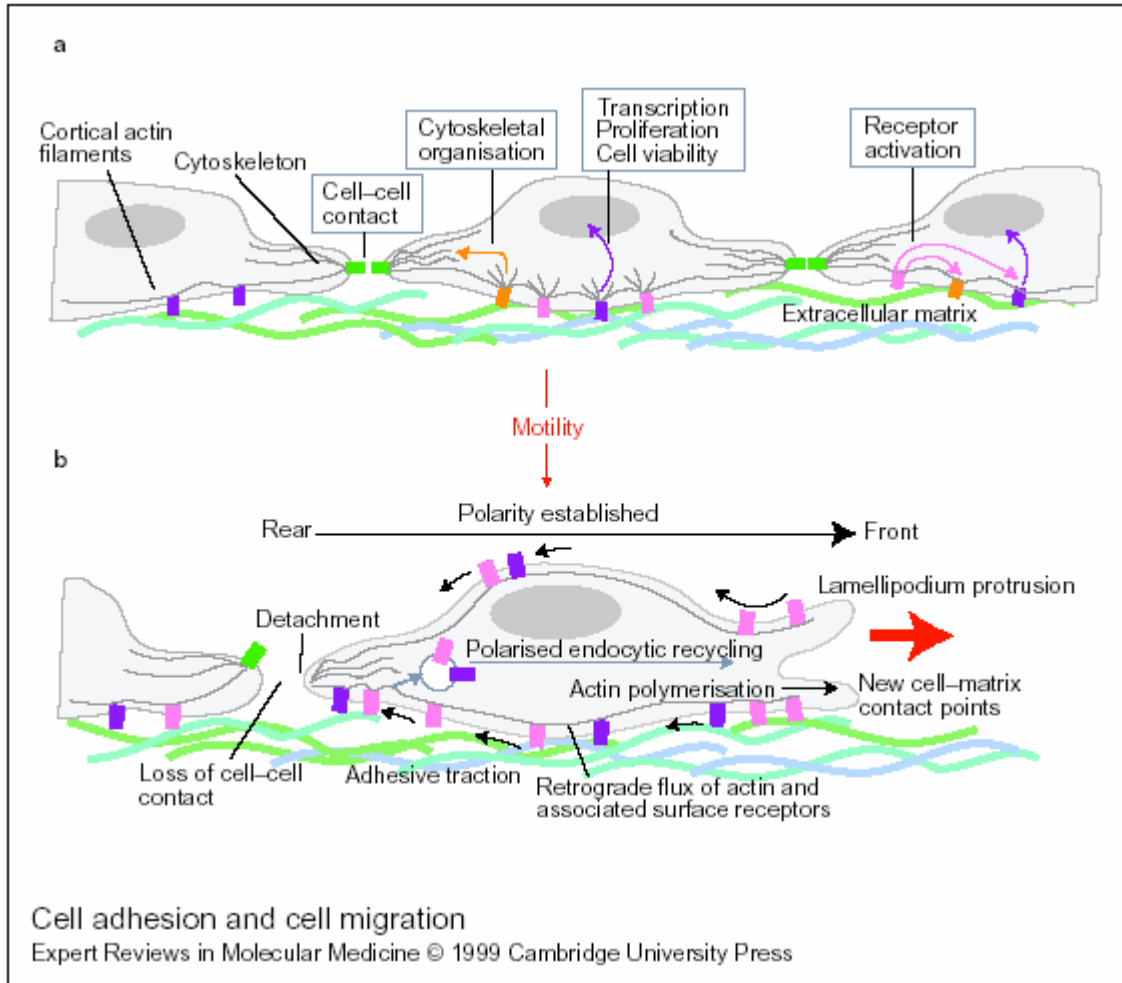


Fig. 10 Cell adhesion and cell migration [72]. (a) The shape and behavior of cells is controlled by a heterogeneous population of transmembrane adhesion molecules which mediate cell–cell and cell–ECM attachment, cell motility and receptor activation. (b) The sequential phases of cell movement in vitro.

The cell movement in vitro begins with the induction of a well-defined front-rear polarity, which determines the direction of motility. Initiation of cell movement involves a directional protrusion in the moving front to form lamellopodia, with its subsequent attachment to the substrate. The front part of the lamellopodia is a broad, flat cytoskeletal protrusion devoid of organelles, and behind is a roundish cell body containing the nucleus and organelles. Membrane extension at the front of the cell is controlled by the combined effects of actin

polymerisation and actin movement mediated by myosin. Receptor proteins (such as integrins) that are inserted into the front of the cell bind to the components of the ECM, thus preventing membrane retraction and providing adhesive traction for cell movement. After formation and stabilization of the lamellopodia, cells use these adhesive interactions to generate the force required for cell movement. The physical process of cell movement results from the retrograde flux of polymerised actin (and associated membrane receptors) and the cyclical flux of membrane from the rear to the front of the cell. The final step in the migratory cycle is the release of adhesions at the rear of the cell, with its subsequent detachment and retraction. The adhesive force at the cell front must be sufficient to generate force and traction to pull the cell forward, and the adhesive strength at the rear must be weak to allow the cell to release from its substrate.

After immigration, cells release highly ordered traces which can be traced back to the interactions between cell and substrate. Zimmermann et al. [73] investigated the cell-trace formation systematically with AFM/IRM (atomic force microscopy/interference reflection microscopy) and time-resolved TIRAF (total internal reflection aqueous fluorescence) and observed that the traces are about 100 nm in height and width but several hundred micrometers in length. They believe that the traces are not simply inevitable wastages during migration but basic elements of cells comparable to lamellopodia, filopodia and other appendices. Potentially, they could be as important and universal as some intracellular structures.

During movement, cells sense the environment and react to the topographical and chemical properties of the substrate surface by means of changing their morphogenesis and moving path. This phenomenon has been utilized to design biomaterials and implants with specific surface properties to control cell response and functions.

2.4.3 Contact guidance

One of the most investigated cell-substrate interactions is cellular behavior affected by substrate topography [1, 9-10, 74]. The effect of surface topography on the development, motility, differentiation, orientation, and alignment of cells was first reported by Harrison [75] in 1912, and termed as “Contact Guidance” by Weiss [76] in 1945 for the ability of an underlying substrate to direct or modify the response of cells. No further attention was paid to this phenomenon until 1970s when Rovinsky et al. [77] rediscovered the guidance effect of the substrate topography. Strictly spoken, contact guidance involves only the effects of the morphological variation on the surface, but cells also show the same response on chemically modified surface [78-81].

Among random and regular surface patterns, the so-called groove/ridge patterns were mostly utilized to study cell behavior on microstructured substrates because of their reproducibility. Cultured on groove/ridge patterns with lateral dimensions from nano- to micrometer range, contact guidance was found with different cells, including fibroblast [6, 82-85], epithelial cells [86-87], neuron cells [7, 88-89], muscle cells [90], osteoblast [91-93] etc. The degree of orientation depends on cell type, substrate materials, groove depth and width.

Clark et al. [94-95] reported that the extent of cell reaction is related to groove width as well as depth and probably also the number of adjacent grooves. It is generally accepted that the extension of orientation increases with groove depth up to about 25 μm of about 1 μm relief. There are a few reports about contact guidance on nano- and submicrometer features. Clark and colleagues [95] found that fibroblast and epithelial cells aligned along grooves and ridges of 130 nm width. Similar substrates were found to induce alignment of oligodendrocytes but not of rat hippocampal or cerebellar neurons [96]. When grooves or ridges are appreciably wider than cells the orientation effect is no more obviously although cells may align to one edge [94]. On deeper and narrower grooves cells may bridge from ridge to ridge so that cells

react only to features of the ridges [6]. Eichenbarth [97] et al. suggested that the elongation of the cells provides more favourable adhesion behavior than the spherical cells based on the observations that the orientated cells had a higher density of focal contacts on the ground grooves.

Contact guidance was also observed on various substrates chemically micropatterned with UV [98] and plasma [69] treatment, ion bombardment, proteins of cell adhesion or growth factors [99-101], immobilization of functional molecules [102] and so on. Mitchell et al. [98] reported that Chinese hamster ovarian (CHO) and mouse embryo 3T3-L1 (3T3) cells show increased attachment and orientation on polystyrene surface chemically patterned with ultra violet/ozone through a mask. AFM studies show that the surface roughness is an order of magnitude less than that expected to cause an effect. Micropatterned immobilization of various proteins has been confirmed as an effective method to initiate cell orientation, which was reviewed by Blawas and Reichert [99]. Among the proteins, cell adhesion proteins or adhesion active peptides were used to regulate cell attachment or neurocite extension of neural cells.

Up to now the most studies were concentrated on the positive effects of the surface topography, such as increasing cell attachment, orientation, differentiation or proliferation. However, contact guidance is meanwhile a process by which the cells accumulate the signals from the environment and vary its behavior to accommodate their new environment. In some circumstances the cells are forced to change their form and functions so that the unexpected reactions and differentiation may also occur. The investigation of these phenomena can help to understand the cell-substrate interactions comprehensively and to improve the biocompatibility of the biomaterials.

3 Experimental

3.1 Laser

The most commonly used lasers for ablation of polymers are excimer (ArF: 193 nm, KrF: 248 nm, and XeF: 308 nm) and Nd:YAG lasers. The fundamental wavelength of Nd:YAG laser is 1064 nm from which a series of wavelengths (532, 355 and 266) can be generated by means of frequency doubling (also called second-harmonic generation, SHG) so that a laser can provide different wavelengths covering from IR, VIS to UV. Another advantage which is very important for LIL is that the laser beam from Nd:YAG possesses larger coherent length compared with excimer lasers, which makes it much easier to adjust interference patterns.

In this study a Q-switched Nd:YAG laser (Spectra Physics, USA) which works under four different wavelengths (1064, 532, 355 and 266 nm) with a frequency of 10 Hz was used for micropatterning.

3.1.1 Working principle of Nd:YAG laser

Laser is the abbreviation of **L**ight **A**mplification of **S**timulated **E**mission **R**adiation. The precondition of lasing is population conversion that arises when more atoms are in a higher state of excitation than those below, which is schematically described by a model of four-level transition (Fig. 11). In this system, the pumping transition excites the atoms from the ground state (E_0) into the pump band (E_3). From level E_3 , the atoms again decay by a fast, non-radiative transition into the level E_2 . If the E_3 to E_2 transition probability is larger than that of E_3 to E_0 , then if E_3 is unstable, population will shift to E_2 - the upper level of the laser. If E_2 is metastable, population will increase with the cascade of population from higher levels - like E_3 . Here, there are four energy levels, energies E_0, E_1, E_2, E_3 , and populations $N_0, N_1, N_2,$

N_3 , respectively. The energies of each level are such that $E_0 < E_1 < E_2 < E_3$. As before, the presence of a fast, radiationless decay transition results in population of the pump band being quickly depleted ($N_3 \approx 0$). In a four-level system, atoms in the lower laser level E_1 are also quickly deexcited, leading to a negligible population in that state ($N_1 \approx 0$). That is, as long as $N_2 > 0$, then $N_2 > N_1$ and a population inversion is achieved. Thus optical amplification, and laser operation, can take place at a frequency of ν_{21} ($E_2 - E_1 = h\nu_{21}$).

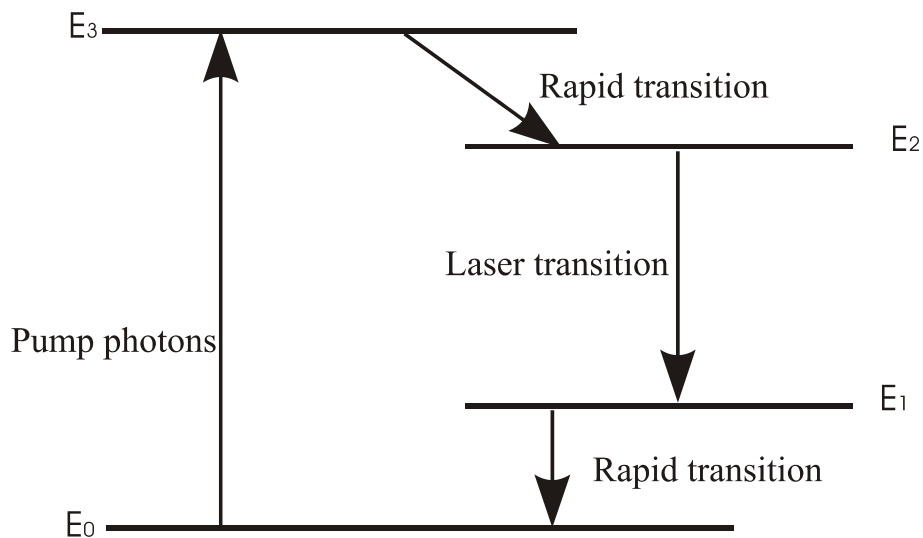


Fig. 11 Principle of the population conversion of a four-level transition.

The host of Nd:YAG laser is an insulating crystal $Y_3Al_5O_{12}$ (Yttrium Aluminium Garnet (YAG))- a cubic symmetry crystal, which is transparent from 0.3 to 5.5 μm and has a refractive index of 1.823 [103]. The active medium is triply ionized neodymium, which is optically pumped by a flash lamp whose output matches principle absorption bands in the red and infrared region. Excited electrons by the lamp flash quickly drop to the $^4F_{3/2}$ level, the upper level of the lasing transition, where they remain for a relative long time (about 230 μs). The most probable lasing is to the $I_{11/2}$ state, emitting photons with a wavelength of 1064 nm (Fig. 12).

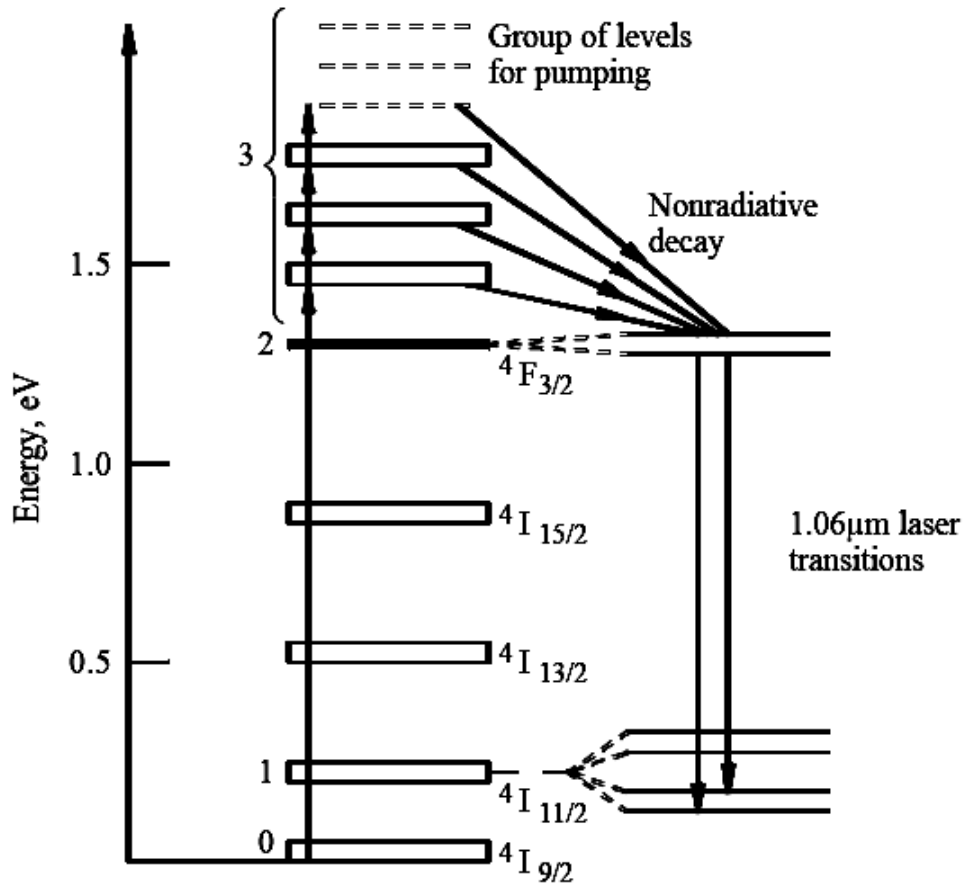


Fig. 12 Energy transitions of neodymium-doped yttrium aluminium garnet (Nd:YAG)

3.1.2 Construction of the Q-switched Nd:YAG laser

With just an active medium and resonator, laser light can be emitted once the flash lamp fires. However, the short pulse with a high peak power is the key to the usefulness of the pulsed Nd:YAG laser. Its peak power permits wavelength conversion through several nonlinear processes, such as frequency doubling, frequency mixing, or dye laser pumping. The pulsed laser pulse is achieved by introducing a Q-switch into the cavity to prevent oscillation.

Fig. 13 shows the schematic construction of the pulsed Nd:YAG laser with a typical Q-switch made of a polarizer, a quarter wave plate, and a Pockels cell. Pockels cells are used because of their low voltage requirements – 4 kV here instead of the Kerr cell which requires very fast switching of high voltages. If a high voltage is applied to the Pockels cell, the crystal changes

its polarization retardation characteristics and thus its losses. With no voltage applied, the Pockels cell does not affect the polarization of the light passing through it. During the Q-switched operation, the flash lamp excites for about 200 μs and builds up a large population inversion. When the Pockels cell is fired, the loss changes and the resultant laser pulse is less than 10 ns in duration and peak laser power can reach 200 MW at the fundamental wavelength.

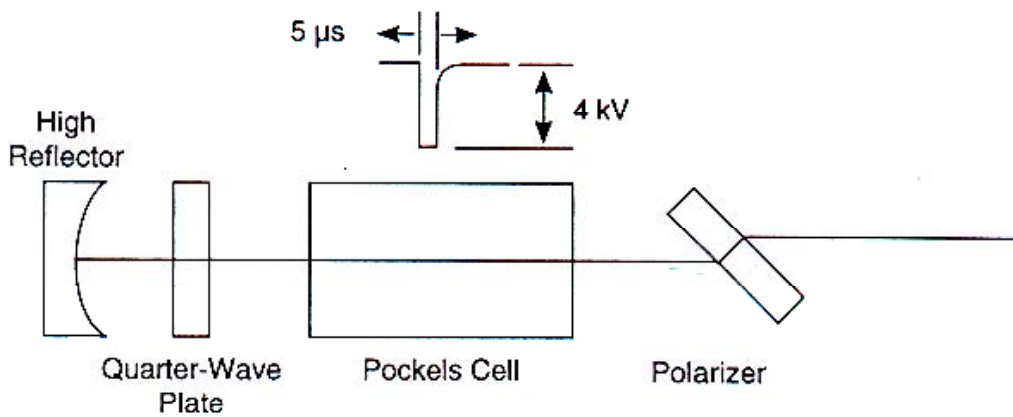


Fig. 13 Nd:YAG laser with a Q-switch made of Pockels cell, polarizer and quarter-wave plate.

3.1.3 Properties of Nd:YAG laser used in this experiment

The laser parameters associated with LIL are wavelength, pulse width, fluence, coherent length, as well as beam profile. Table 1 lists the most important parameters of the Nd:YAG laser made by Spectra Physics [104].

Another feature of Nd:YAG laser which is especially important for laser interference lithography is its good coherency. The coherence length (L_c)---the distance over which the output beam maintains a fixed phase relationship---is reciprocally proportional to the linewidth:

$$L_c = \frac{c}{\Delta\nu} \quad \text{Eq. 3-1}$$

where c is light velocity and $\Delta\nu$ is linewidth. Taking linewidth 6 GHz as an example, the coherence length is 50 mm. This is good enough for making laser interference with large angle between the interfering beams (small pattern period). For an interference with small angle, larger coherence length is needed, which is achieved by using injection seeder. The main concept is the synchronization of laser emission by an outside laser source with very narrow linewidth. Through the model 6350 injection seeder the linewidth is reduced from 30 GHz to 0.1 GHz, which corresponds to the coherence length of more than 1 meter.

Table 1 Important parameter of laser used in this experiment

Wavelength [nm]	Energy [J/cm ²]	Pulse width [ns]	Repeated rate [Hz]	Energy stability
1064	2.0	10	10	4%
532	1.0	10	10	6%
355	0.55	10	10	8%
266	0.18	10	10	16%

Laser beams often approaches Gaussian beams whose transverse profiles of the laser intensity with a power P can be described with a Gaussian function

$$I(r, z) = \frac{P}{\pi w(z)^2 / 2} \exp\left[-2 \frac{r^2}{w(z)^2}\right] \quad \text{Eq. 3-2}$$

where the beam radius $w(z)$ (the distance from the beam axis where the intensity drops to $1/e^2$ (about 13.5%) of the maximum value) varies along the propagation direction:

$$w(z) = w_0 \sqrt{1 + (z/z_R)^2} \quad \text{Eq. 3-3}$$

with the Rayleigh length

$$z_R = \frac{\pi w_0^2}{\lambda} \quad \text{Eq. 3-4}$$

The wavelength λ is the value in the medium (i.e., not the vacuum wavelength). Beyond the Gaussian shape of the intensity profile, a Gaussian beam has a transverse phase profile which is either flat or parabolic (i.e., with the phase deviation being proportional to the radial position). The electric field is:

$$\vec{E}(r, z) = E_0 \frac{w_0}{w(z)} \exp\left[-\frac{r^2}{w(z)^2}\right] \exp\left\{-i\left[kz - \arctan\frac{z}{z_R}\right] + \frac{kr^2}{2R(z)}\right\} \quad \text{Eq. 3-5}$$

with the wavenumber $k = 2\pi/\lambda$ and the radius of curvature of the wavefronts

$$R(z) = z[1 + (z_R / z)]^2 \quad \text{Eq. 3-6}$$

The smallest beam radius w_0 is obtained at the so-called beam waist (for $z = 0$), where the phase profile is flat.

3.2 Materials

Polymers were selected according to following criteria: they must be biocompatible and possess high laser absorption coefficient at the wavelength of the Nd:YAG laser. Besides, they must be transparent so that cell photographs can be taken by using scanning laser confocal microscopy.

Transparent Thermanox® film from Nunc Inc., which is often used as standard substrate in cell culturing, was selected because of its biocompatibility and light sensitivity at 266 nm. According to the information from the producer (Nunc Inc.), one side of the film is relatively more hydrophilic, and is recommended to be suitable for cell culture. We denote this side as TXL, correspondingly another side as TXB. However, no detailed information about the chemical component is released by the company. According to our ATR-FTIR (attenuated total reflection Fourier transformation infrared spectroscopy) analysis (Fig. 14), it mainly consists of poly(ethylene terephthalate) (PET), but modified in bulk and at surface.

Amorphous PET and polycarbonate (PC) films were received from Goodfellow GmbH (Bad Nauheim, Germany). Thermanox was used as received, while PET and PC films were first cleaned with isopropanol. The chemical structures of PET and PC are shown in Fig. 15.

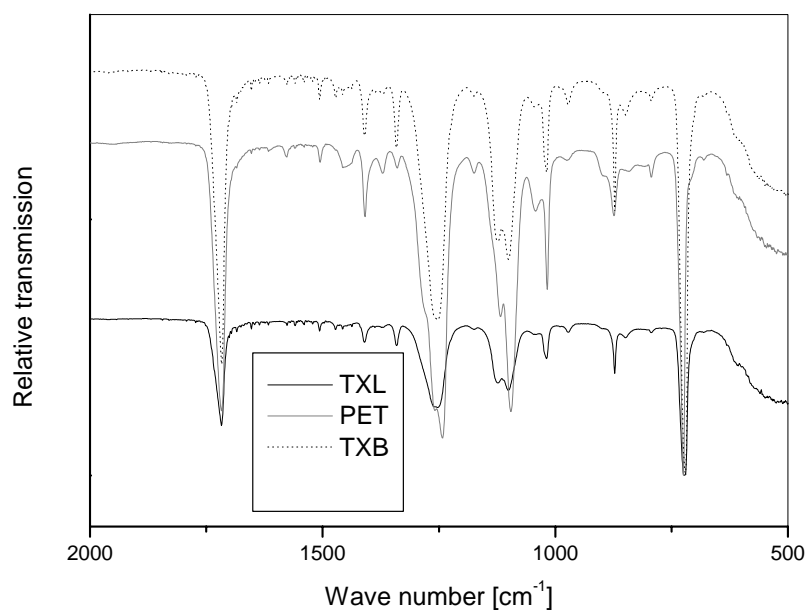


Fig. 14 IR spectra of PET and Thermanox

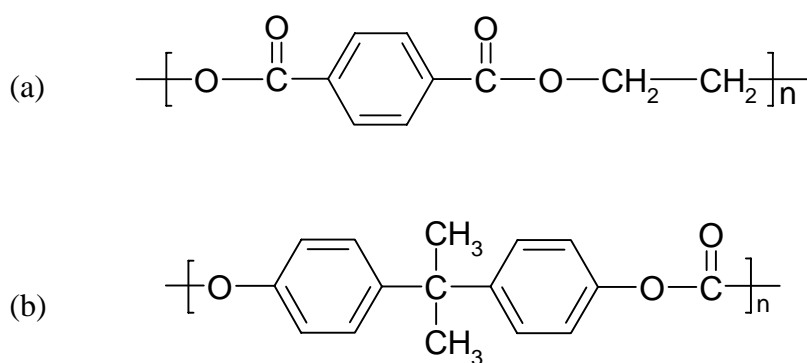


Fig. 15 Chemical formula of materials used in the experiment. (a) poly(ethylene terephthalate), (b) polycarbonate.

3.3 Characterization of the micropatterns and ablation craters

The micropatterns and ablation craters were characterized by white light interferometry (WLI), atomic force microscopy (AFM) and scanning electron microscopy (SEM). WLI measurement gives 3-D images with high vertical resolution and can be performed within a few minutes, which was used to control the patterning process and measure the pattern depth; while more topographical information was obtained from AFM images. SEM provides 2-D images with higher lateral resolution.

3.3.1 White light interferometry

WLI measurements were performed using a NewView 200 white light interferometer (NewView 200 3D Imaging Surface Structure Analyser, Zygo Corporation, USA). The operating principle of this instrument is the interference pattern formed by a reference and a specimen beam with path difference, which is described elsewhere [105]. A light beam from a tungsten halogen lamp is split by an objective lens. One of the beams is focused onto the specimen surface and another onto an inner reference plane. After reflection, the two beams are superimposed one to another in the interferometer. By accurate vertical scanning, produced by a Piezo electrical measurement converter (PZT), and a camera able to measure the intensity of the individual pixels, a three dimensional interferogram of the surface is produced. A quantitative 3D-image is then produced from computer calculations by Frequency Domain Analysis.

3.3.2 Atomic force microscopy

Micropatterns were characterized by means of atomic force microscopy (AFM) (Digital Nanoscope IV Bioscope, Veeco Instruments, Santa Barbara, CA). All measurements were

performed in Tapping modeTM using a commercial pyramidal tip (NCH-W, Veeco Instruments) on a cantilever with a length of 125 μm , a resonance frequency of about 220 kHz and a nominal force constant of 36 N/m. The scan speed was proportional to the scan size, and the scan frequency was between 0.5 and 1.5 Hz. Images were obtained by displaying the amplitude signal of the cantilever in the trace direction, and the height signal in retrace direction; both signals being simultaneously recorded.

3.3.3 Scanning electron microscopy

Since the polymers used aren't conductive, the static electricity caused by free electrons may decrease the resolution. Therefore, a layer of 10 nm Au/Pb was sputtered to the polymer surface before SEM measurement. SEM photographs were taken in a FIB / SEM DualBeam system (Strata DB, 235, FEI) which combines a scanning electron microscope with a focused ion beam (FIB) system for nanoscale erosion of the sample. The ion-beam system has a gallium metal ion source giving a high-brightness ion beam which can cut structures on the scale of nanometers. The instrument can be used for preparing samples for transmission electron microscope (TEM) from specific areas of the specimen, as well as for undertaking a wide range of experiments in this nanofabrication facility. The system is equipped with a high-performance field-emission microscope.

3.4 Laser ablation of polymers

To understand laser ablation mechanisms, it must be known what happens during ablation. At first the laser ablation curves were plotted and photographs on ablation craters were taken with SEM. XPS were used to characterize the chemical surface modification, while the emitted ions, small molecules and polymer segments were analyzed by ToF-MS.

3.4.1 Ablation curves

The laser beam was focused to 0.8 mm in diameter which was measured using a black photo paper. The polymer samples were irradiated with 1, 5 and 10 pulses under different fluence. The ablation depth was measured with WLI as shown in Fig. 16. The ablation curves were plotted by drawing the ablation rate ($\mu\text{m}/\text{pulse}$) against laser fluence.

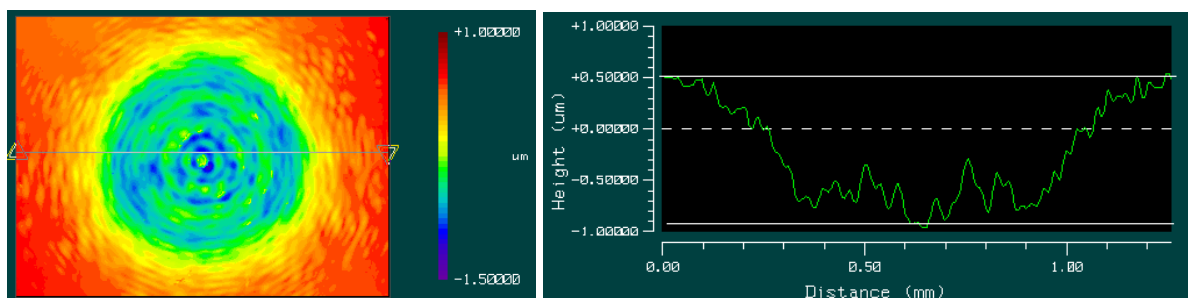


Fig. 16 Ablation craters for ablation curves taken by WLI.

3.4.2 XPS analysis

The chemical surface modification after irradiation was analyzed by using XPS. Since the lateral resolution is not enough to measure the chemical composition of different positions on the LIL-induced micropatterns, XPS samples were treated with one laser beam under different fluence in order to find the influence of the fluence on the polymer chemical composition. In order to measure several samples at one time and reduce the influence of static electricity, the following copper sample carrier was designed (Fig. 17).

All the samples were fixed at the back of the copper carrier and introduced in the XPS chamber immediately after the laser treatment. The XPS analysis was performed on a Surface Science Instrument (M-Probe) operating with an Al $K\alpha$ radiation and an instrumental resolution of ca. 0.8 eV. The pressure of the analyser chamber remained below 2×10^{-9} mbar

during the measurement. Due to poor conductivity of the PET and Thermanox films, a flood gun was regulated to compensate the charge within the films.

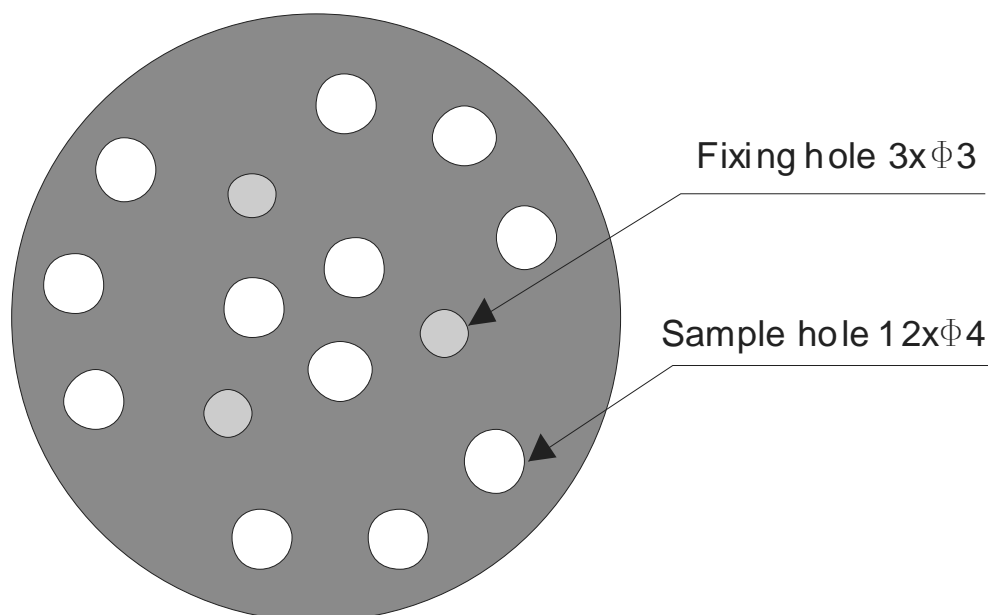


Fig. 17 Copper sample carrier for XPS analysis of laser ablated polymers (thickness 1 mm, diameter 40 mm). Three small holes are used to fix the carrier and the other 12 holes with a diameter of 4 mm are used to fix the samples.

3.4.3 Contact angle

The water wettability of the polymers after laser treatment was measured with a video-based contact angle meter (OCA 20, Dataphysics, Germany). The micro-controller module allows automation of the liquid handling as well as measurement. The static contact angles and the dynamic wetting angles, i.e. advancing and receding angles, can be measured with this device using a fixed dosing volume. For particularly small or large contact angles, the system provides an increased measuring accuracy as well as an automatic detection of the solid surface. Under every fluence, three samples were treated with one laser pulse (one beam) and measured at 23 °C and 60% humidity immediately after laser ablation.

3.4.4 Time of flight mass spectroscopy

ToF-MS is a powerful instrument to investigate the laser ablation mechanism since it provides direct evidence to laser ablation process. The mass spectrometer used is a linear ToF-MS (shown in Fig. 18) which was developed at the Institut für physikalische Chemie at Christian Albrechts Universität zu Kiel. The ion source and the flight pipe (Leybold, Köln, Germany) are evacuated through a turbo (Pfeiffer Vacuum, Asslar, Germany) to 10^{-6} mbar. The ion source region and the flight pipe are separated by a tunable valve.

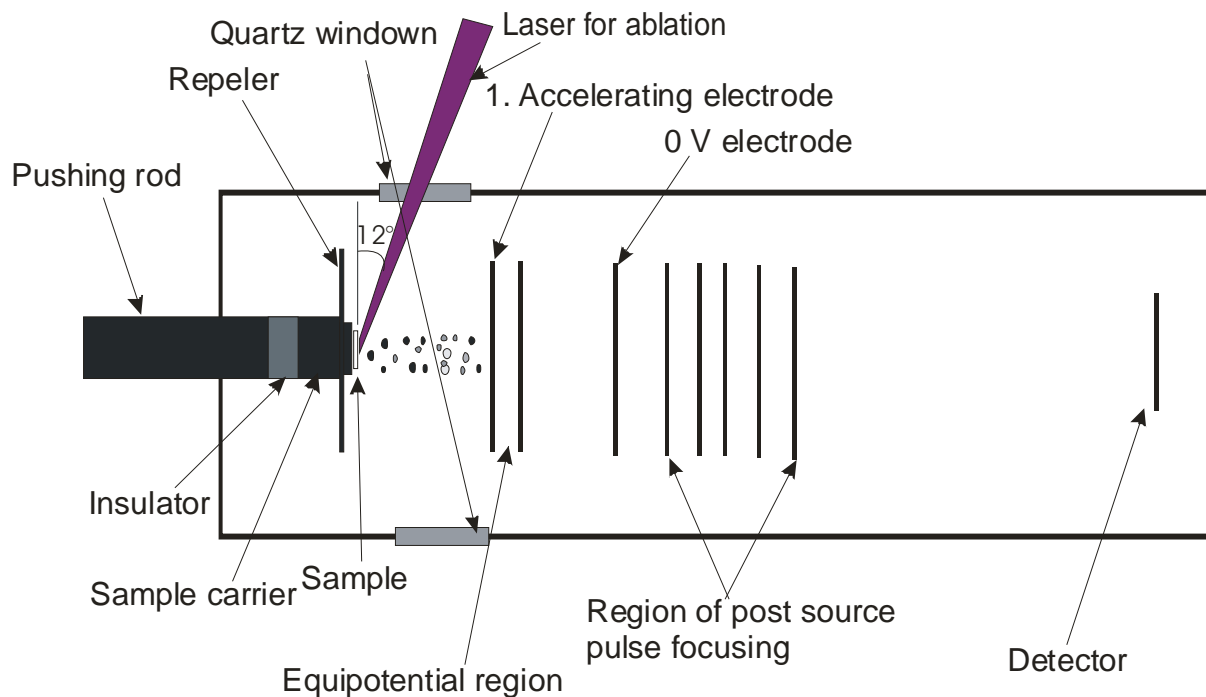


Fig. 18 Schematic setup of the ToF-MS instrument and its working mechanism (according to [106])

The Disadvantage of ToF-MS is the low resolution which is influenced by the following 4 factors:

- time unsharpness,
- position unsharpness,

- energy unsharpness,
- speed unsharpness.

Time unsharpness is caused by the different time at which the ablation ions are formed. Here the pulse width plays an important role. The ions produced in different spatial position result in position unsharpness. An ideal ToF-MS spectrum can be measured when the ions are limited in a small spatial area. The energy unsharpness comes from the different speed of the ions obtained during laser ablation, while the speed vector and speed distribution result in speed unsharpness.

To carry out ToF-MS measurements, the samples were punched from the films, cleaned with alcohol and adhered onto the stainless steel sample carrier. Then, they were supplied through a lock device which was evacuated to 10^{-6} mbar with a membrane pump. The 266 nm laser beam was directed to the polymer sample at an angle of 78° with respect to the surface normal. ToF-MS spectra were measured under different laser fluence and pulse number.

3.5 Laser ablation of thin polymer solution

1% (w/w) PC solution was obtained by resolving PC granulate in tetrahydrofuran (THF) under shaking. 1 g PC solution was filled in a standard quartz cuvette (10×10×45 mm) with PTFE (polytetrafluorethylene) stopper so that the concentration of the solution was not changed during laser ablation and molecular weight measurement. The experimental set-up is shown in Fig. 19. The original laser beam is about 8 mm in diameter, which was cut to 7 mm on the sample. The solution was irradiated with different number of pulses under different fluence. The solution was always protected from light before and after laser irradiation.

The number average molecular weight (M_n) of the as-received and laser-ablated PC was measured using gel permeation chromatography (GPC) (Waters GmbH, Column: Nucleogel GPC 103-5, Macherey & Nagel). The resolution region is 1000-100,000 Da.

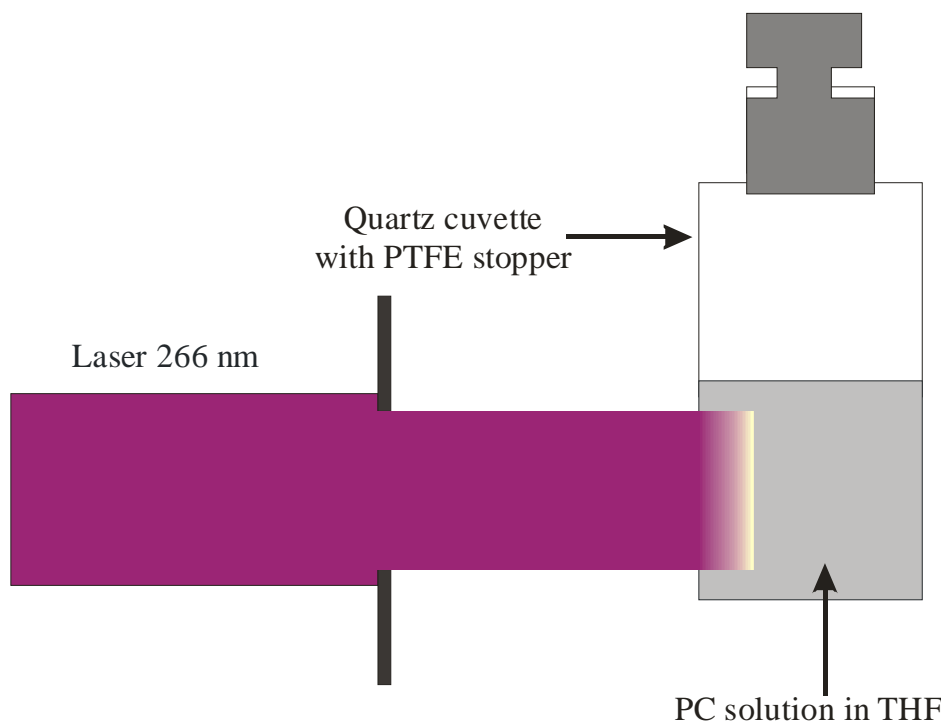


Fig. 19 Experimental setup for laser ablation of thin polymer solution

3.6 Laser interference lithography

The experimental set-up of two-beam LIL is shown in Fig. 20. The laser beam was split into two equal beams, which were then guided by the mirrors and focused by optical lenses to superimpose on the sample surface to form an interference pattern. The linear micropatterns were then duplicated to polymer surfaces through laser ablation of polymers. 3-D patterns (also called as point patterns) were produced by means of rotating a line-patterned sample 90° about z-axis and repeating the above process (two-step process). Adjusting the laser fluence and the angle (θ), the patterns with different depth and period were obtained.

In this work the 4. harmonic laser beam with a wavelength of 266 nm was selected because the photon has higher energy and the polymers possess higher absorption efficient (for PET about 4000 cm^{-1}) at this wavelength. The micropatterns were characterized with WLI, AFM and SEM.

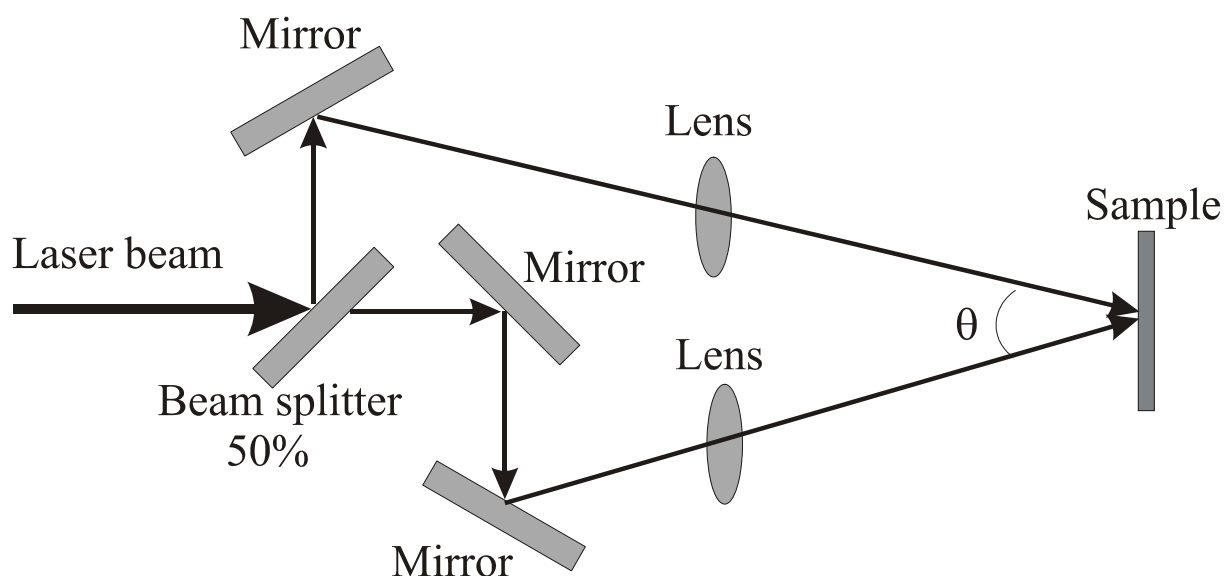


Fig. 20 Experimental setup of two-beam laser interference lithography [64]

3.7 Cell culturing on micropatterned polymer surfaces

3.7.1 Culturing of mouse fibroblasts on micropatterned Thermanox

4 linear micropatterns were prepared with LIL on each side of Thermanox for culturing of mouse fibroblast cells. The period and depth measured with WLI are shown in Table 2.

The mouse fibroblast line L929 was kindly provided by Prof. P. Mestres of Department of Anatomy, Saarland University. L929 cells were cultured in 15 mL/flask of Dulbecco's Modified Eagle's Medium (Sigma), which was supplemented with 10% fetal calf serum (FCS) (Gibco Invitrogen Corporation, Gaithersburg, MD) and 10% antibiotic antimycotic solution including 100 IU/mL penicillin, 100 g/mL streptomycin sulfate, and 0.025 g/mL amphotericin B. Cell culture flasks were kept in a humidified incubator (37°C/5% CO₂) for four days until confluence was reached.

Table 2 Thermanox patterns for cell culturing induced by ILI

Polymer	Type of pattern	Period [μm]	Fluence [J/cm^2]	Depth [μm]
TXL	line	1.26	0.10	0.68 ± 0.079
TXB	line	1.26	0.10	0.86 ± 0.067
TXL	line	2.08	0.50	1.39 ± 0.082
TXB	line	2.08	0.50	1.38 ± 0.072
TXL	line	5.05	0.49	1.26 ± 0.072
TXB	line	5.05	0.49	1.32 ± 0.066
TXL	line	9.69	0.49	0.93 ± 0.062
TXB	line	9.69	0.49	0.94 ± 0.089

Each of the four laser-patterned TXL and TXB including the controls were placed separately into a 24-wells culture plate (Greiner Labortechnik, Frickenhausen Germany). The samples in the wells were disinfected by treating with 70% alcohol for 15 min, and air-dried for another 15 min under a lamina-flow hood. Then, the disinfected samples were washed three times with 1 mL Hanks Balanced Salt Solution (HBSS) (BD Biosciences, Heidelberg, Germany). Afterwards, the samples were coated each with 1 mL 0.1% collagen type I Rat Tail in HBSS at room temperature for two hours, aspirated, and washed three times again with 1-mL HBSS. L929 cells were trypsinated, counted, and 150 000 cells/mL (7.46×10^4 cells/cm²) L929 were seeded onto each of the TXL and TXB samples in 1 mL/well of culture medium mentioned above, and were kept in humidified incubator (37 °C/5% CO₂) for over night until sub-confluence was reached. Then, the cells were fixed and stained the next day for light microscopic analysis. Unstained cells were used for AFM characterization.

3.7.2 Culturing of human pulmonary fibroblasts on patterned PET and TXL

Linear micropatterns with a period of 2, 3, 4, 5, 6, 7 and 8 μm were produced on PET and TXL surfaces for culturing of human pulmonary fibroblasts (HPF). The depth of each pattern was measured with AFM, which is shown in Table 3.

Table 3 PET and TXL patterns for cell culturing prepared by ILI

Polymer	Type of pattern	Period [μm]	Laser fluence [J/cm^2]	Depth [μm]
PET	line	2	0.25	0.62 \pm 0.006
PET	line	3	0.27	0.57 \pm 0.02
PET	line	4	0.34	0.71 \pm 0.06
PET	line	5	0.34	0.86 \pm 0.03
PET	line	6	0.37	0.80 \pm 0.02
PET	line	7	0.32	0.71 \pm 0.02
PET	line	8	0.38	0.55 \pm 0.006
TXL	line	2	0.14	0.77 \pm 0.06
TXL	line	3	0.18	1.18 \pm 0.05
TXL	line	4	0.27	1.36 \pm 0.02
TXL	line	5	0.21	1.00 \pm 0.2
TXL	line	6	0.24	1.06 \pm 0.06
TXL	line	7	0.24	1.17 \pm 0.05
TXL	line	8	0.28	1.25 \pm 0.05

Two sets of PET and TXL micropatterns were placed into a 24-wells culture plate. An extra culture plate was used for two sets of micropatterned PET and TXL. All samples were submerged in 1 ml of 70% alcohol for 30 min for disinfections, and air-dried for 45 min under a lamina-flow hood. Afterwards, one set of laser-micropatterned and as-received TXL and PET samples were coated with 1 mL 0.1% collagen (type I Rat Tails, BD Biosciences) in

HBSS at room temperature for two hours, aspirated, and washed three times with 1 mL HBSS (pH 7.4). The previously cultured human pulmonary fibroblasts were trypsinated, counted and 50000 cells ($\sim 2.49 \times 10^4$ cell/cm²) were seeded onto each of the samples in 1 mL/well of Dulbecco's modified Eagle medium (DMEM) (10% FCS). The cell cultures were kept in humidified incubator (37°C/5% CO₂) for two days until 85% confluence was reached.

Prior to staining, the cells were air-dried for overnight. Then, they were stained with May-Gruenwald Stain for 15 min, submerged in phosphate buffer (isotonic, pH 7.2) for 3 min, stained again with Giemsa Stain for 20 min, and washed in phosphate buffer (isotonic, pH 7.2). Cells were then investigated under white light microscope, and pictures were taken.

3.7.3 Culturing human pulmonary fibroblasts on patterned PC

Linear and point micropatterns with a period of 3, 5, 7 and 9 μm , respectively, were prepared on PC films, whose period and depth were measured with WLI and are given by Table 4.

Table 4 PC patterns for cell culturing induced by ILI

Polymer	Type of pattern	Period [μm]	Fluence [J/cm^2]	Depth [μm]
PC	line	3	0.37	0.63 \pm 0.025
PC	point	3	0.37 \pm 0.37	0.88 \pm 0.066
PC	line	5	0.37	0.58 \pm 0.10
PC	point	5	0.37 \pm 0.37	0.86 \pm 0.12
PC	line	7	0.37	0.67 \pm 0.099
PC	point	7	0.37 \pm 0.37	1.12 \pm 0.12
PC	line	9	0.37	0.65 \pm 0.072
PC	point	9	0.37 \pm 0.37	1.00 \pm 0.050

Linear and point PC micropatterns were punched into circular disks with diameter of 8 mm. The disks were placed into a 24-wells culture plate (Greiner Labortechnik, Frickenhausen, Germany), soaked in 1 mL 70% alcohol for 30 min for disinfections, and air-dried for 45 min under a lamina-flow. Then, they were washed three times with PBS (pH 7.4, 1 mL/wash), and coated with 1 mL 0.1% collagen (type I Rat Tails, BD Biosciences, Heidelberg, Germany) in PBS at 37 °C for two hours, aspirated, and washed three times with phosphate buffered saline (PBS) (pH 7.4, 1 mL/wash) again. In addition, PC disks without surface pattern were treated equally, and used for comparison purpose.

The previously cultured human pulmonary fibroblasts were trypsinated, counted, and 50000 cells ($\sim 2.49 \times 10^4$ cell/cm²) were seeded onto each of the PC disks in 1 mL/well of DMEM (10% FCS) (Gibco Invitrogen Corporation, Gaithersburg, MD). The cell cultures were kept in humidified incubator (37 °C/5% CO₂) for three days until 85% confluence was reached.

After having been air-dried for overnight, the HPF seeded on PC disks were stained with May-Gruenwald Stain (Merck KGaA, Darmstadt, Germany) for 15 min, submerged in phosphate buffer (isotonic, pH 7.2) for 3 min, stained again with Giemsa Stain (Merck KGaA, Darmstadt, Germany) for 20 min, and washed in phosphate buffer (isotonic, pH 7.2). Cells were then investigated under Olympus CK2 white light microscope, and pictures were taken directly with Olympus C-505Zoom digital camera.

The pictures (20 x magnification) were then used for measurement of cell number and cell length. Three squares (10 cm x 10 cm) in each picture were chosen, the cell number was then counted within each selected area, and the average of the total cell number in the three selected squares was calculated (n = 3). In addition, the cell lengths were obtained by selecting cells in each picture randomly (n = 10), measuring the longitude and latitude lengths with a ruler, and multiplying the measured lengths with the magnification factor of the microscope.

3.7.4 E-selectin expression

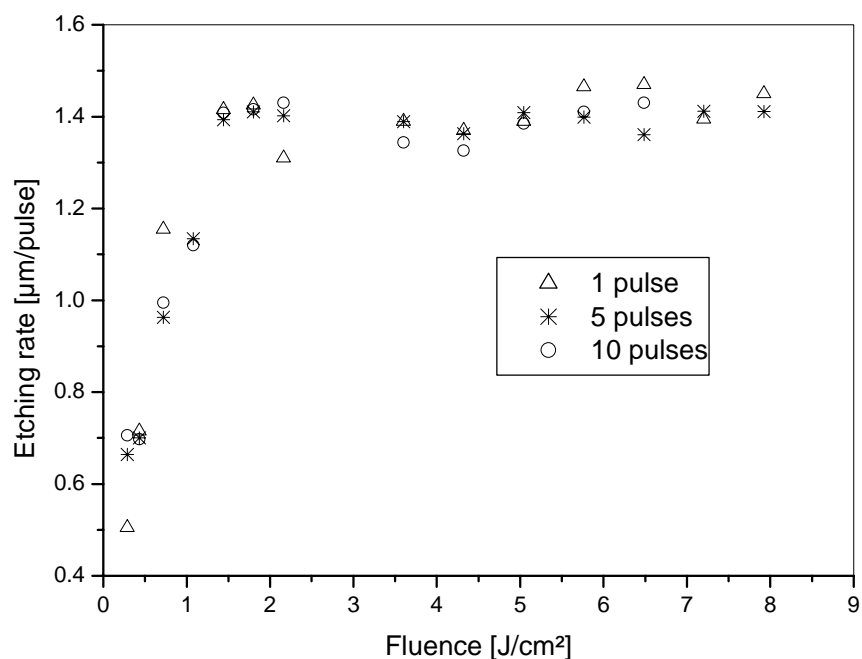
The HPF seeded on PC disks were washed 3 times with PBS (1mL/wash) before incubation with 500 μ L/disk primary antibody, mouse anti-Human E-selectin (1:500 dilution in PBS containing 1% (w/v) BSA) (DAKO, Hamburg, Germany) for 60 min. Afterwards, the cells were washed 3 times with PBS containing 1% (w/v) BSA (1mL/wash), and then incubated with 500 μ L/disk secondary antibody, goat anti-Mouse-FITC (1:500 dilution in PBS containing 1% (w/v) BSA) (DAKO, Hamburg, Germany) for another 60 min. Finally, the cells were washed 3 times with PBS (1 mL/wash), embedded in FluorSave anti-fade medium (Calbiochem, Bad Soden, Germany), and the images were taken by a confocal laser scanning microscope (MRC-1024).

4 Results

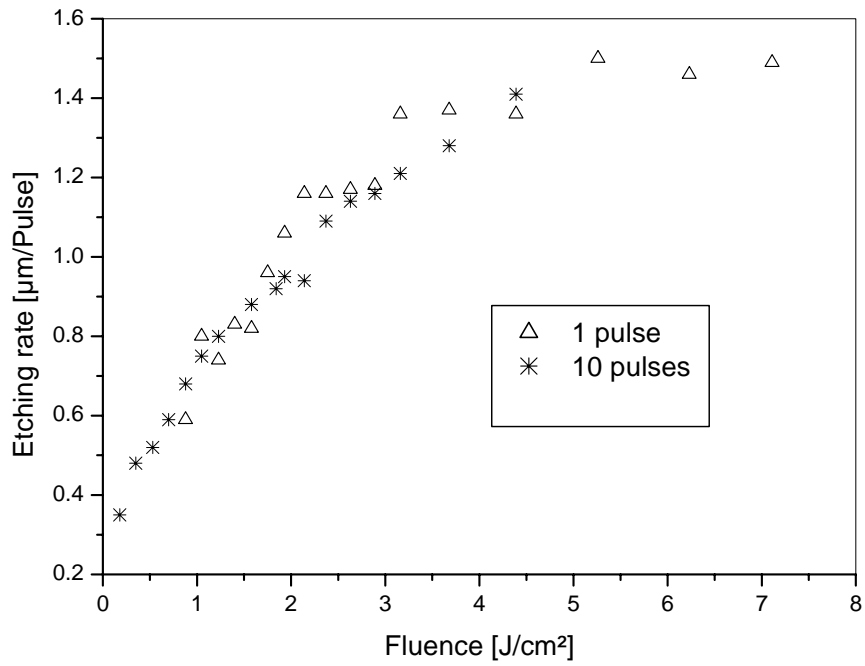
4.1 Laser ablation polymer films

4.1.1 Laser ablation curves

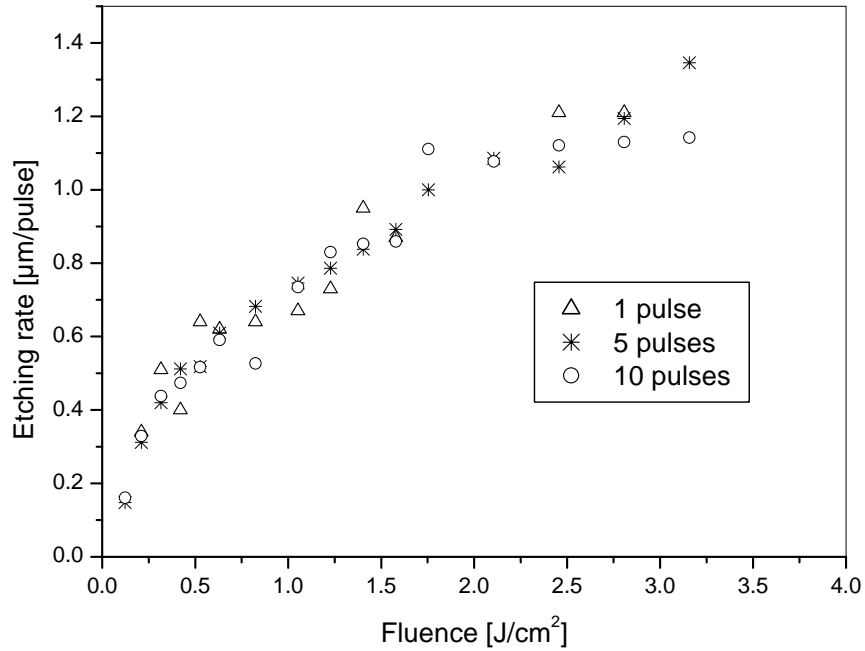
Laser ablation curves of PET, TXL and PC are shown in Fig. 21. The average etching rates from different pulses (1, 5 and 10 pulses) are similar for each polymer. The etching rate of PET increases with the fluence quickly until 1.4 J/cm², and then remains nearly stable at 1.4 μm/pulse with higher fluence (Fig. 21a); while those of TXL and PC increase gradually to a saturated etching rate of 1.5 μm/pulse at 5 J/cm² (TXL) and 1.2 μm/pulse at 2.5 J/cm² (PC), respectively (Fig. 21b and c). It is relatively difficult to define the ablation threshold since the ablation curves satisfy neither photochemical nor photothermal mechanism. Approximate thresholds of 0.2 J/cm² for PET, 0.1 J/cm² for TXL and 0.08 J/cm² for PC are obtained when the linear part of the logarithmic ablation curves are extrapolated to 0 μm/pulse.



(a)



(b)

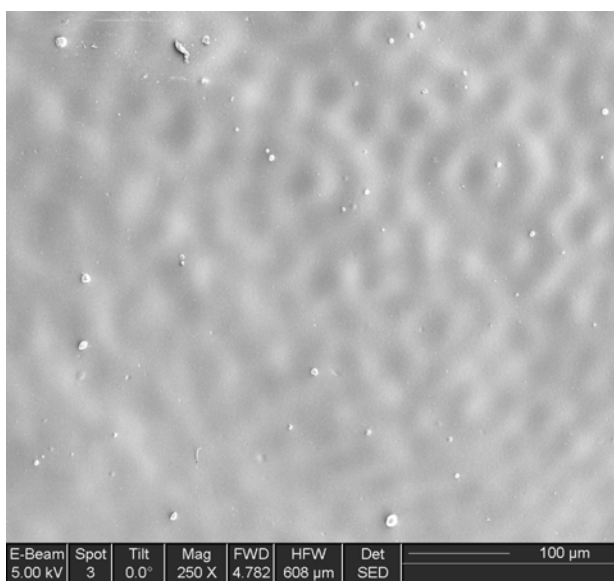


(c)

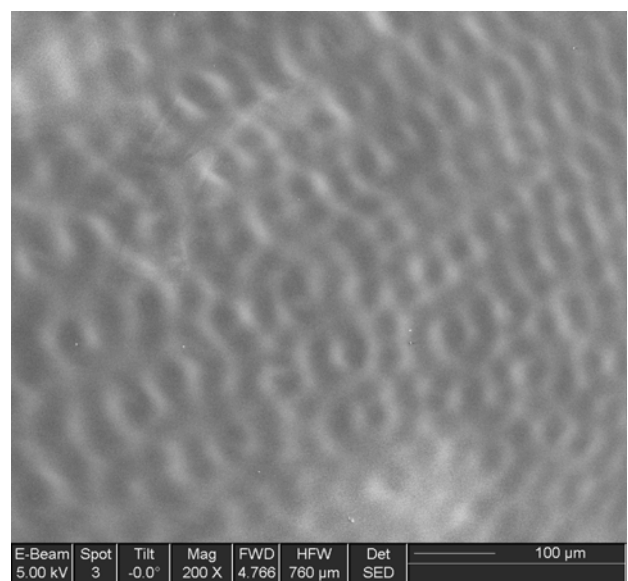
Fig. 21 Ablation curves of (a) PET, (b) TXL and (c) PC at 266 nm. The depth was measured by using WLI.

4.1.2 Morphology of laser ablation craters

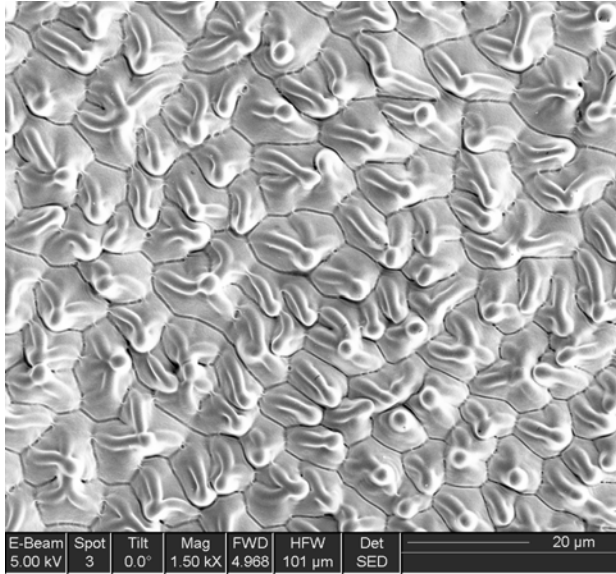
The ablation craters were characterized by SEM. The photographs of PET and PC show a relative smooth surface under different fluence although the surfaces possess also somewhat structures whose distance between two peaks is about 20 μm (Fig. 22a and b). However, very interesting microstructures were observed on irradiated TXL surfaces with 5 to 500 pulses under fluence from 0.055 to 7.2 J/cm^2 (Fig. 22c-i). Regular cracks appear after irradiation of 50 pulses under 0.1 J/cm^2 , whose dimension is about 3-10 μm (Fig. 22c and d). The structure is very similar to the texture of sintered ceramics. Similar structures can be observed under 0.055 J/cm^2 after 100 pulses. Nevertheless, the so-called ripples can be observed with fewer pulses. They show somewhat orientation, and the period falls between 2 and 5 μm . The protuberances are observed at the breaking positions or connecting point of two ripples. With much higher fluence, the ripples appear just after irradiation of several pulses. Under these conditions, the ripples have very clear orientation, and possess fewer protuberances. The distance between two ripples is about 5 μm . With 1 pulse, no microstructures are found under any fluence (Fig. 22j).



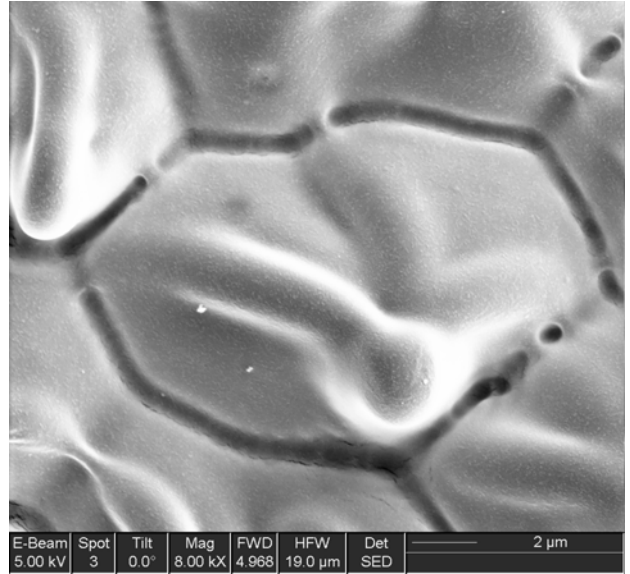
(a)



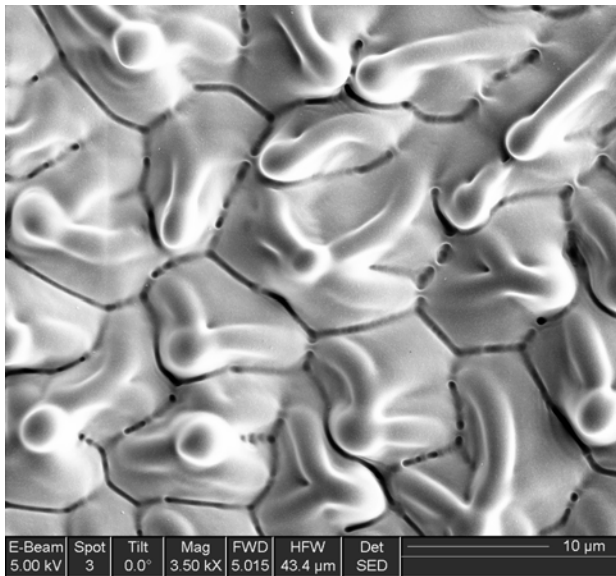
(b)



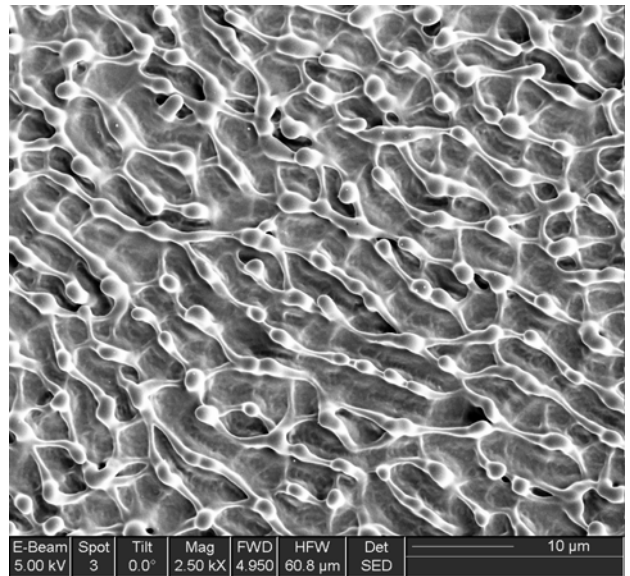
(c)



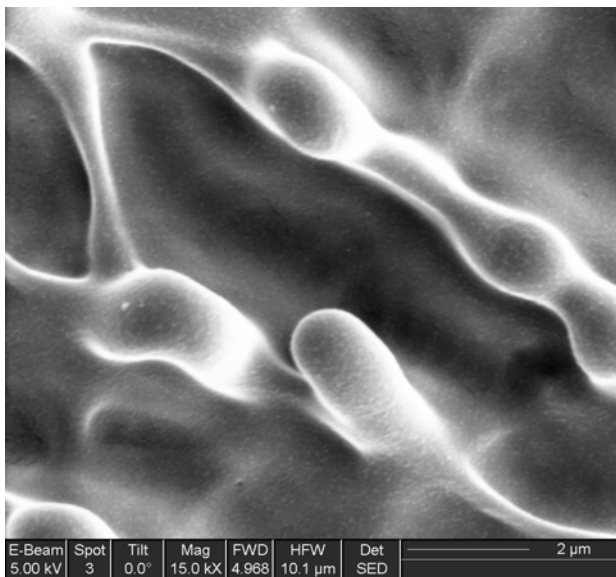
(d)



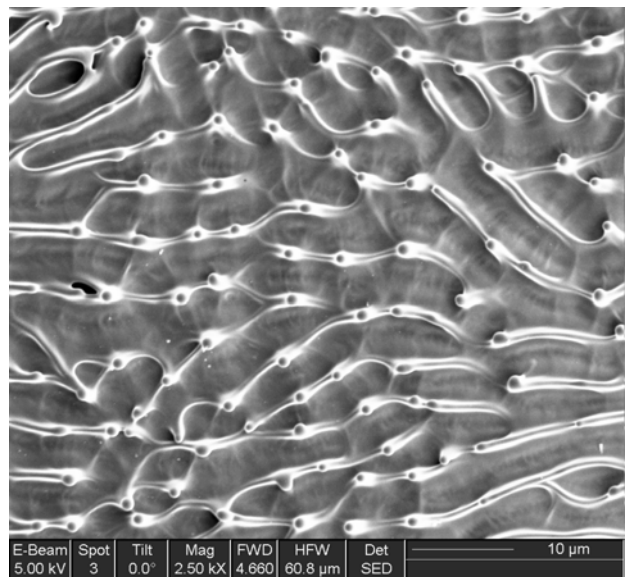
(e)



(f)



(g)



(h)

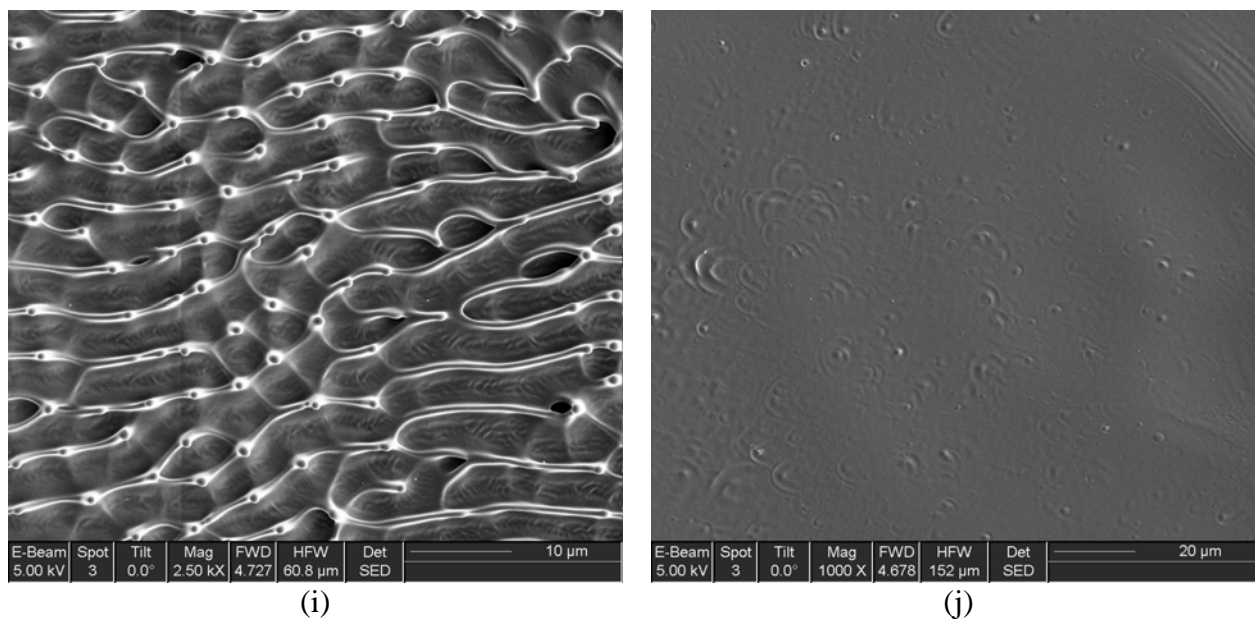


Fig. 22 SEM photographs of laser irradiated polymer surfaces. (a) PET: 0.14 J/cm², 50 pulses; (b) PC: 0.11 J/cm², 100 pulses; (c) TXL: 0.1 J/cm², 50 pulses; (d) TXL: magnification of (c); (e)TXL: 0.055 J/cm² 100 pulses; (f) TXL: 0.055 J/cm² 50 pulses; (g) TXL: magnification of (f); (h) TXL: 1.44 J/cm², 5 pulses; (i) TXL: 7.20 J/cm², 10 pulses; and (j) TXL: 7.2 J/cm², 1 pulse.

4.1.3 Contact angle

The influence of laser fluence on contact angle is shown in Fig. 23. The untreated PC (92°) has a larger contact angle than PET (76°) and TXL (67°). Laser treatment have reduced contact angle of all polymers used in this experiment. For PC it decreases about 10° under 0.3 J/cm² and 15° under 0.65 J/cm² treatments, while laser irradiation has less influence on PET and TXL by which the contact angle remains nearly unchanged when laser fluence exceeds 0.3 J/cm². Generally, all polymers are changed from hydrophobic to more hydrophilic after the laser treatment.

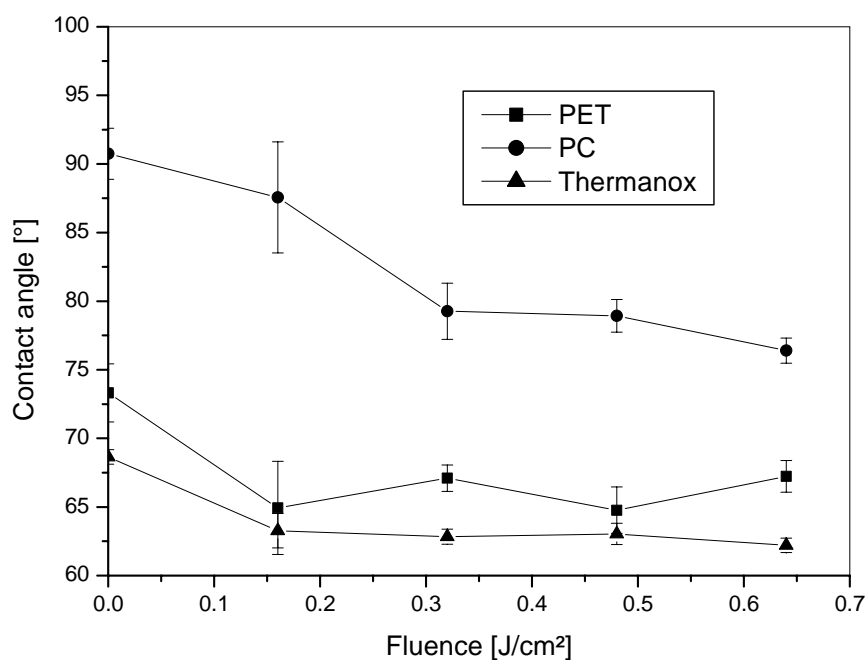


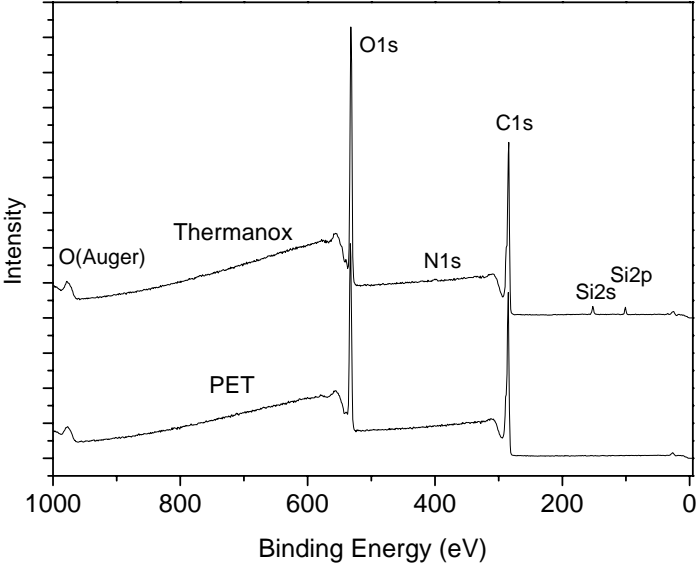
Fig. 23 Variation of the contact angle after laser ablation. The samples were treated by 1 pulse.

4.1.4 XPS analysis

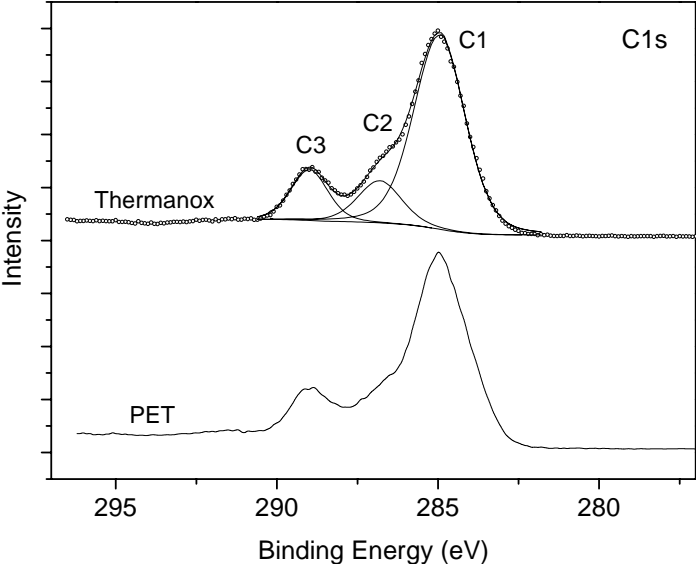
4.1.4.1 XPS analysis of PET and TXL treated with laser

The overview XPS spectra of PET and Thermanox (Fig. 24a) shows that Thermanox is composed of carbon and oxygen like PET, but of additional nitrogen and silicon, which indicate the biocompatible treatment of the Thermanox film. The C1s spectra of both films are enlarged in Fig. 24b. The labels C1, C2 and C3 due to different chemical surroundings are denoted as follows: C1 285.0 eV aromatic carbon, C2 286.8 eV carbon bearing single oxygen, C3 289.0 eV carboxylic carbon. The C/O ratio depending on laser fluence is shown in Fig. 25a. The C/O ratio of both non-treated films are different, although the other ratios related to laser treatment are similar. With increase of laser fluence, the O content decreases while the C

content increases. The relative weight of C species is shown in Fig. 25b. The trend of C species in both cases is similar whereas the C1 increased and saturated at a constant, and C2, C3 decreased gradually and reached a constant value.

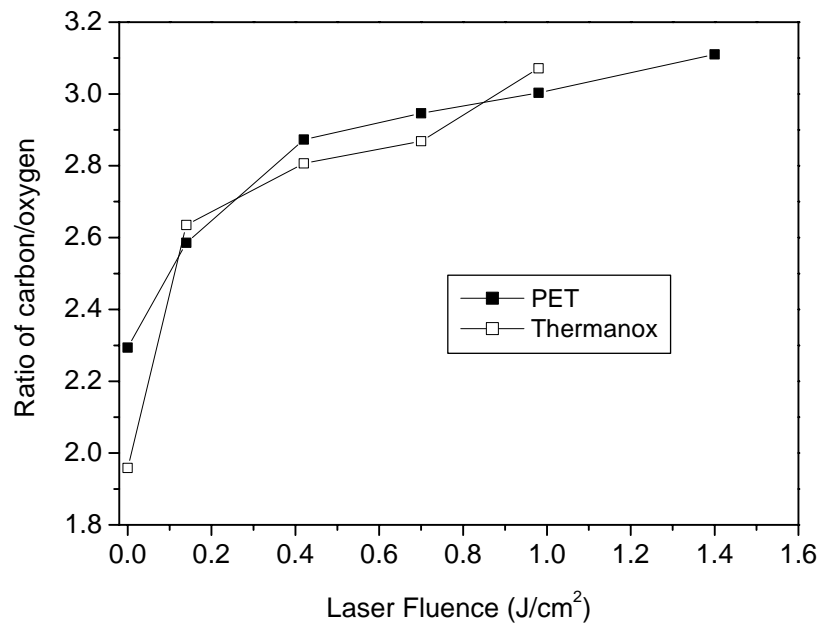


(a)

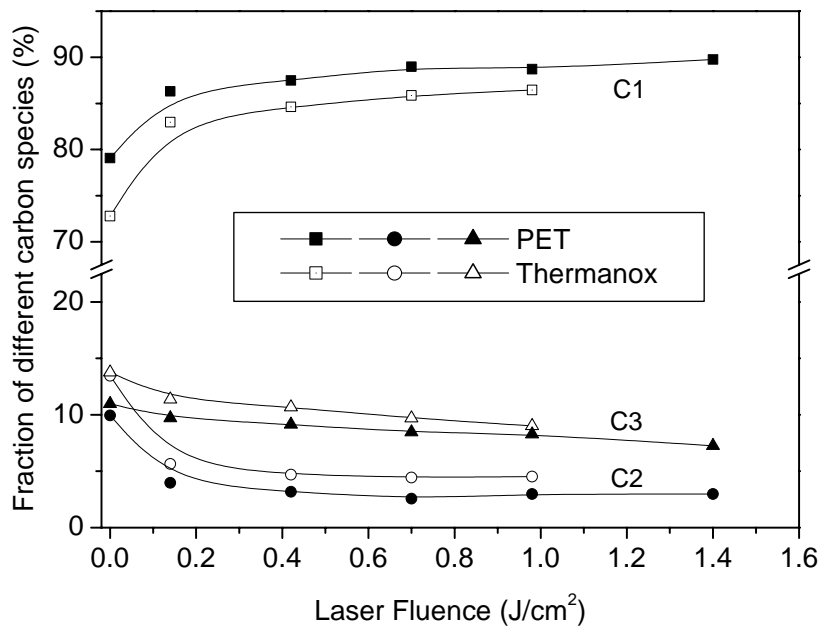


(b)

Fig. 24 (a) Overview and (b) C1s XPS spectra of non-treated PET and Thermanox samples. (C1: aromatic carbon, C2: carbon bearing single oxygen, C3: carboxylic carbon) [64].



(a)

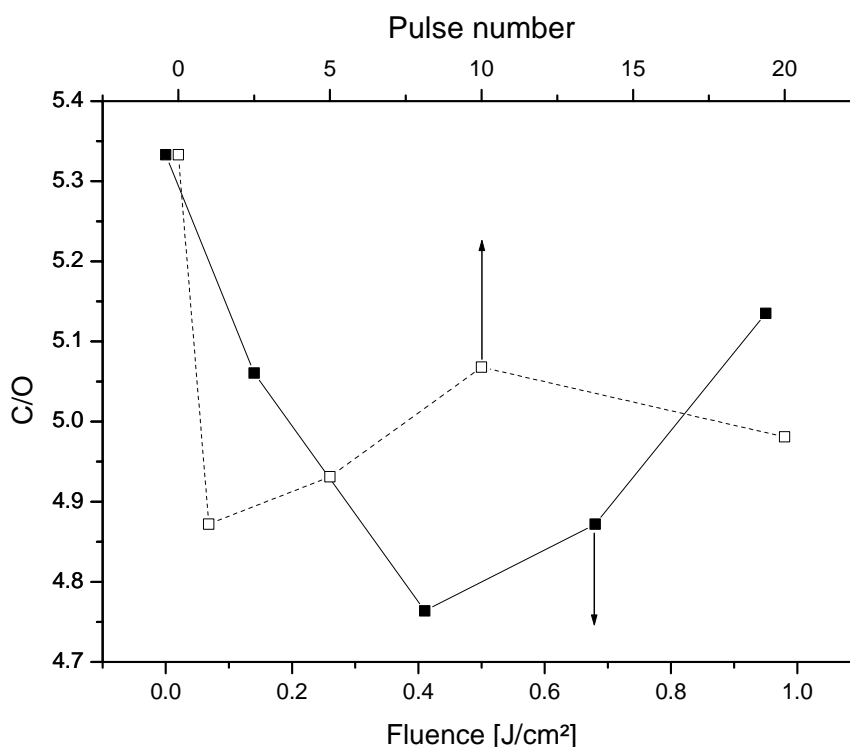


(b)

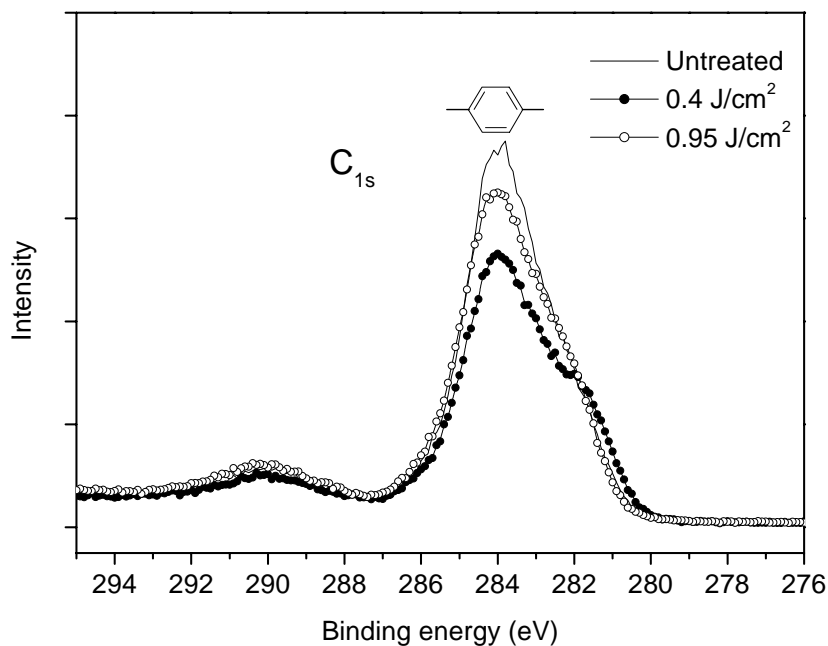
Fig. 25 Influence of the laser irradiation on chemical composition of the polymer surfaces. (a) The C/O ratio of as-received and laser treated PET and Thermanox films as a function of fluence, (b) fraction of different carbon species as a function of laser fluence [64].

4.1.4.2 XPS analysis of PC treated with laser

Fig. 26 shows the influences of laser fluence and pulse number on chemical modification of PC surfaces characterised by XPS. The C/O ratio decreases to a definite value with fluence first, then increases when the fluence is above 0.4 J/cm². However, no obvious difference is observed when laser pulses vary from 1 to 20. Generally, the C/O ratios of all laser ablated samples are slightly lower than that of untreated PC. This suggests an oxidation process during laser ablation. The normalized C1s XPS spectra (Fig. 26b) show that the intensity of peak assigned to benzene carbon decreases under 0.4 J/cm² and increases again under 0.95 J/cm² provided that the intensity of carboxylic carbon is relative stable. It means at low laser energy density, either the oxidation occurs or the benzene fragments are released from the PC due to the weak bonds between benzene and the neighbor carbon atoms.



(a)



(b)

Fig. 26 XPS analysis. (a) Chemical surface modification of the PC film treated under different laser fluence and pulse number; (b) normalized C1s spectra [65].

4.2 Time of flight mass spectrometry

4.2.1 ToF-MS of PET and Thermanox

The ToF-MS peaks of PET differ with laser fluence and irradiation duration, which are shown in Fig. 27 (a, b and c). Under low fluence the main species are at 28 and 44 amu corresponding to CO and CO₂. It is also possible that they contain CH₂=CH₂ (28) and CH₃COH (44). With higher fluence the main peaks of 120 and 170 amu appear. The peaks of 28, 44 and other small species are also found. After about 900 pulses, peaks for CO and CO₂ disappeared and the polymer is carbonised. XPS analysis has confirmed this phenomenon. As the results from laser ablation curves, Thermanox is easier ablated. Apart from the species

from PET, more peaks are found (Fig. 27d). The assigned structures of the emitted species from PET and Thermanox are listed in Table 5.

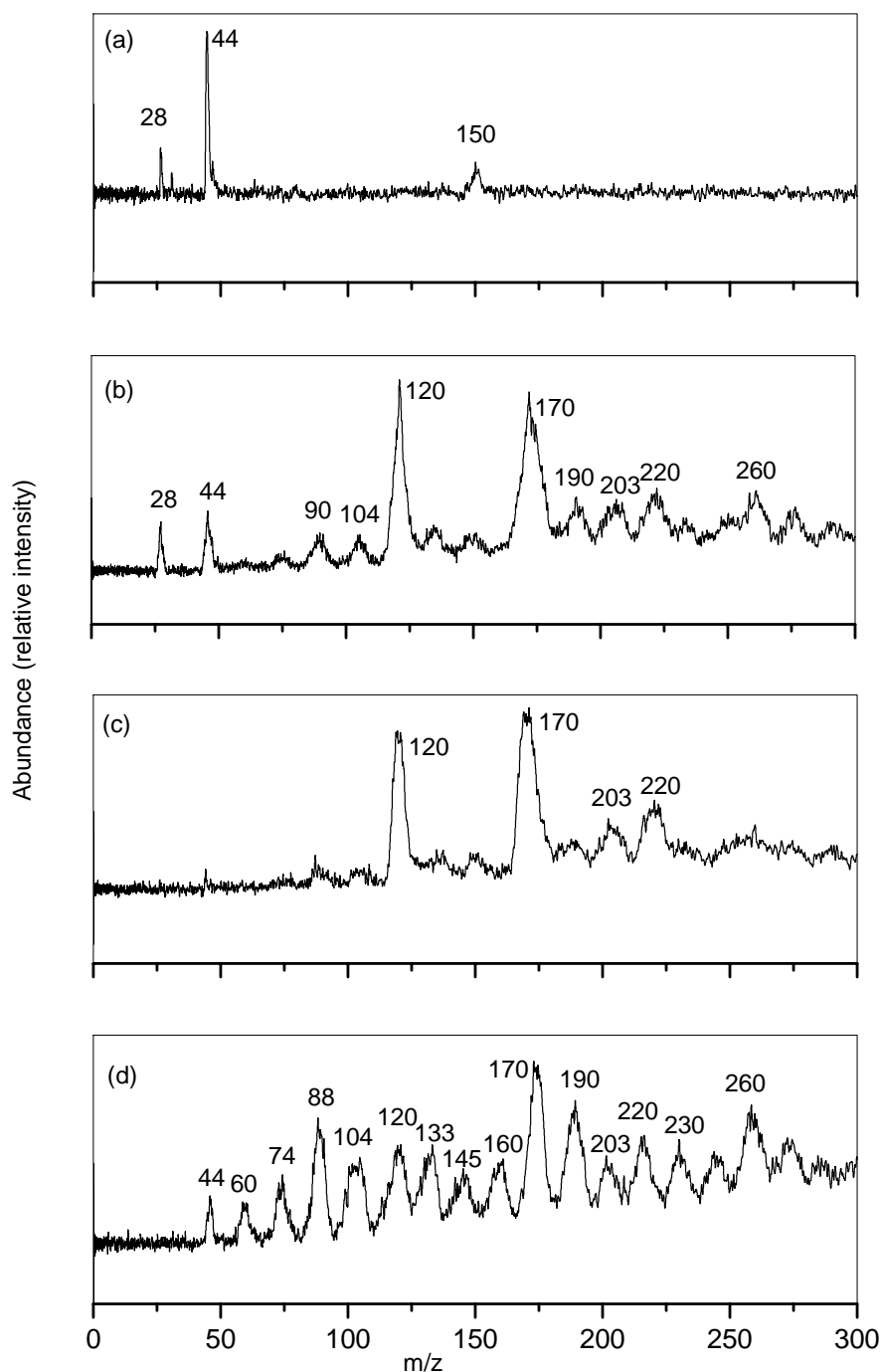


Fig. 27 ToF-MS Spectra of PET and Thermanox. (a) PET at 136 mJ/cm²; (b) PET at 183 mJ/cm²; (c) PET after 900 pulses at 183 mJ/cm² and (d) TXL at 212 mJ/cm².

Table 5 Assigned structures of species of PET and Thermanox found from ToF-MS spectra

m/z	Possible structure
28	CO (CH ₂ CH ₂)
44	CO ₂
60	O-CH ₂ -CH ₂ -O
74	C ₆ H ₂
89	HO-CH ₂ -CH ₂ -O-CO
104	C ₈ H ₈
120	O-C ₆ H ₄ -C ₂ H ₄
133	H ₄ C ₂ -C ₆ H ₄ -C ₂ H ₂
145	OOC-C ₆ H ₄ -C ₂ H ₃
170	C ₆ H ₅ -O-C ₆ H ₅
190	OOC-C ₆ H ₄ -COOCHCH
203	?
220	H ₂ CH ₂ OOC-C ₆ H ₄ -COOCH ₂ CH ₂
230	?
260	C ₆ H ₄ -O-C ₆ H ₄ O-C ₆ H ₄

4.2.2 ToF-MS of PC

The ToF-MS spectra of PC under different laser fluence and time duration are shown in Fig. 28. Similar to results of PET, CO and CO₂ were detected at low laser fluence, which were reported elsewhere with different lasers in different atmosphere. The m/z 150 is assigned to t-butyl phenol which was used to end-cap the molecule end of PC. Several small peaks are found near 67 amu that are assigned to species of ring opening of benzene, which were produced during laser ablation or ionisation. At higher fluence much more species were detected showing that laser ablation of this material is a very complex procedure. After about

900 pulses, most peaks disappeared showing that the polycarbonate was carbonised and the ablation rate is much lower. The possible structures of the peaks are listed in Table 6.

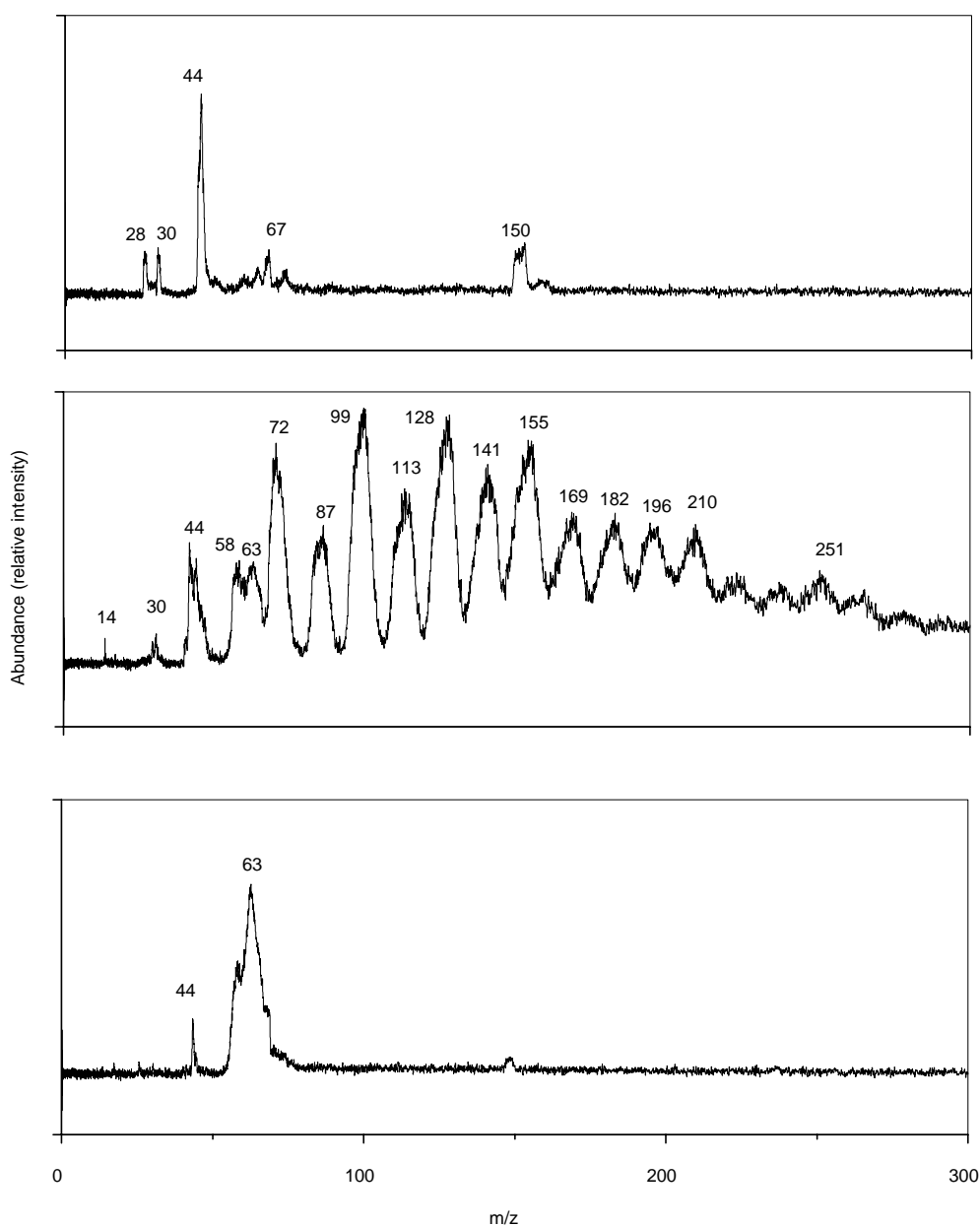


Fig. 28 ToF-MS spectra of PC. (a) 257 mJ/cm^2 , (b) 488 mJ/cm^2 , (c) 488 mJ/cm^2 after 900 pulses.

Table 6 Assigned structures found from ToF-MS spectra

m/z	Structure
14	CH ₂
28	CO
30	CH ₃ CH ₃
44	CO ₂
58	?
63	C ₅ H ₃
67	C ₅ H ₇
72	C ₆ H ₂
87	C ₇ H ₃
99	C ₈ H ₇
113	C ₉ H ₅
128	C ₁₀ H ₈
141	C ₉ H ₅ O
150	C ₁₂ H ₇
155	C ₁₁ H ₈
169	C ₁₂ H ₉ O
183	C ₆ H ₅ -O-C ₆ H ₄ -CH ₂
196	H ₃ C-C ₆ H ₄ -O-C ₆ H ₄ -CH ₂
210	H ₃ C-C ₆ H ₄ -O-C ₆ H ₄ C ₂ H ₃
251	HC-C ₆ H ₄ -OCO ₂ -C ₆ H ₄ -C ₂ H ₂

4.3 Laser ablation of thin polymer solution

The UV spectra of THF and PC solution are shown in Fig. 29. Since the result is not exact when the absorbance is higher than 2, the absorbance of 7.38 for 1% (w/w) PC solution is calculated by linear dependence of the absorbance on PC concentration (Fig. 30). According to Eq. 2-6 ($l = 0.2$ cm is the thickness of the quartz cuvette), the absorption coefficient of 1 %

PC (w/w) solution was calculated to 85 cm^{-1} ; while that of THF is only 2.5 cm^{-1} , which is relatively small and can be neglected.

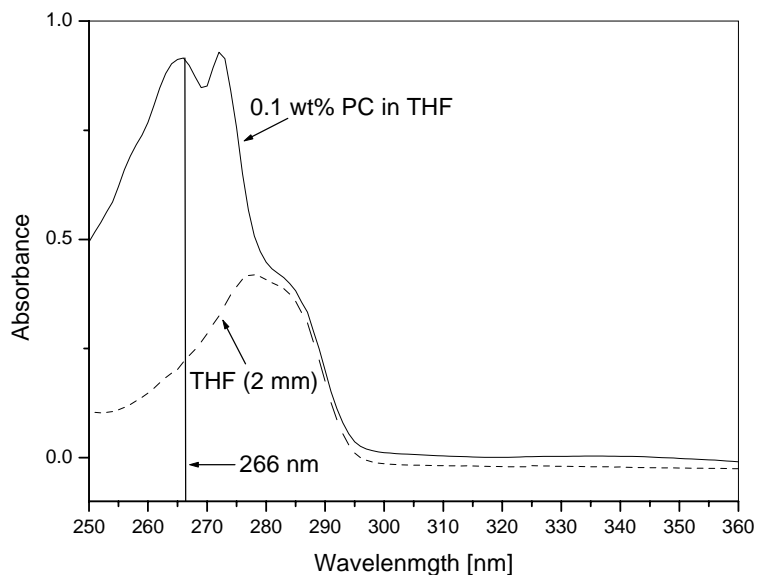


Fig. 29. UV spectra of THF and PC solution measured in a 2 mm quartz cuvette

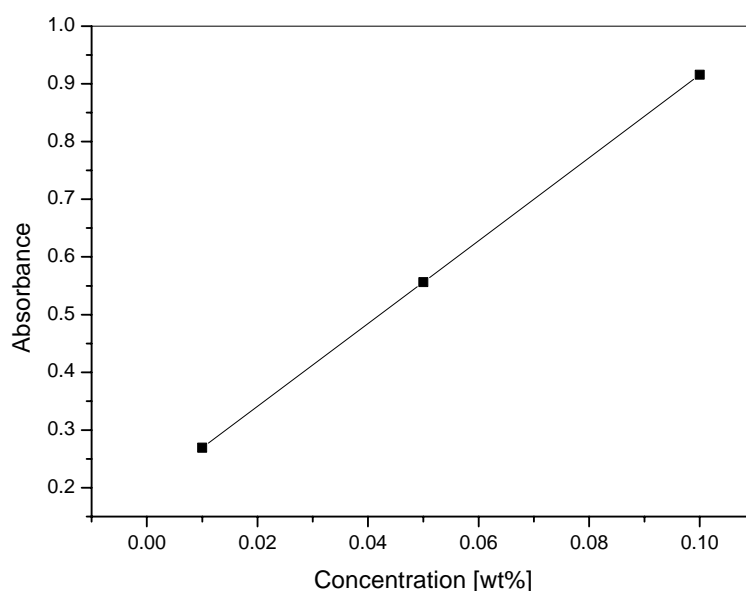


Fig. 30. Dependence of the absorbance on PC concentration at 266 nm. According to linear fitting, the absorbance of 1% (w/w) solution is 7.38.

The decrease of the average number molecular weight (M_n) after 10 and 100 pulses irradiation under different fluence is shown in Fig. 31. Significant degradation has already been found under low fluence irradiation. After 100 pulses M_n decreases 17% under 25 mJ/cm², and more than 40% under 195 mJ/cm².

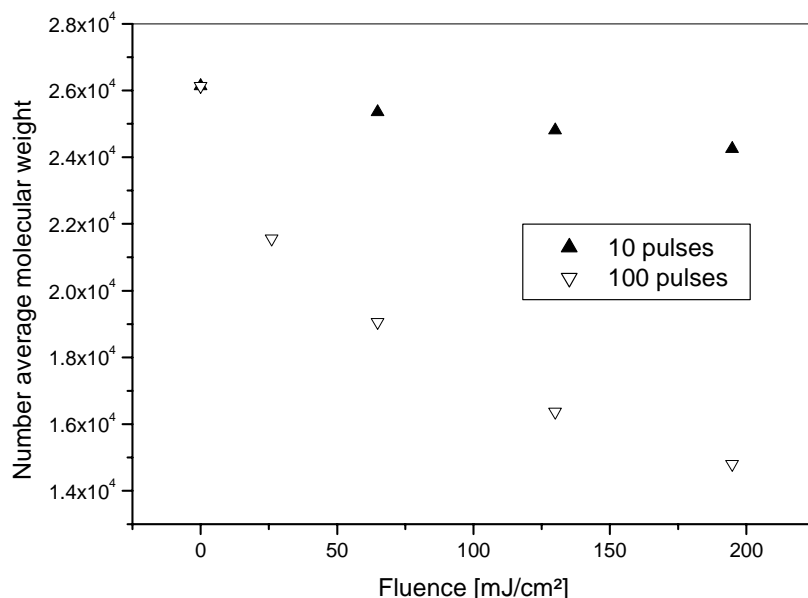


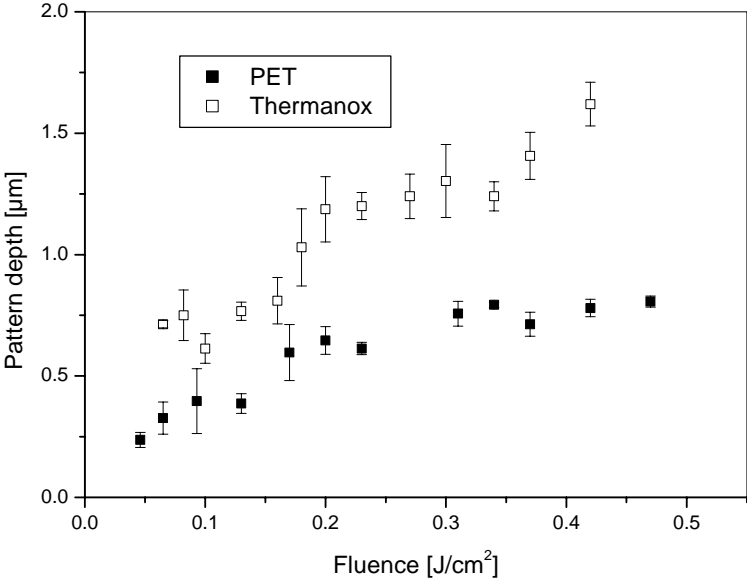
Fig. 31 Decrease of the number average molecular weight of PC after laser irradiation

4.4 Micropatterning of polymer surface by laser interference lithography

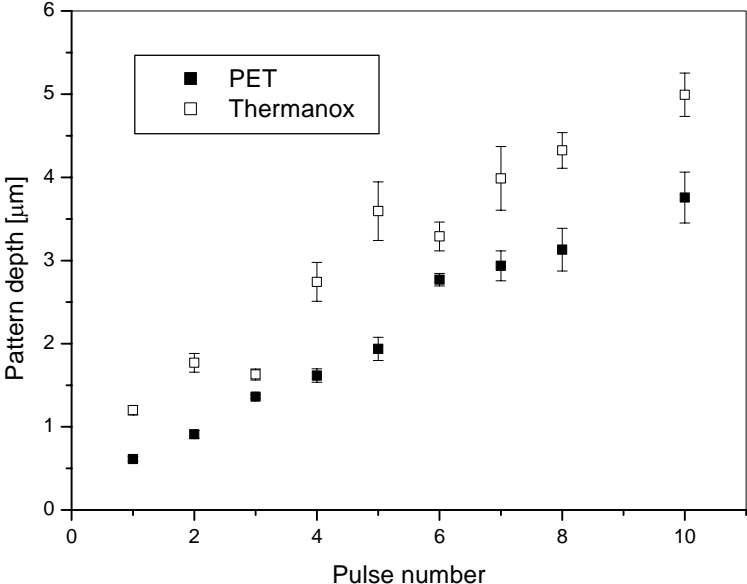
4.4.1 Micropatterning of poly(ethylene terephthalate) and Thermanox

As indicated in Eq. 2-30, the period (spacing) is determined by the laser wavelength and angle between two interfering beams. Adjusting the angle, the period can be varied from several hundred nanometers up to 20 μm . For a definite polymer, the depth of the micropattern depends on the fluence and laser pulses, which are shown in Fig. 32a. Micropatterns can be observed on PET and Thermanox when the fluence exceeds 0.05 J/cm². The depth was

measured in three different positions within an area whose diameter is the half of the whole structured area.



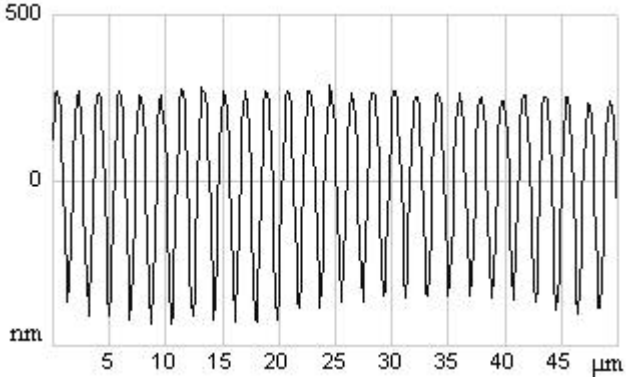
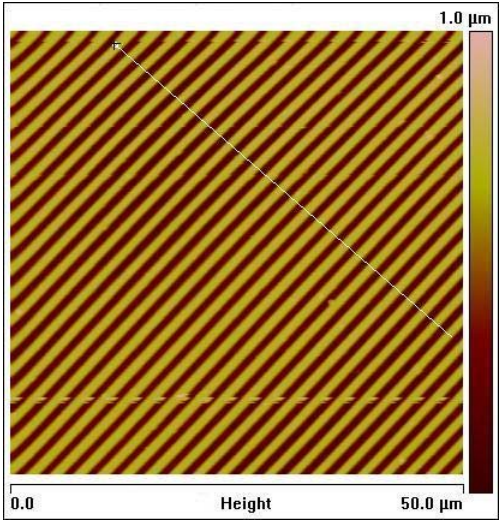
(a)



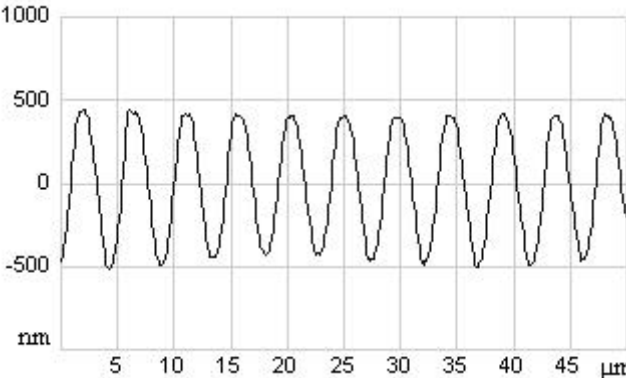
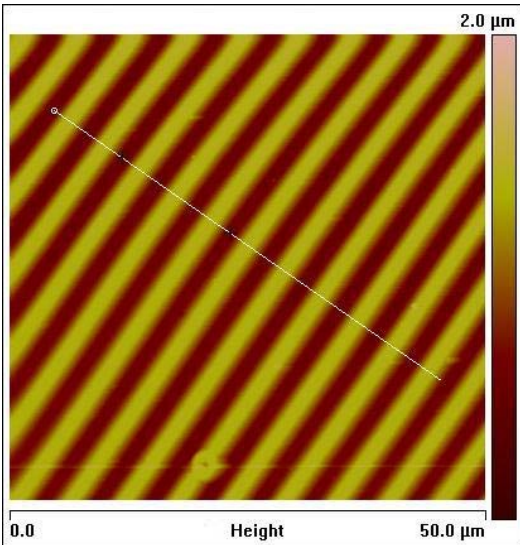
(b)

Fig. 32 Dependence of the depth of micropatterns ($P = 5 \mu\text{m}$) on the fluence and number of the laser pulses [64].

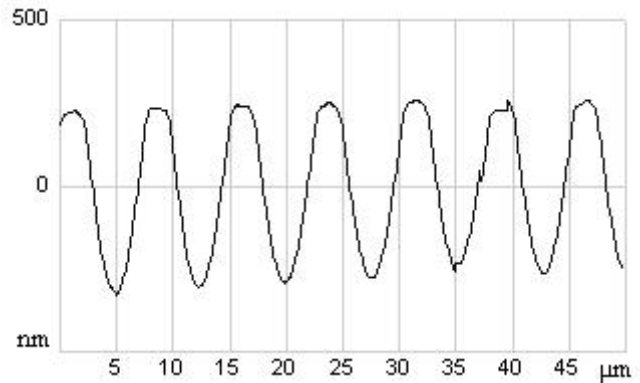
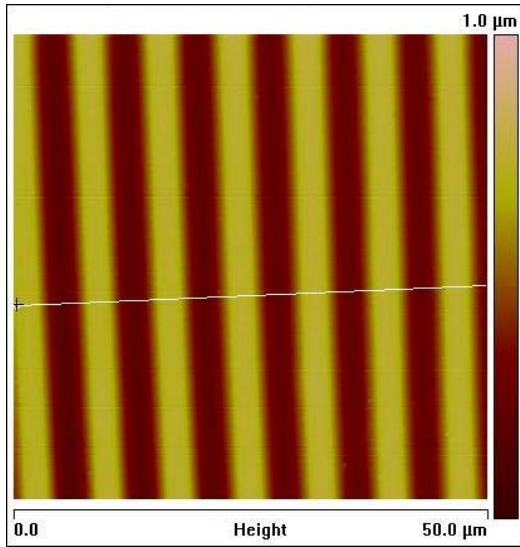
The depth of the micropatterns on both polymers increases linearly with the laser fluence until about 0.2 J/cm². Above this value, the depth on PET remains nearly stable, while increases on TXL but at a relative low rate. The influence of the pulse number is given by Fig. 32b by which a linear increase with pulse number in both materials is observed up to 10 pulses. With 10 laser pulses, the depth of 5 μm is reached on TXL and 4 μm on PET.



(a)



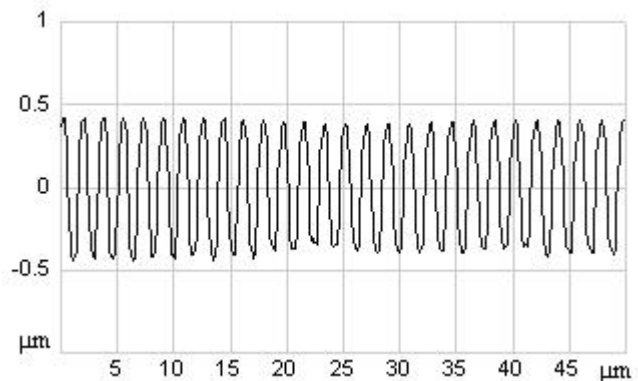
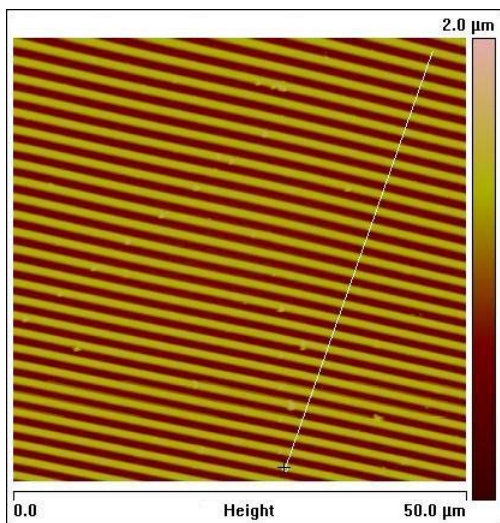
(b)



(c)

Fig. 33 AFM micrographs of linear micropatterns on PET film with a period of (a) $2\mu\text{m}$, (b) $5\mu\text{m}$ and (c) $8\mu\text{m}$ induced by 1 pulse.

As for the two types of polymers, very consistent micropatterns were prepared whose AFM micrographs are shown in Fig. 33 for PET and Fig. 34 for TXL. Nevertheless, their cross section is different. The cross section of PET patterns is identical to the reverse of the energy distribution on interference pattern while that on Thermanox is steeper and narrower, especially when the period is larger than $2\mu\text{m}$ (Fig. 34b).



(a)

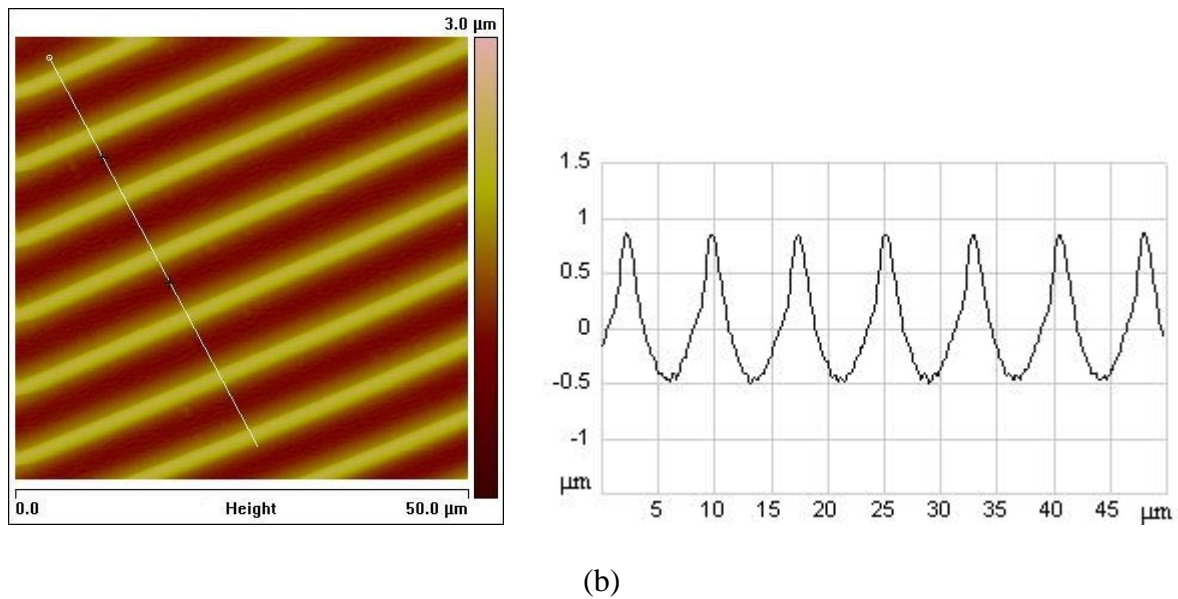


Fig. 34 AFM micrographs of linear micropatterns on Thermanox film with a period of (a) 2 μm , (b) 8 μm .

The pictures of point-like patterns taken by using WLI are shown in Fig. 35. After second

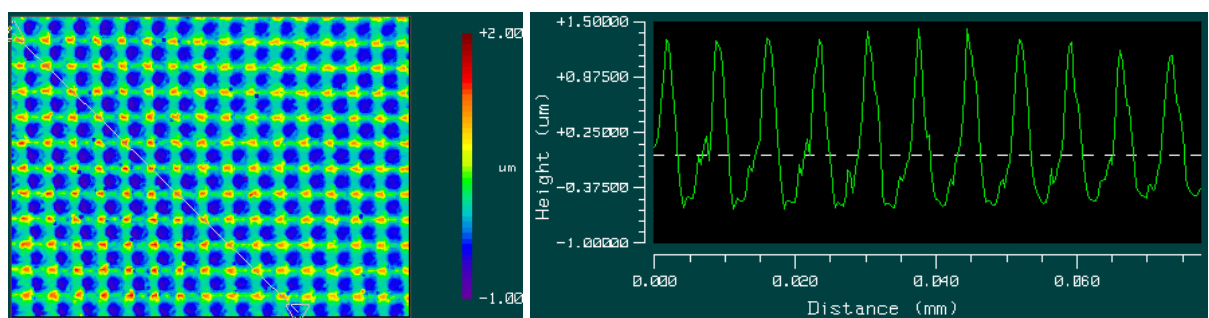
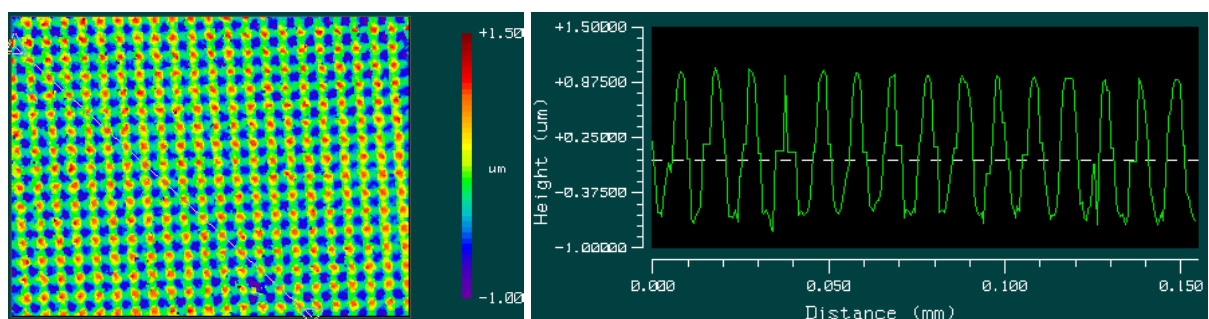
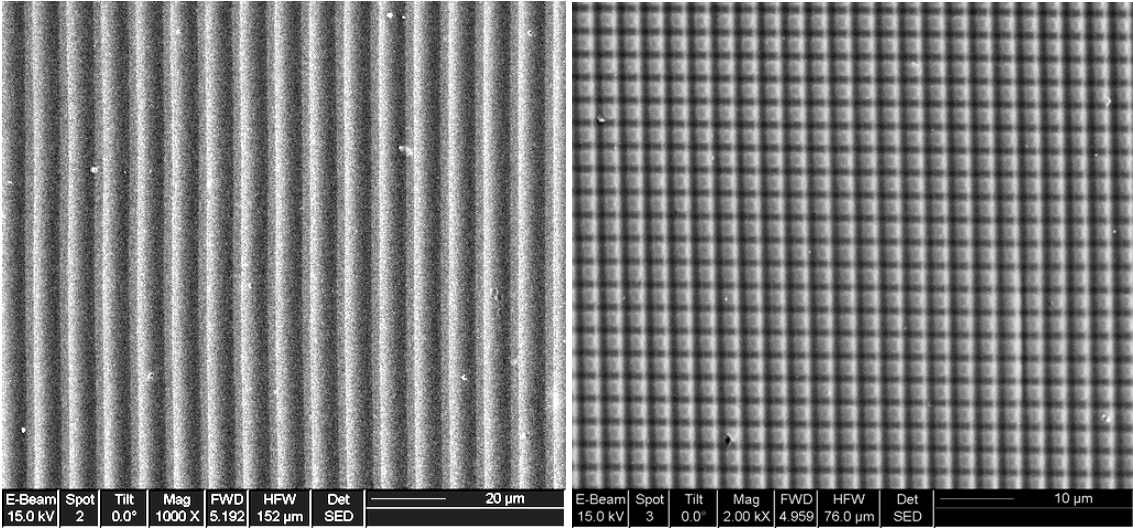


Fig. 35 WLI photographs of point micropatterns. (a) PET pattern with a period of 7 μm and depth of 1.3 μm , (b) TXL pattern with a period of 5 μm and depth of 1.8 μm .

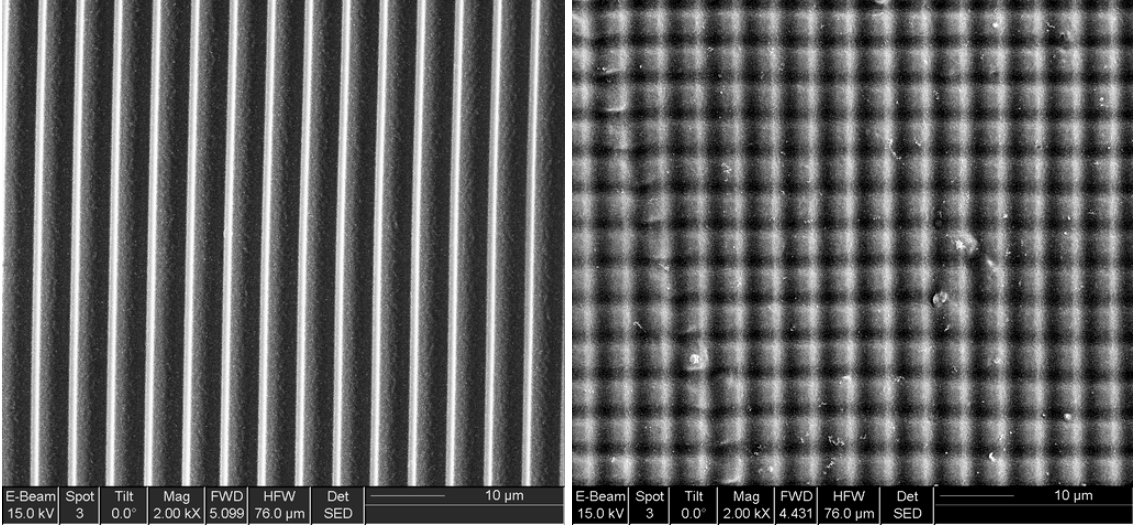
laser ablation, the pattern depth is larger. The laser fluence for second ablation should be carefully selected in order to avoid destroying the patterns when the period is smaller than 2 μm .

SEM micrographs of linear and point patterns are shown in Fig. 36 which demonstrates the very consistent patterns.



(a)

(b)



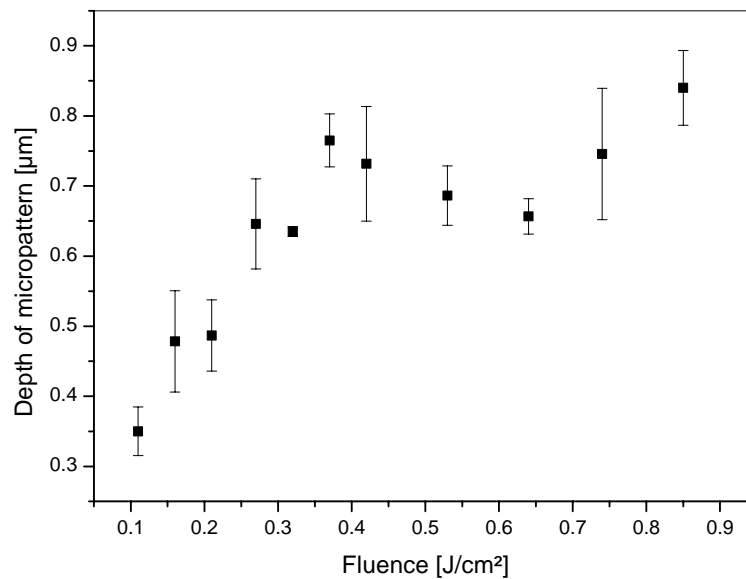
(c)

(d)

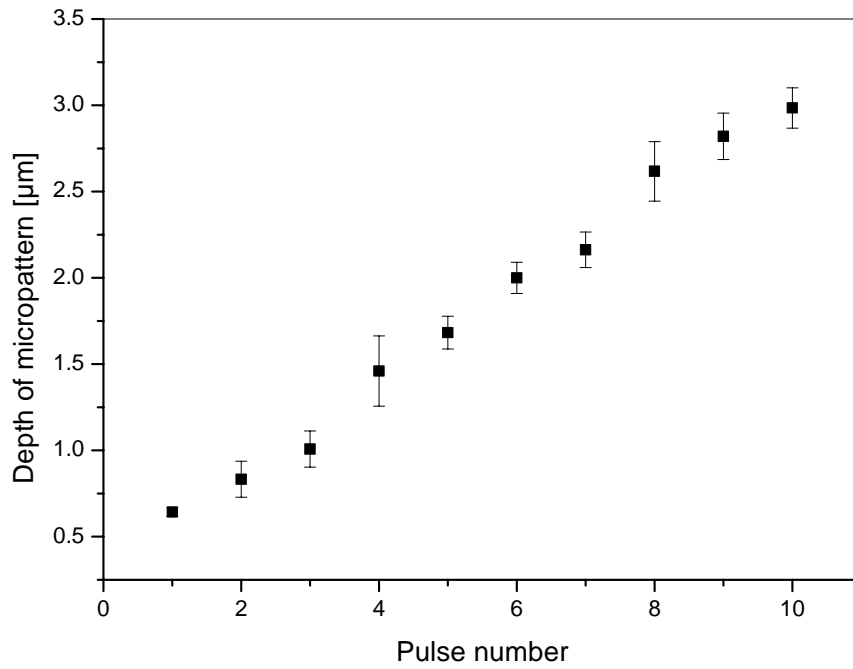
Fig. 36 SEM photographs of (a) PET with a period of 9 μm , (b) PET with a period of 3 μm , (c) TXL with a period of 5 μm , and (d) TXL with a period of 5 μm .

4.4.2 Micropatterning of polycarbonate

Fig. 37 shows the influence of the laser fluence and pulse number on the depth of linear patterns on PC film. The depth of the linear patterns increases with the fluence linearly up to a saturation value at about 0.4 J/cm². In order to get a homogeneous pattern, micropatterning should be performed above this fluence, but the depth can't be higher than 0.85 μm when ablated by one laser pulse. A deeper micropattern is produced by several shots as shown in Fig. 37b in which a linear pulse number dependence is observed until 10 laser pulses. With increase of the pulse number, the ridges of the pattern become narrower. Compared with line patterns, the depth (vertical distance between highest und deepest positions) of the point patterns is about 40% higher because of the second ablation at the deepest positions. The aspect ratio for line PC patterns has reached only 0.3-0.4 with one laser pulse depending on the laser fluence and pattern period, yet 0.8-1.0 has been reached with number of laser pulses. Accordingly, the aspect ratio of point patterns is larger.



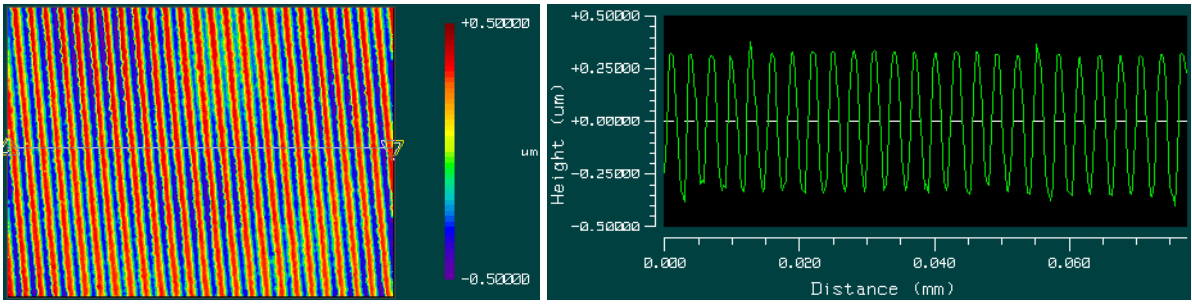
(a)



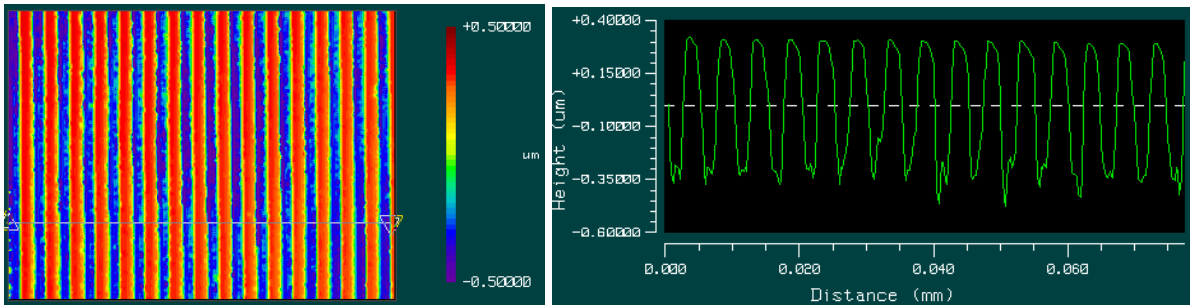
(b)

Fig. 37 Dependence of the depth of linear micropatterns (period: 5 μm) on (a) laser fluence, and (b) pulse number (under the same fluence: 0.32 J/cm²) [65].

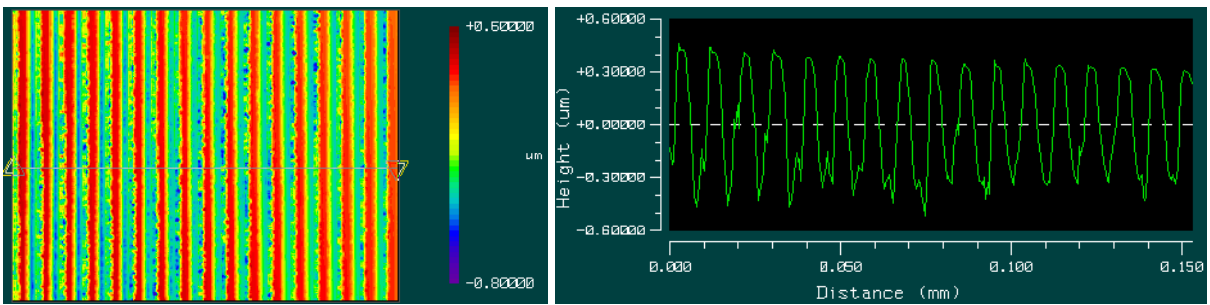
Fig. 38 shows the linear patterns with different periods induced by different pulse number on PC. As discussed above, one laser pulse can only induce a relatively small pattern depth, while a depth of 2.8 μm was obtained with 8 pulses although the fluence is only 0.32 J/cm². The cross section of the linear patterns is similar to that of the interference pattern, and all of them are well-defined and of great consistency in a large area. A point pattern on PC is shown in Fig. 39.



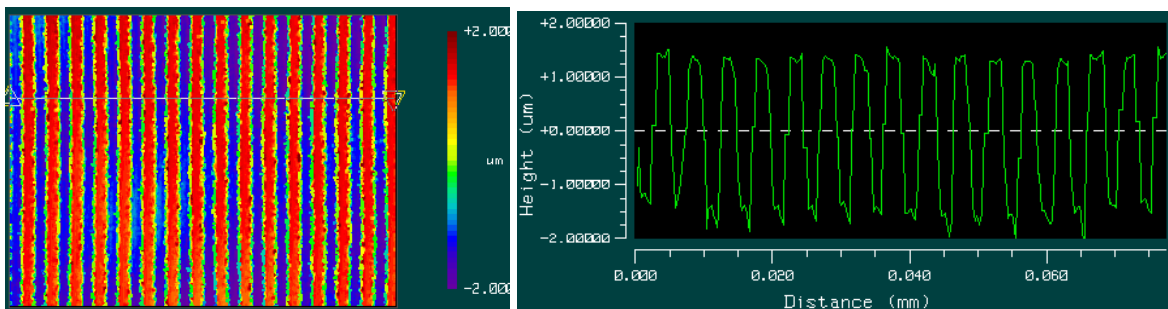
(a)



(b)



(c)



(d)

Fig. 38 WLI photographs of linear patterns on PC produced with (a) 1 pulse: 0.37 J/cm^2 (period: $3 \text{ }\mu\text{m}$, depth: $0.6 \text{ }\mu\text{m}$); (b) 1 pulse: 0.37 J/cm^2 (period: $5 \text{ }\mu\text{m}$, depth: $0.6 \text{ }\mu\text{m}$); (c) 1 pulse: 0.37 J/cm^2 (period $9 \text{ }\mu\text{m}$ depth: $0.7 \text{ }\mu\text{m}$); (d) 8 pulse: 0.32 J/cm^2 (period: $5 \text{ }\mu\text{m}$, depth: $2.8 \text{ }\mu\text{m}$).

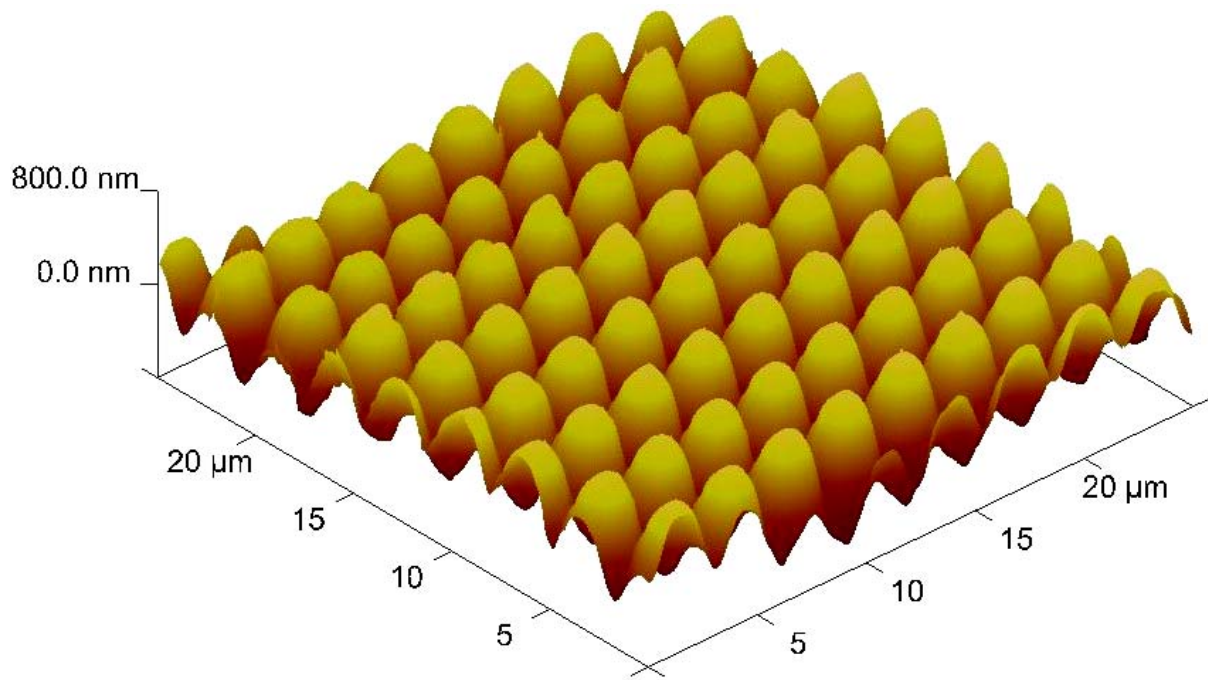


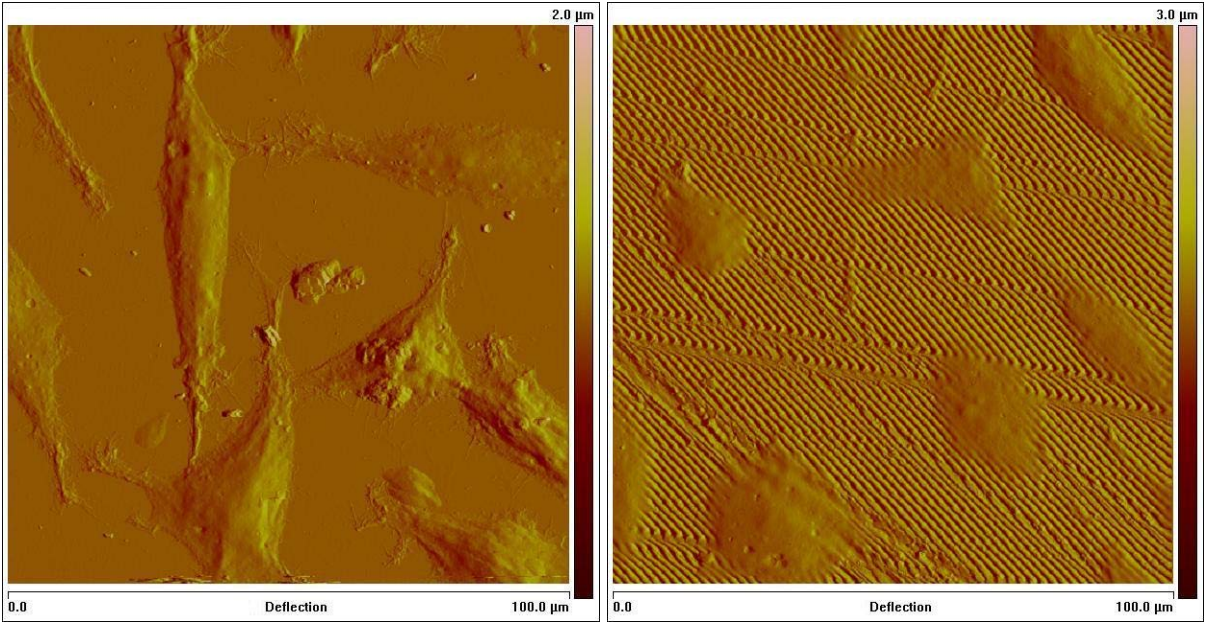
Fig. 39 AFM photograph of point pattern induced with laser fluence of $0.37 \times 0.37 \text{ J/cm}^2$ on PC (period: $3 \mu\text{m}$, depth: $0.9 \mu\text{m}$).

4.5 Cell culturing on micropatterned polymer surface

4.5.1 Mouse fibroblasts cultured on micropatterned Thermanox

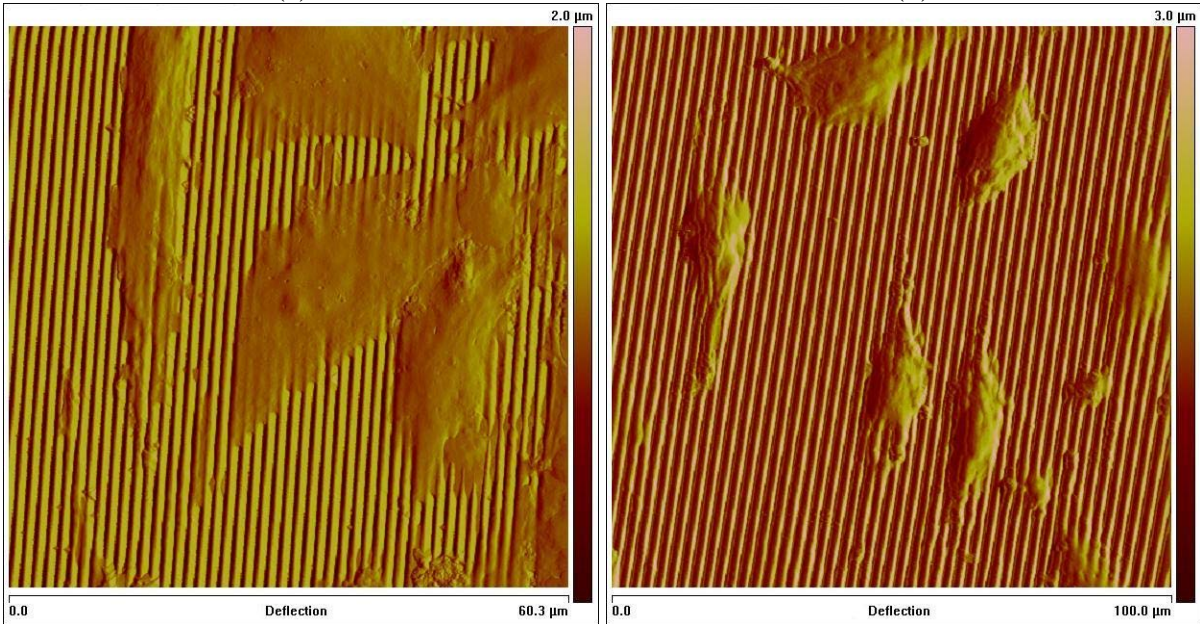
Fig. 40 shows the AFM images of mouse fibroblasts (L929) cultured on linear TXL and TXB patterns. L929 on unpatterned surface possess different forms, some are though elongated but without orientation (Fig. 40a). Fig. 40b and c show that L929 grown on the micropatterns with small period ($1.26 \mu\text{m}$) orientated themselves along the lines, but they were only slightly elongated. They seems only lying on the hill of the ridges without contact with the valley. With increase of the periods to 2 and $5 \mu\text{m}$, the cells orientated themselves highly aligning the microgrooves, and also they were better elongated and had spindle-like shape (Fig. 40d, e, f, and g). On $5 \mu\text{m}$ patterns, they bended themselves to form focal contact with the valley. In contrast, L929 grown on wider microgrooves ($9.7 \mu\text{m}$, Fig. 40h) still orientated themselves parallel to the microgrooves but the effect was not as strong as L929 seeded on smaller

microgrooves. In addition, the cells were less spindle-shaped but rather triangular. Additionally, most of the lamellopodia of the fibroblasts on wider microgrooves with period of 5 μm and 9.7 μm appeared to be extended not only parallel to the microgrooves but also horizontally crossing the patterns while most of the lamellopodia of the fibroblasts extended only in the direction of the micropatterns. No different effect between TXL and TXB are observed.



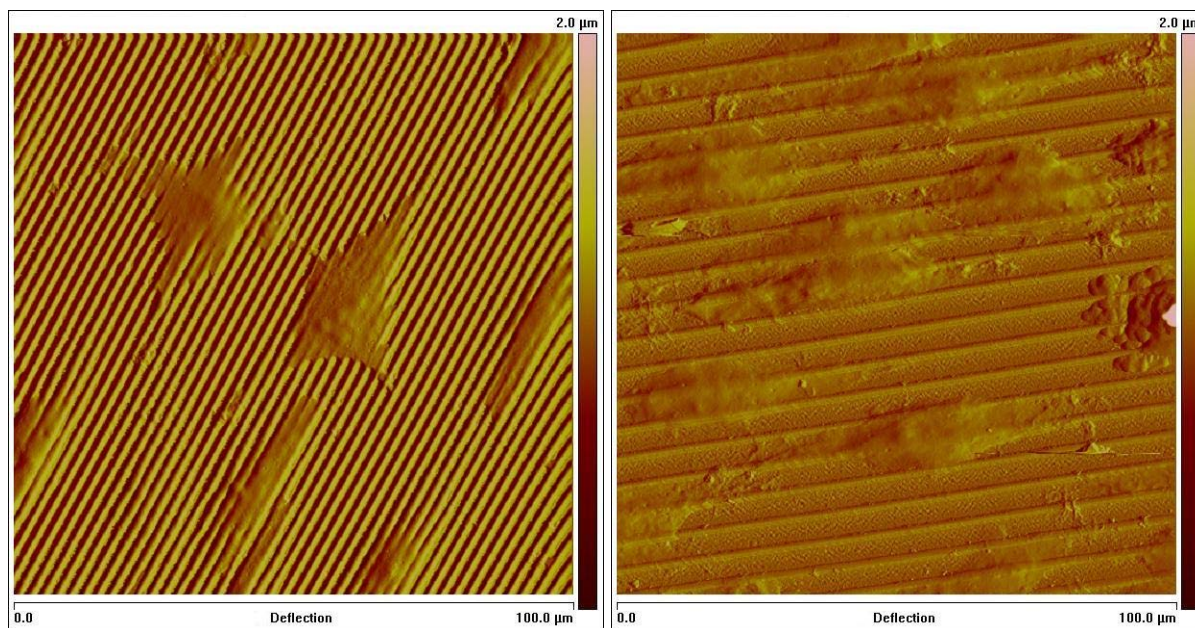
(a)

(b)



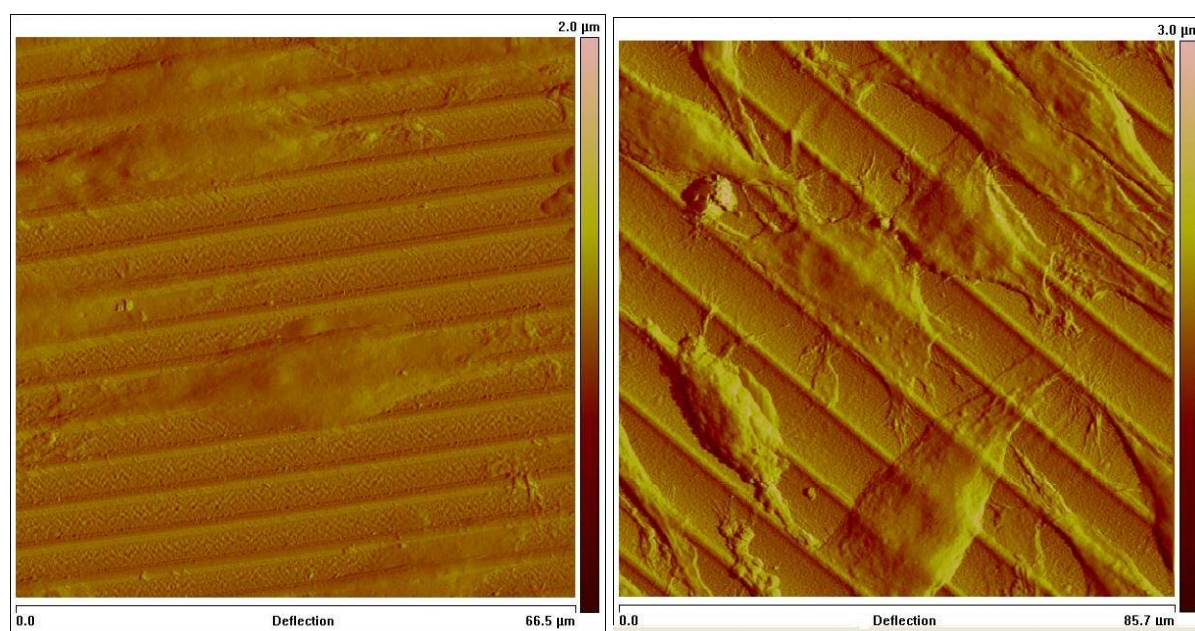
(c)

(d)



(e)

(f)



(g)

(h)

Fig. 40 Mouse fibroblasts cultured on Thermanox micropatterned by LIL. (a) TXL, unpatterned; (b) TXL with period of 1.3 μm ; (c) TXB with period of 1.3 μm ; (d) TXL with period of 2.1 μm ; (e) TXB with period of 2.1 μm ; (f) TXL with period of 5.1 μm ; (g) TXB with period of 5.1 μm ; (h) TXL with period of 9.7 μm .

4.5.2 Human pulmonary fibroblasts cultured on patterned PET and TXL

Light microphotographs show that human pulmonary fibroblasts (HPF) cultured on both collagen coated and non-coated laser-micropatterned PET and TXL surfaces are elongated, spindle-like shaped, and no morphological difference among the cells cultured on all micropatterned polymer samples are observed (Fig. 41a, b, and c). In addition and most importantly, HPFs show directional growth parallel to the line patterns with all different groove widths. In contrast, HPFs cultured on collagen-coated and non-coated unmodified PET and Thermanox film are larger, multipolar, rather randomly orientated, and frequently overlap each other (Fig. 41 d). However, this phenomenon is seldom seen among the HPFs cultured on micropatterned surfaces.

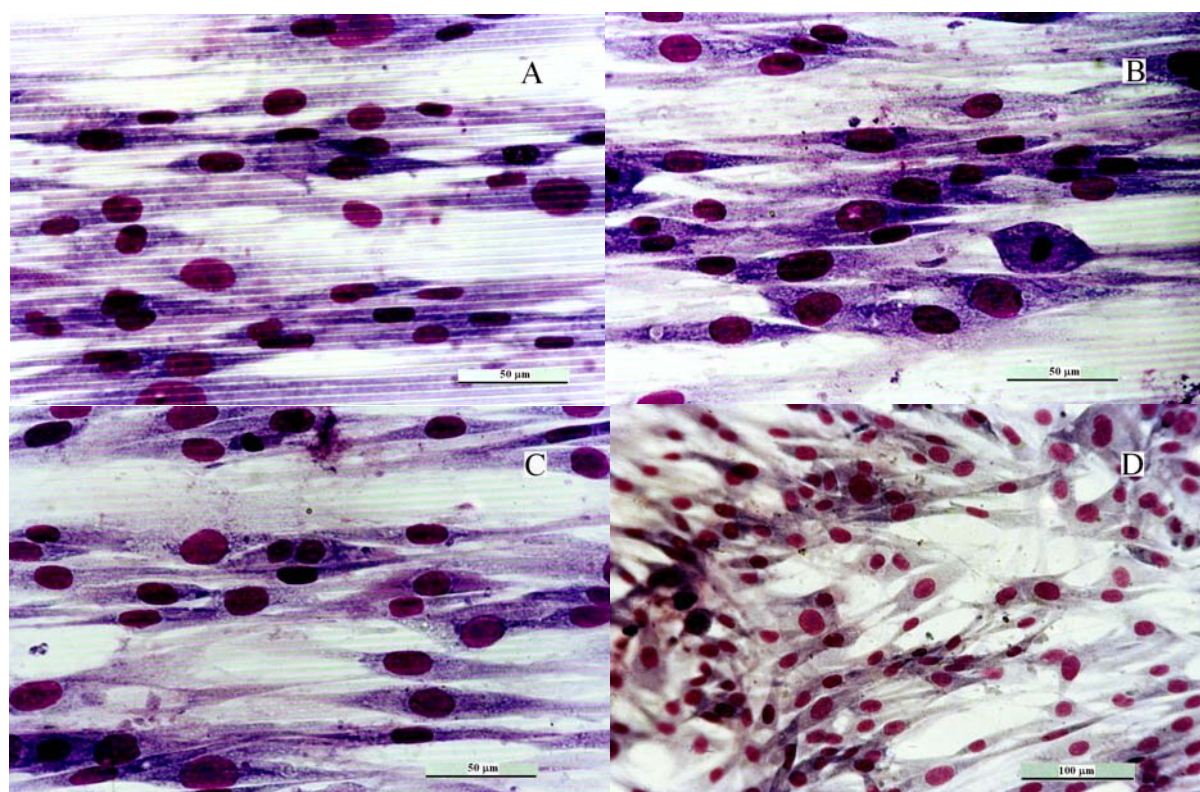


Fig. 41 Human pulmonary cells cultured on PET and Thermanox micropatterns prepared by LIL (a) TXL with a period of 4 μm , uncoated; (b) PET with a period of 4 μm , uncoated with collagen; (c) PET with a period of 4 μm , coated with collagen; and (d) original PET without pattern.

4.5.3 Human pulmonary fibroblast cultured on patterned PC

White light photographs show that HPFs cultured on both collagen-coated and non-coated line-patterned PC are strongly elongated and strictly orientated parallel to the line directions (Fig. 42). In contrast, HPFs cultured on collagen-coated and non-coated but unmodified PC film are mostly multipolar, also strongly elongated, but show no specific orientation, and frequently overlapping each other.

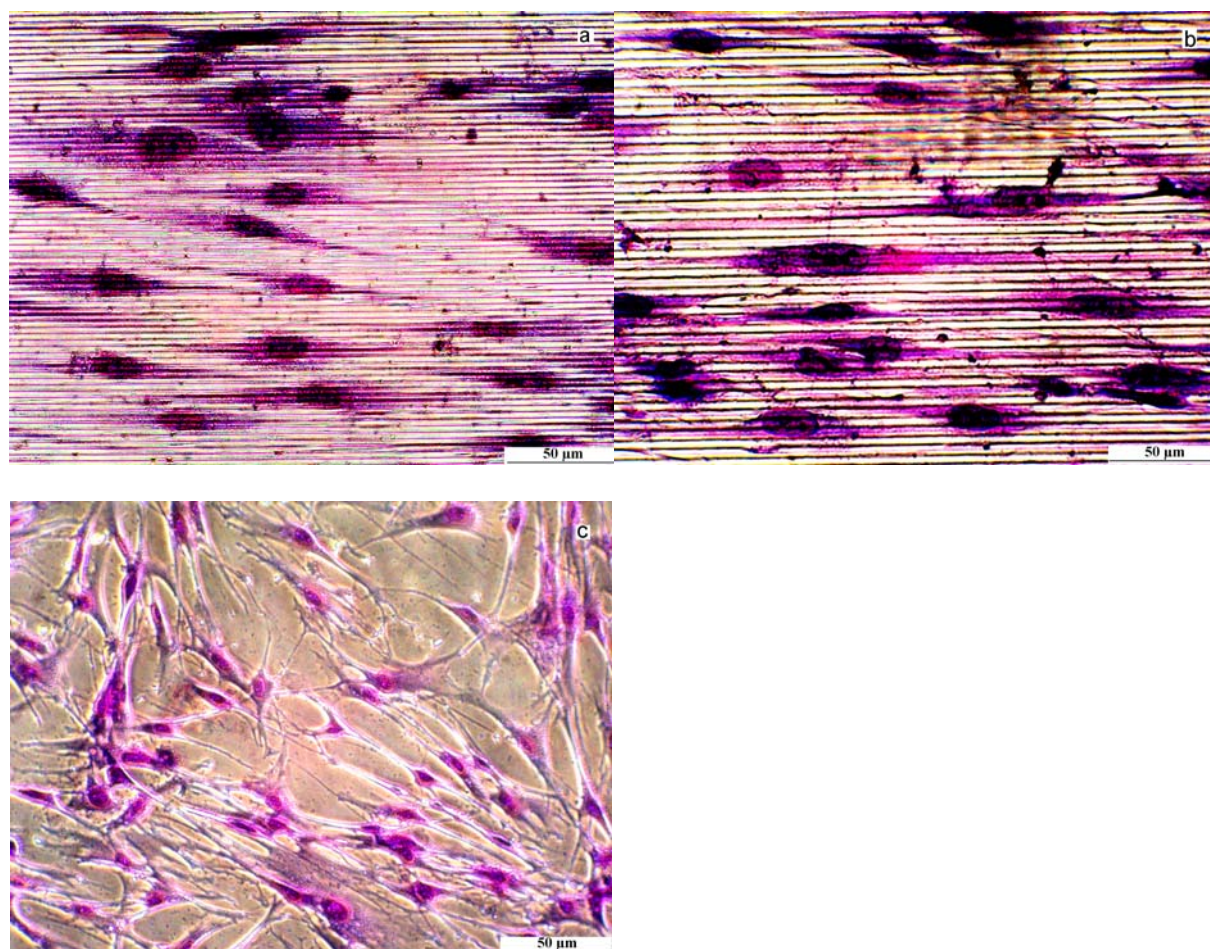


Fig. 42 Human pulmonary cells cultured on (a) line micropattern on PC film with a period of 3 μm prepared by LIL; (b) line micropattern on PC film with a period of 9 μm prepared by LIL, and (c) original PC film without pattern. All substrates were coated with collagen [65].

The number of cells grown on different patterns is shown in Fig. 43. Highest amount of HPFs are seen on the PC film without surface micropattern while the second highest amount of

HPFs are seen on line-patterned PC film with a period of 3 μm . In addition, the number of cells decreases as the period increases. However, there are more HPF grown on line-patterned PC film with a period of 9 μm than on the line-patterned PC film with a period of 5 μm and 7 μm . Considering the experimental error, it can be concluded that the period of the line micropatterns on the surface of PC films produced by LIL has influence on the cell number, but the effect is relatively weak.

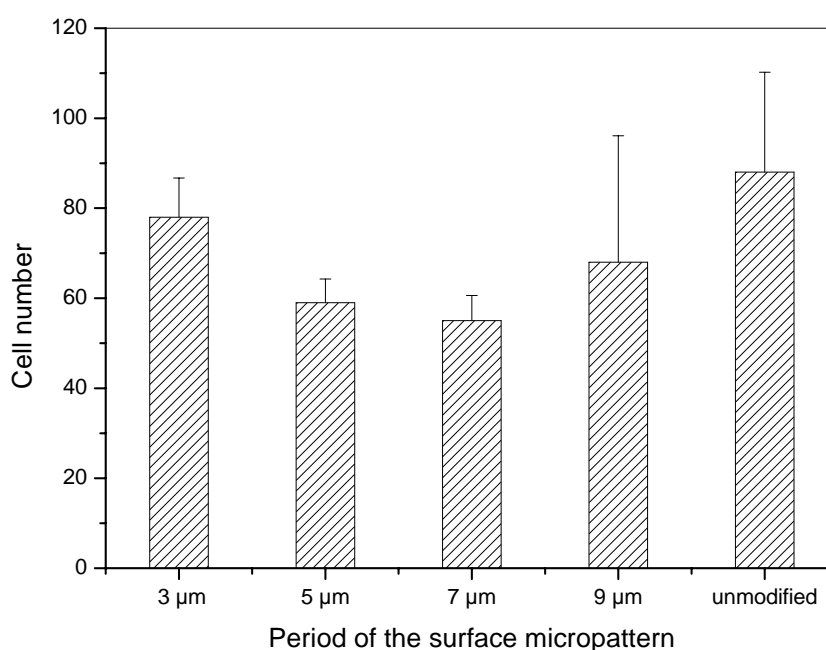


Fig. 43 Amount of HPFs grown on line-patterned PC with different periods [65].

Furthermore, the size of the cell body varies only slightly when seeded on PC films with different period of the line patterns. The so-called “latitude” lengths of the HPFs seeded on the PC bearing line pattern with period of 3 μm are the second longest followed the cells seeded on unmodified PC. However, the latitude lengths of the HPF seeded on PC bearing line patterns with other periods are rather similar. Likewise, the “longitude” lengths of the cells seeded on most of the PC with different periods of the line patterns are also closed to

each other (Fig. 44). Therefore, the effect of period of the line patterns to the cell length is relatively small.

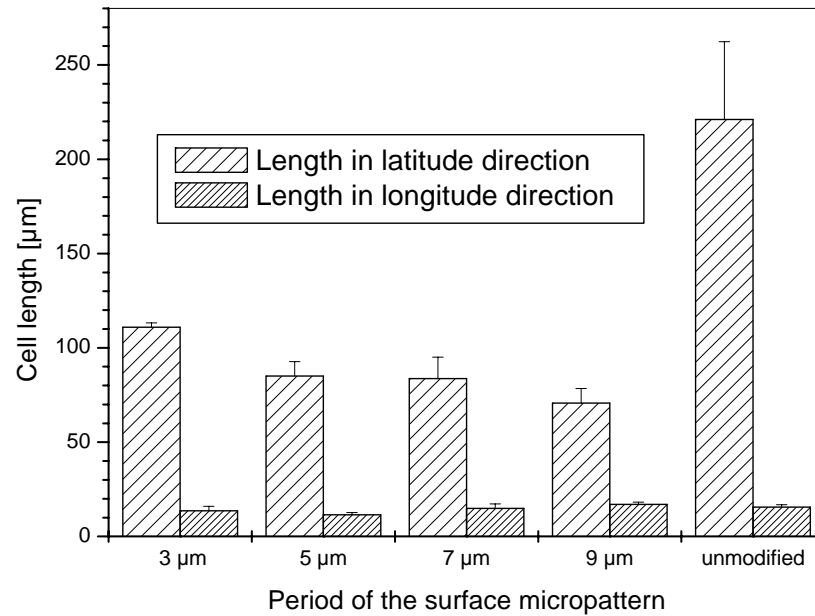
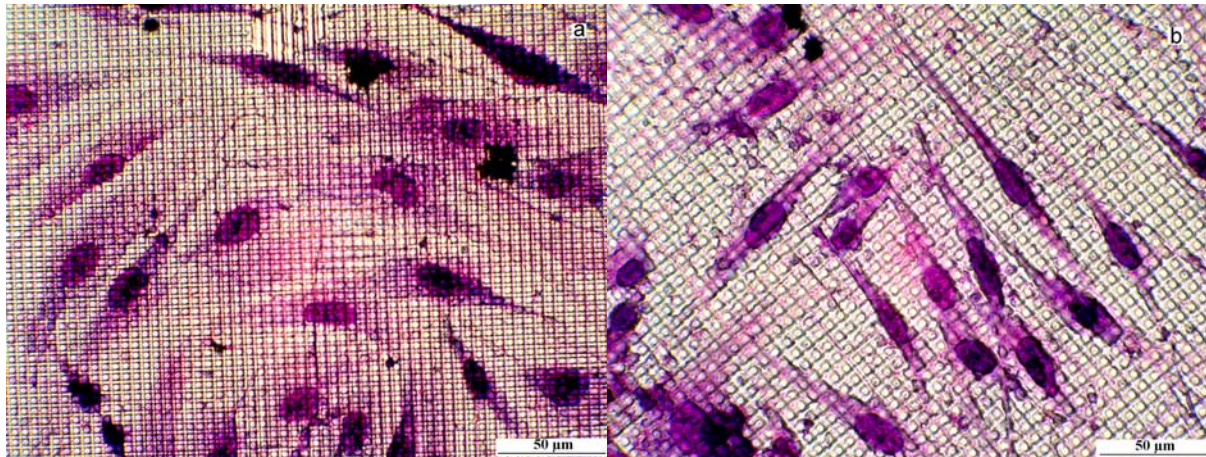


Fig. 44 Comparison of cell bodies in terms of latitude and longitude lengths to different periods of line patterns on the PC films [65].

In comparison to HPFs seeded on line patterns ablated on PC films, the cells seeded on point patterns don't show the sole orientation (Fig. 45). However, unlike the cells seeded on unmodified PC film, HPFs seeded on point patterns are mostly bipolar, spindle-like. Furthermore, they also show some orientation along the specific directions as shown in Fig. 46. On the pattern with larger period (7 μm), the cell orientation is more obvious and the elongation is larger than on the pattern with 5 μm period. In addition, cells are sometimes overlapping each other when seeded on point patterns but less frequently than the cells seeded on unmodified PC film.



(a)

(b)

Fig. 45 (a) HPFs seeded on point-patterned PC film with a period of 5 μm and b) HPF seeded on point-patterned PC film with a period of 7 μm . Both substrates were coated with collagen [65].

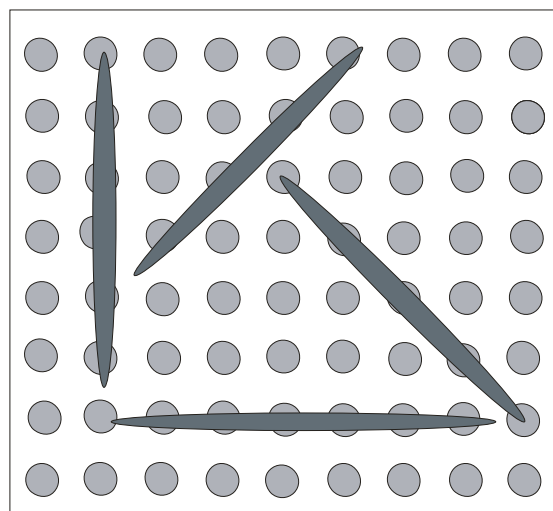


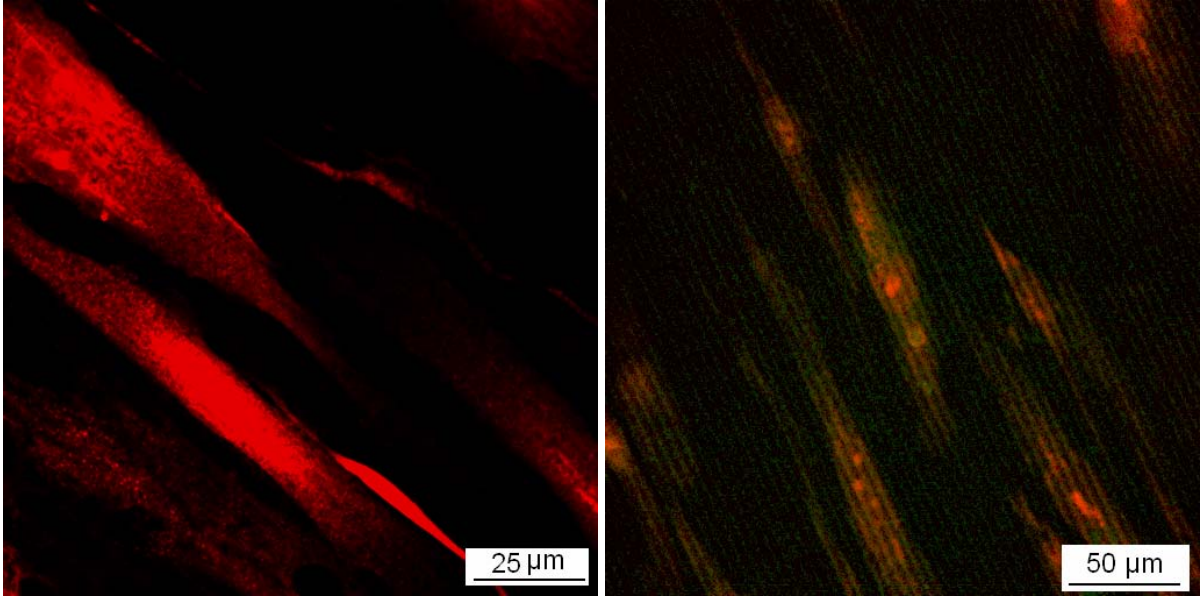
Fig. 46 Preferred orientation of the HPFs seeded on point micropatterns on PC surface prepared by LIL.

4.6 Inflammation of cells on cultured polymer surface

4.6.1 E-selectin expression

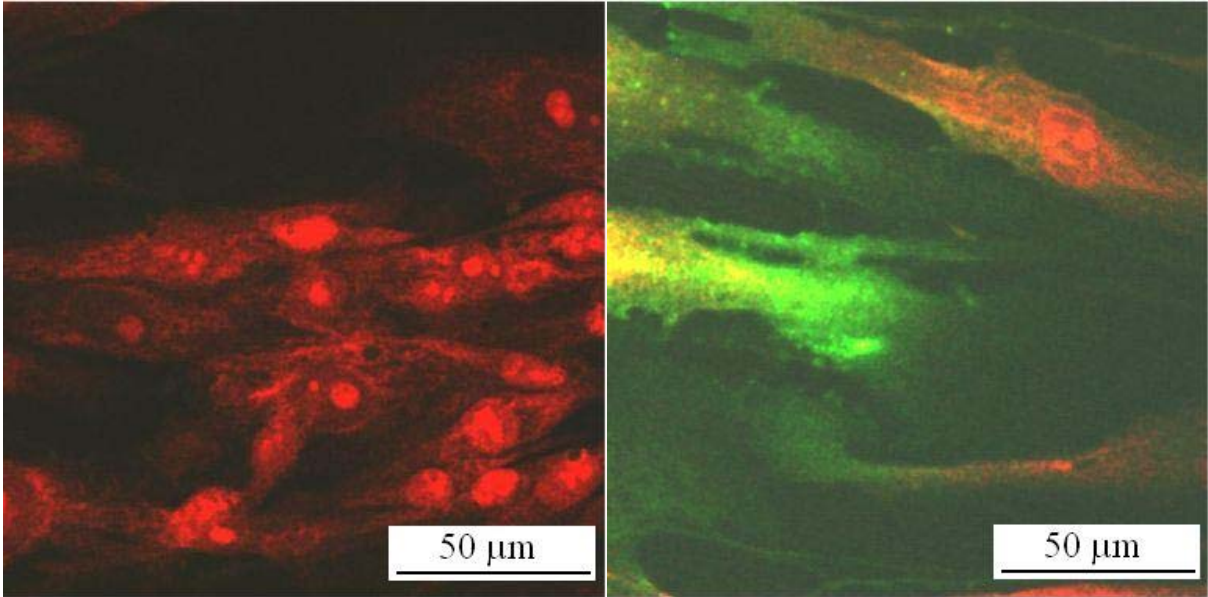
Confocal laser scanning microscopic (CLSM) photographs of HPFs cultured on patterned and original polymer surfaces and stained with antibodies against E-selectin are shown in Fig. 47.

Green fluorescence emitted by fluorescein isothiocyanate (FITC) on the surface of HPFs indicates that E-selectin is expressed when the cells are seeded on linear PC pattern (Fig. 47b). In contrast, no green fluorescence is observed when the cells are seeded on the unmodified PC film (Fig. 47a).



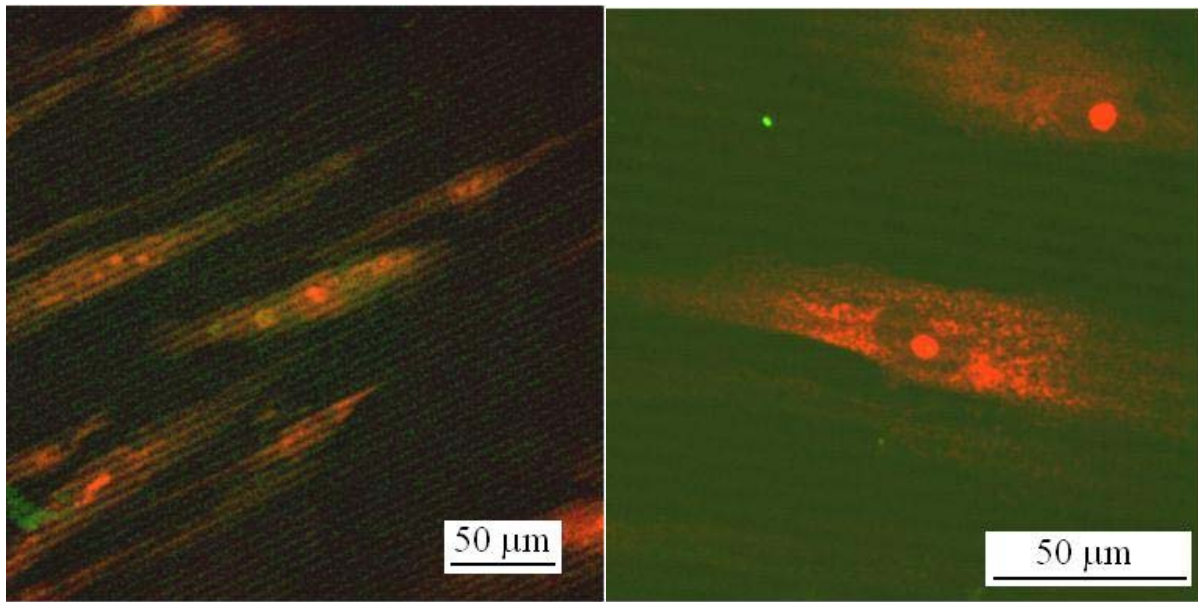
(a)

(b)



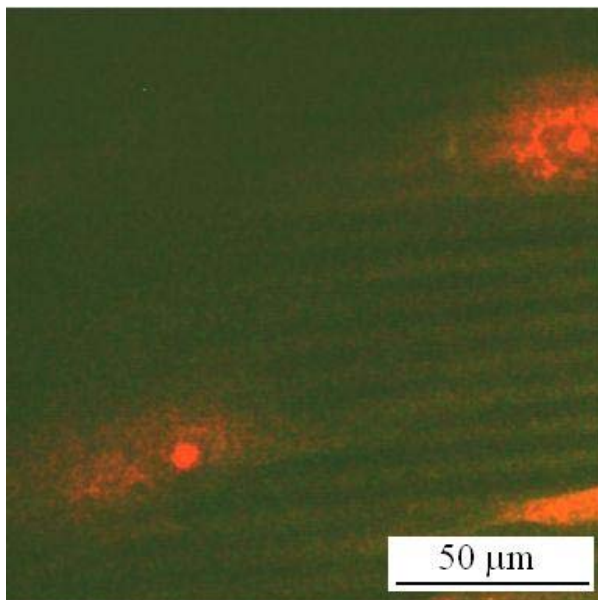
(c)

(d)



(e)

(f)



(g)

Fig. 47 Laser confocal microscopic images of HPFs seeded on PC and TXL with linear patterns. (a) PC, unpatterned; (b) PC, linear pattern with period of 5 μm ; (c) TXL, unpatterned; (d) TXL, linear pattern with period of 3 μm ; (e) TXL, linear pattern with period of 5 μm ; (f) TXL, linear pattern with period of 7 μm ; (g) TXL, linear pattern with period of 9 μm . (Green fluorescence – antibody against Human E-selectin with secondary antibody conjugated with FITC and red fluorescence-propidium iodide).

The cells grown on the linear TXL patterns show different levels of E-selectin expression. According to the CLSM images, HPFs seeded on linear patterns with a period of 3 μm (Fig. 47d) and 5 μm (Fig. 47e) show FITC-based green fluorescence signals. However, cells seeded on line patterns with 7 μm (Fig. 47f) and 9 μm (Fig. 47g) demonstrate weaker or virtually non-existent green fluorescent signals. In addition, green fluorescence is absent when cells are seeded on unmodified TXL (Fig. 47c). For the purpose of positive control, HPFs seeded on unmodified TXL were treated with tumor necrosis factor (TNF- α), and the cells displayed similar fluorescent signals to the cells seeded on line patterns with 3 μm and 5 μm .

4.6.2 Quantitative measurement of E-selectin expression by FACS

In agreement with the CLSM characterization, there exists a clear correlation between pattern period and the degree of E-selectin expression, which were quantitatively measured by using fluorescence activated cell sorting (FACS) (Fig. 48).

The E-selectin expression is reciprocally proportional to the period of linear patterns ablated on TXL. For example, HPF seeded on TXL with linear pattern of 3 μm period for 3 days showed almost 17 times higher in E-selectin expression than the cells seeded on unmodified TXL. Similarly, cells seeded on TXL with linear pattern of 5 μm groove width showed about 14 times higher in E-selectin expression than the cells seeded on unmodified TXL. However, the expression became weaker when the period is widened to 7 μm and 9 μm ; cells seeded on such linear patterns showed 8 times higher in E-selectin expression than the cells seeded on unpatterned polymer. Besides, the cells seeded on TXL treated by one laser beam without surface patterns expressed 4 times higher E-selectin than that on untreated TXL. Moreover, HPFs cultured for 7 days displayed a similar trend. The cells seeded on TXL with line pattern of 3 μm period had 16 times higher E-selectin expression than the cells seeded on unpatterned one and 13 times higher when the period is 5 μm . However, with regard to patterns with period of 7 μm and 9 μm , cells are only 3 to 5 times higher in E-selectin expression than those

seeded on unpatterned polymer. In addition, the cells seeded on laser-treated TXL without surface patterns expressed approximately 2 times higher E-selectin than those on non laser-treated TXL. Comparing the E-selectin expression of 3 days with that of 7 days, it is clear that E-selectin expression of the 7 days cell culture is always higher than that of the 3 days cell culture. The E-selectin expression of HPFs seeded on TXL with a period of 3 μm and 5 μm for 7 days is almost 3 times higher than that of the 3 days culture.

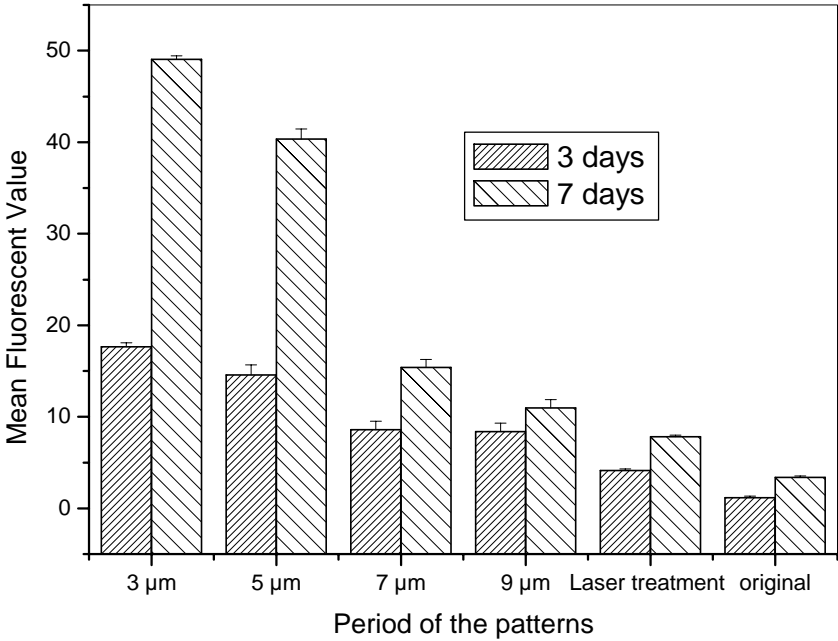


Fig. 48 Data of FACS measurement of HPFs seeded on TXL bearing line pattern with different period.

5 Discussion

5.1 Light excitation of PET and PC

Absorption of ultraviolet and visible radiation in organic molecules is restricted to certain functional groups (chromophores) that contain valence electrons of low excitation energy. Absorption bands observed in the UV-visible region relate to the transition of orbital occupations, so viewing electronic transitions helps identify excited states available for both kinetic and photochemical reactions. Aromatic benzene rings and carbonyl groups composing the main molecular skeleton of the PET and PC molecules are associated to the light excitation and chain decomposition behavior during laser ablation. The polymers used in this study contain σ , π and n orbitals which can be excited to higher σ^* or π^* orbitals by UV light as described in Fig. 2. The absorption of 266 nm leads to $n \rightarrow \pi^*$ or $\pi \rightarrow \pi^*$ transitions.

5.1.1 Calculation of the molecular orbitals by using CAChe

Quantum mechanical calculations of the ground and excited states are carried out using CAChe WorkSystem Pro Version 6.1.12.33 of the program package ZINDO (Professor M. C. Zerner's Intermediate Neglect of Differential Overlap program) developed at the University of Florida Quantum Theory Project. ZINDO computes semi-empirical quantum mechanical values for properties and spectra of molecules with two methods: a method for computing spectroscopic properties (electronic spectra) and a method of computing molecular geometries (conformations and structures). CAChe provides access to ZINDO methods through a Windows environment.

Because the macromolecules are long chains with repeated units, it is unnecessary and also impossible to calculate all MOs of a whole macromolecule. Therefore, a chain which can well

represent the whole molecule was selected (Fig. 50 and Fig. 52). The UV-visible electronic transitions are calculated with ZINDO using INDO/S parameters after optimizing geometry in mechanics using augmented MM3 parameters.

From the calculated UV/VIS spectrum of PET (Fig. 49), a relative weak absorption peak is observed at 354 nm, which can be assigned to $n \rightarrow \pi^*$ transition. The excitation at 283 nm ($n \rightarrow \pi^*$) relates to the laser ablation performed in this study. In its ground state (Fig. 50a), the electronic cloud of HOMO-1 (HOMO: highest occupied molecular orbital) accumulates around the four C-atoms connected with H-atoms. After excitation, the electronic cloud is partly shifted to  bond; meanwhile, the density on aromatic C-atoms decreases (Fig. 50b). As comparison, the excitation at 197 nm is shown in Fig. 50c and d. In excited state the electronic cloud is pulled partly from aromatic C-atoms to C=O group. As a result, the excitation is in favor of the bond breaking between the benzene ring and C=O group. It should be indicated that the electronic cloud which isn't included in this excitation isn't shown in the photograph.

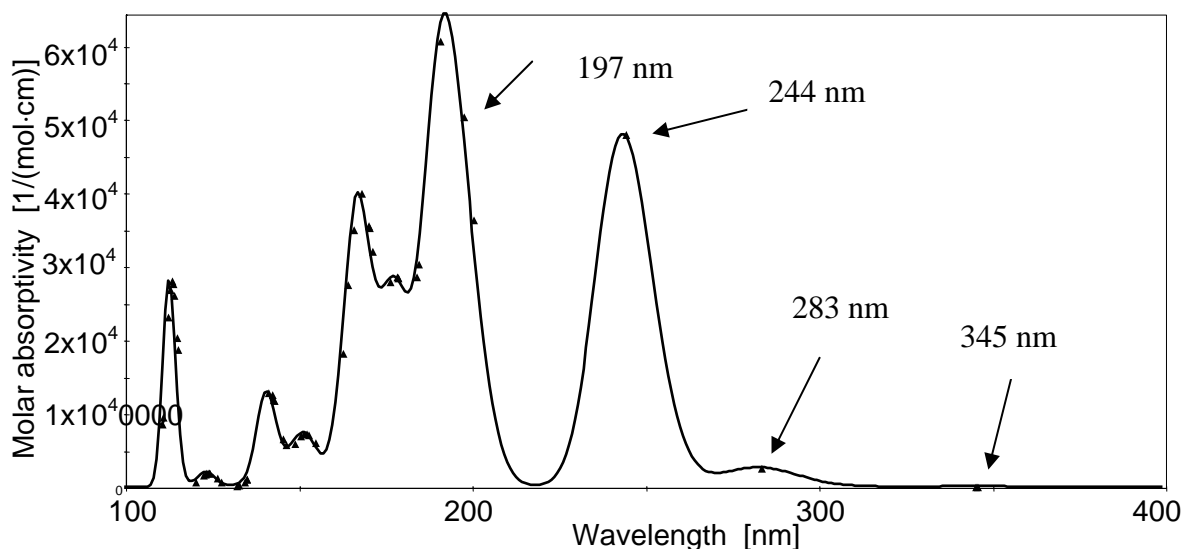
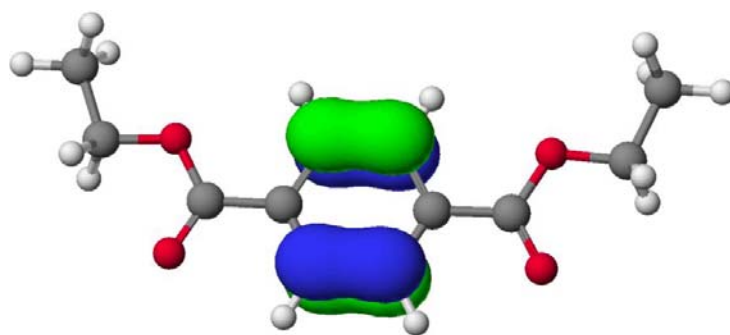


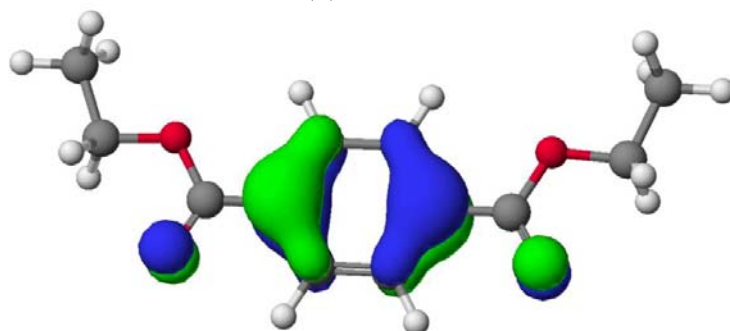
Fig. 49 UV Absorption of PET calculated by using CAChe.



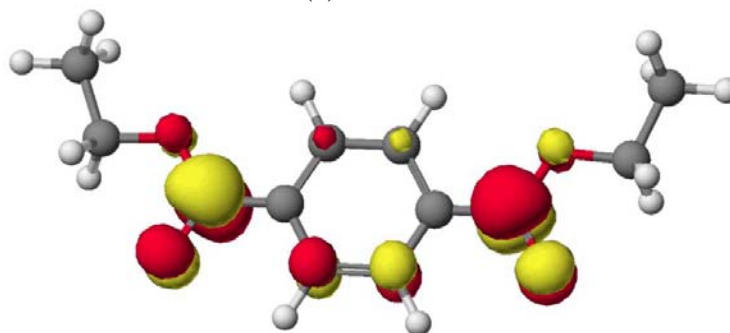
(a) HOMO-1



(b) LUMO



(c) HOMO



(d) LUMO+2

Fig. 50 The distribution of the electronic cloud of (a) HOMO-1, (b) LUMO, (c) HOMO and (d) LUMO+2 in PET calculated by using CAChe. The excitation from HOMO-1→LUMO can be excited by 283 nm and from HOMO→LUMO+2 by 197 nm. The colour represents the MO polarity (for HOMO, blue: positive, green: negative; for LUMO, red: positive, yellow: negative).

The calculated UV spectrum of PC is shown in Fig. 51 in which three absorption peaks near 270 nm are observed, which can be assigned to $n \rightarrow \pi^*$ transitions. The MOs associated with the excitation at 267 nm (HOMO \rightarrow LUMO+2) are shown in Fig. 52. Compared with excitation of PET near this wavelength, the electronic cloud around the aromatic C-atom connected with C=O group decreases (Fig. 52b). Thus, a direct bond breaking in the excited state is possible.

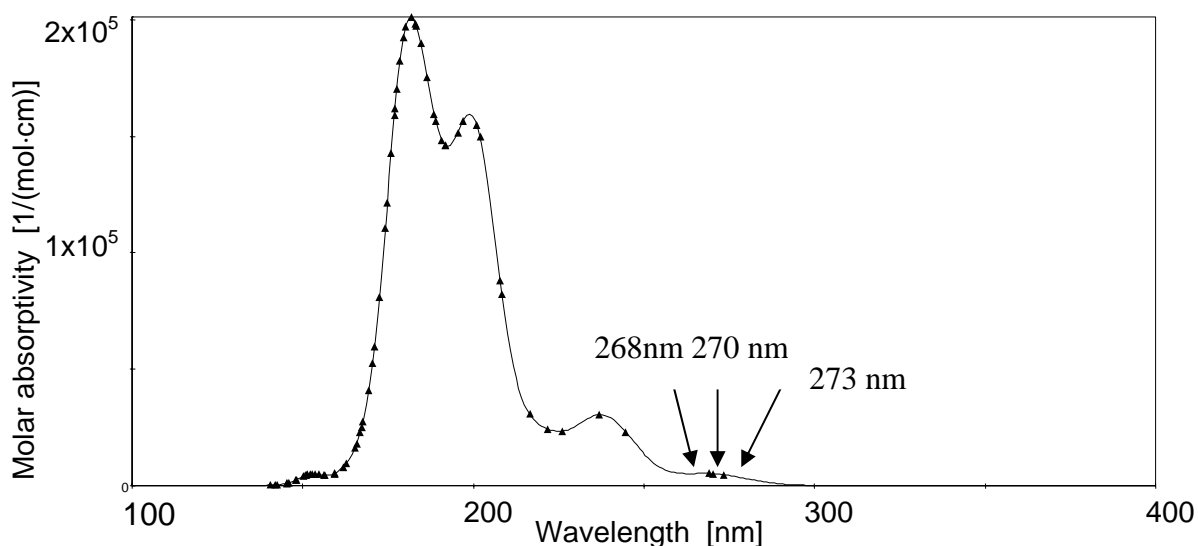


Fig. 51 UV spectrum of PC calculated by using CAChe.

The MOs discussed above are calculated using free molecules with optimized geometry. When the molecules form a dimer or an aggregate, the proximity of the orbitals of the different molecules induce a splitting of the HOMO and LUMO energy levels. This splitting produces vibrational sublevels that have their own energy, slightly different from one another. There are as many vibrational sublevels as there are molecules that interact together. When there are enough molecules influencing each other (e.g. in solid polymer materials), there are so many sublevels that their discrete nature is no longer perceived: they form a continuum-energy bands. Therefore, the calculated spectrum differs normally from the one measured

with solid polymer or polymer solution. Nevertheless, this calculation is very helpful to understand light-organic molecule interactions and laser ablation mechanisms.

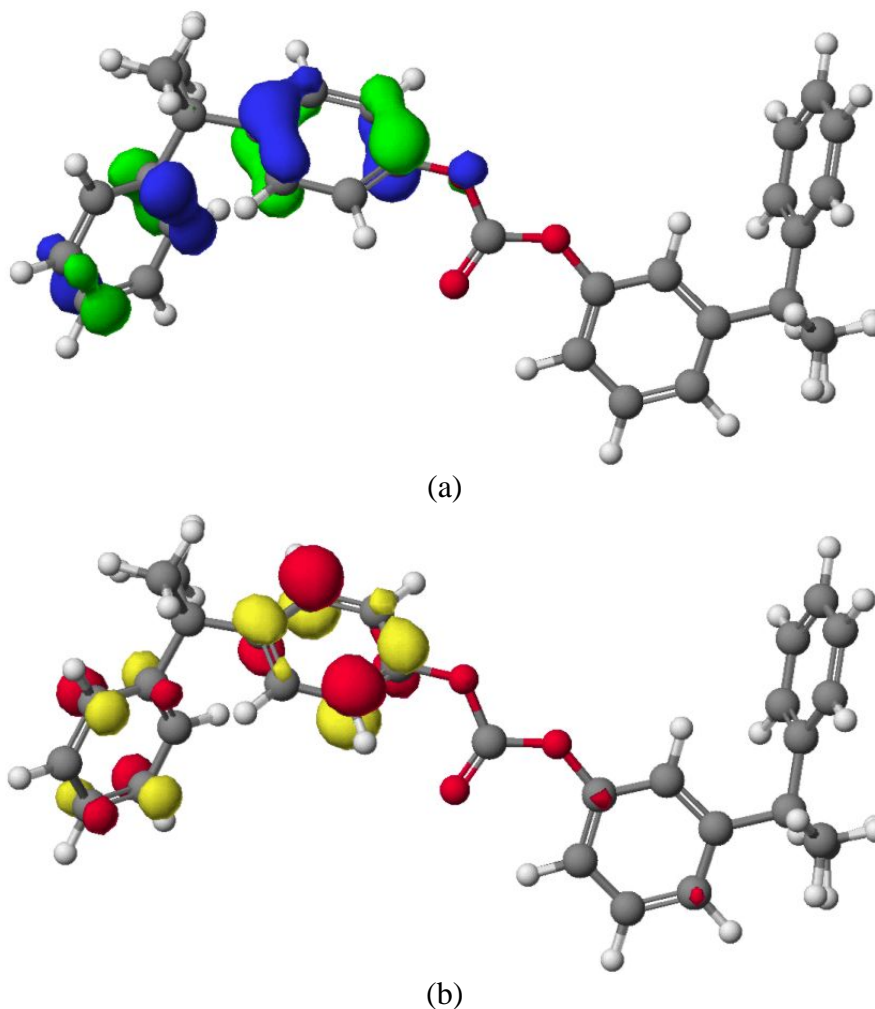


Fig. 52 The distribution of the electronic cloud of (a) HOMO and (b) LUMO+1 in PC calculated by using CAChe. The transition HOMO→LUMO+1 is excited by 267 nm.

5.2 Mechanisms of laser ablation of polymers

5.2.1 Significance of laser ablation curves

The laser ablation behavior can be described briefly by the so-called ablation curve (etching rate vs. laser fluence) without considering the concrete decomposition processes. As shown in

Fig. 21, the ablation was detectable only above a definite fluence, then increased with laser influence, and saturated at higher fluence. The threshold fluence (F_{th}) is normally received by extrapolating the logarithmic linear part of the curve to zero etching rate. Practically F_{th} reflects the relative sensitivity of the polymer to the laser irradiation. Therefore, the sequence of sensitivity of the three polymers used in this study is PC (0.08 J/cm^2) > TXL (0.1 J/cm^2) > PET (0.2 J/cm^2), which is in agreement with the calculation of the MO transition near 266 nm. Nevertheless, it is often argued if such threshold fluence really exists based on the fact that polymer properties could be modified below F_{th} [107].

Küper et al. [108] measured the near-threshold behavior in the ablation of polyimide (PI) with 4 UV lasers. Single-shot measurements were performed, using a sensitive quartz crystal microbalance technique. The curve for 193 nm satisfies the Lambert-Beer's law showing that photochemical effect dominates the ablation, while the curve for 351 nm meets the Arrhenius law approximately. The other curves lie between these two curves showing the transitional mechanisms. Comparing the ablation curves of PET, Thermanox and PC (Fig. 21) with Fig. 53, it can be supposed that the ablation of these commercial polymers at 266 nm satisfies neither photothermal nor photochemical mechanism.

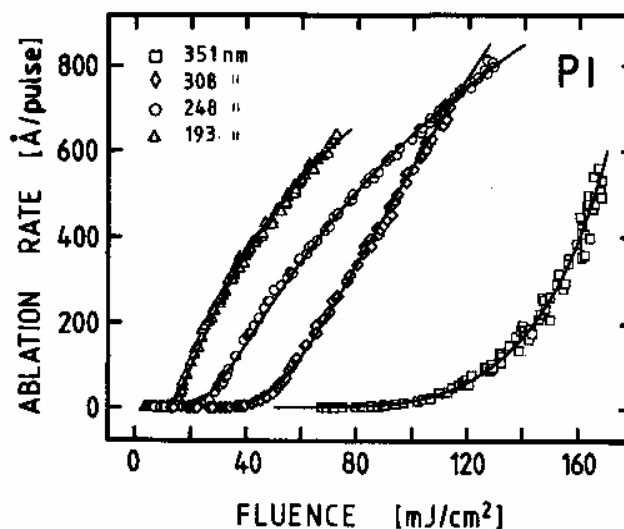


Fig. 53 Ablation curves of PI at different laser wavelength [108]

The ablation curves (Fig. 21) obtained from different pulses don't support the claim that the etching rate varies with pulse number because the surface chemistry of the polymer is modified after first pulse irradiation [110]. The same curves have been found up to 10 pulses under the given experimental conditions, indicating that the modification is not strong enough or too thin to influence etching rate obviously.

As all experimental results, the etching rate saturated at higher fluence. This is often explained by the screening effect of the plasma and species induced by laser ablation. This is true for long-pulse laser such as ns laser. However, the irradiation of a fs laser is finished before the plasma is initiated. In experiments with pulse durations of a few tens of picoseconds, a plasma plume appears after tens of picoseconds, consisting of electrons, and atomic and ionic mass [111-112]. In some experiments with pulse durations of several nanoseconds the ejection of clusters and larger particles is observed up to several hundred nanoseconds after the laser pulse. Besides, high laser intensity may arouse nonlinear absorption that reduces the penetration depth of the laser beam. Under any circumstance, the nature of the logarithmic attenuation of the light intensity in the polymer leads to the saturation of etching rate.

5.2.2 Surface topography

The ripples on Thermanox surface demonstrate the photothermal effect clearly. Such patterns induced by laser irradiation of hundreds of pulses were reported earlier [39-40] when the laser fluence slightly exceeds the laser threshold. Fig. 54 shows a schematic model to explain the formation of the ripples on polymer surface, which was given originally by Kesting et al. [39]. It consists of the ablation layer (surface to X_d in diagram), the fusion layer (X_d to X_m), and the layer which was heated above the glass transition temperature (X_m to X_g). Such a surface depth profile was measured by an electron probe surface analyser, and the depths of the

ablation layer and of the fusion layer were calculated. The thickness of each layer increased with the increase of irradiation energy.

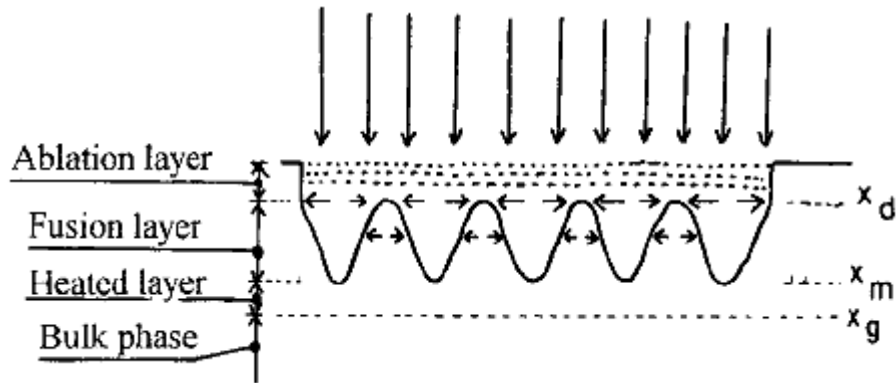


Fig. 54 Modified model of PET film surface by excimer laser irradiation [39-40]

In this study, only patterns with larger period on PET and PC have been observed. However, the ripples appear on Thermanox in a much wider region of laser fluence and pulse number than reported ever before. At low fluence, the patterns were found as cracks similar to the texture of sintered ceramics, showing that the fusion layer is too thin to form the ripples. With increase of laser fluence, the fusion layer becomes thicker, and the necessary pulse number decreases as small as to 5 at 7 J/cm².

5.2.3 Chemical surface modification

According to XPS analysis of PET samples, the O content decreases while the C content increases with increase of laser fluence: This is in agreement with the results obtained by Lazare and Srinivasan [109] and by Watanabe and Yamamoto using KrF excimer laser (248 nm) [40]. Further analysis shows that the relative content of C2 and C3 within three C atoms decreases with laser fluence. This suggests that the decomposition took place mainly in ester

group, while the benzene ring is relative stable. This process is mainly a carbonization caused by photothermal pyrolysis which is supported by MO calculation.

In contrast to PET, the C/O ratios of all laser ablated PC samples are slightly lower than untreated PC. This suggests an oxidation process during laser ablation, which is reflected by the large decrease of the contact angle after laser ablation (Fig. 23). The similar tendency is found for the pulse number dependence, which differs from the results by Lemoine et al. [113], where the laser ablation was performed with a KrF excimer laser (248 nm) and carbonization was observed. However, Laurens et al. [107] reported that the C/O ratio remains nearly unchanged (slightly decrease) with pulse number at 248 nm (KrF excimer laser) in the air, but significant increase (carbonization) was observed at 193 nm (ArF excimer laser) under same conditions. Combining with the different excitation at different wavelengths, it can be concluded that the laser wavelength determines the ablation mechanism through specific excitation and thus results in different surface chemical modifications.

5.2.4 Species emitted during laser ablation

According to ToF-MS results, CO and CO₂ were emitted from PET and PC when they were irradiated by low laser fluence, which is in agreement with results of Watanabe and Yamamoto [40]. Therefore, it can be deduced that the chain decomposition occurs mainly near the ester group, while the benzene group is relative stable. The dissociation energy of various chemical bonds in PC can confirm this assumption (Fig. 55) [114]. The weakest bond is CH₂-C followed by OC-O, whereas the dissociation energy of C-C bond in benzene ring is two times as that of these two chemical bonds. As a result, it can be expected that the content of benzene group will increase after laser ablation, which has been verified by the XPS measurements. Nevertheless, after laser treatment with different fluence and pulses C/O ratios of PC are slightly lower than that of the untreated, revealing that oxidation occurs.

At high laser fluence, the benzene group could also pyrolyze because of the high temperature. However, in most circumstances it was rejected as a whole together with other groups and atoms. Thus, various specific peaks between 70-250 amu were detected. Due to the limited resolution, it is difficult to assign their chemical structure. On the other hand, ToF-MS spectra after 900 pulses demonstrate different laser ablation behavior because of the variation of chemical component caused by the prior laser irradiation. These results can help us better understand laser ablation mechanisms.

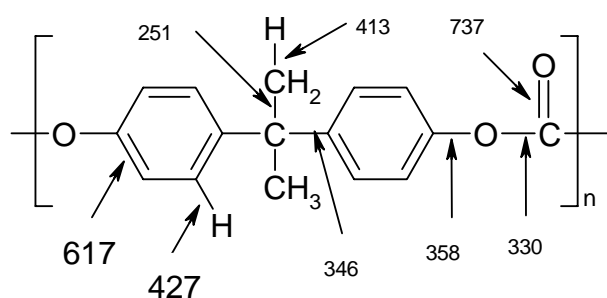


Fig. 55 Bond dissociation energy of polycarbonate in kJ/mol (according to [114])

5.2.5 Evidence of photochemical laser ablation of polymers

Up to now, there is no evidence for pure photochemical laser ablation because the laser ablation was always performed with solid state polymers and the photothermal effect couldn't be avoided. The aim of laser ablation of the thin PC solution is to study if the laser ablation occurs at 266 nm without photothermal effect. Therefore, the temperature evolution of the solution during laser irradiation should be considered first. The temperature increase during laser ablation can be calculated by solving Eq. 2-16 with numerical method under following assumptions and boundary conditions:

- (1) all laser energy is converted to thermal energy to heat the solution,
- (2) no energy exchange between the solution and the cuvette and no energy loss due to irradiation,

(3) the temperature is always 300 K (room temperature) at $z = 0.2$ cm (irradiation depth at 0.2 cm).

Fig. 56 shows the simulated temperature evolution when the solution is irradiated by a 700 mW laser pulse (184 mJ/cm²). It is observed that the temperature increases less than 2 °C which can be neglected with respect to the thermal influence on polymer decomposition. On the other hand, THF isn't excited by 266 nm laser (see UV spectrum of THF in Fig. 29) to initiate reactions (possible polymerisation of THF) that may influence the M_n value of the PC after laser ablation. NMR spectrum of PC ablated in THF confirms this conclusion, from which the chemical shift $\delta=3.39$ isn't observed. As a result, it can be concluded that the decomposition of PC was caused by direct photochemical bond breaking.

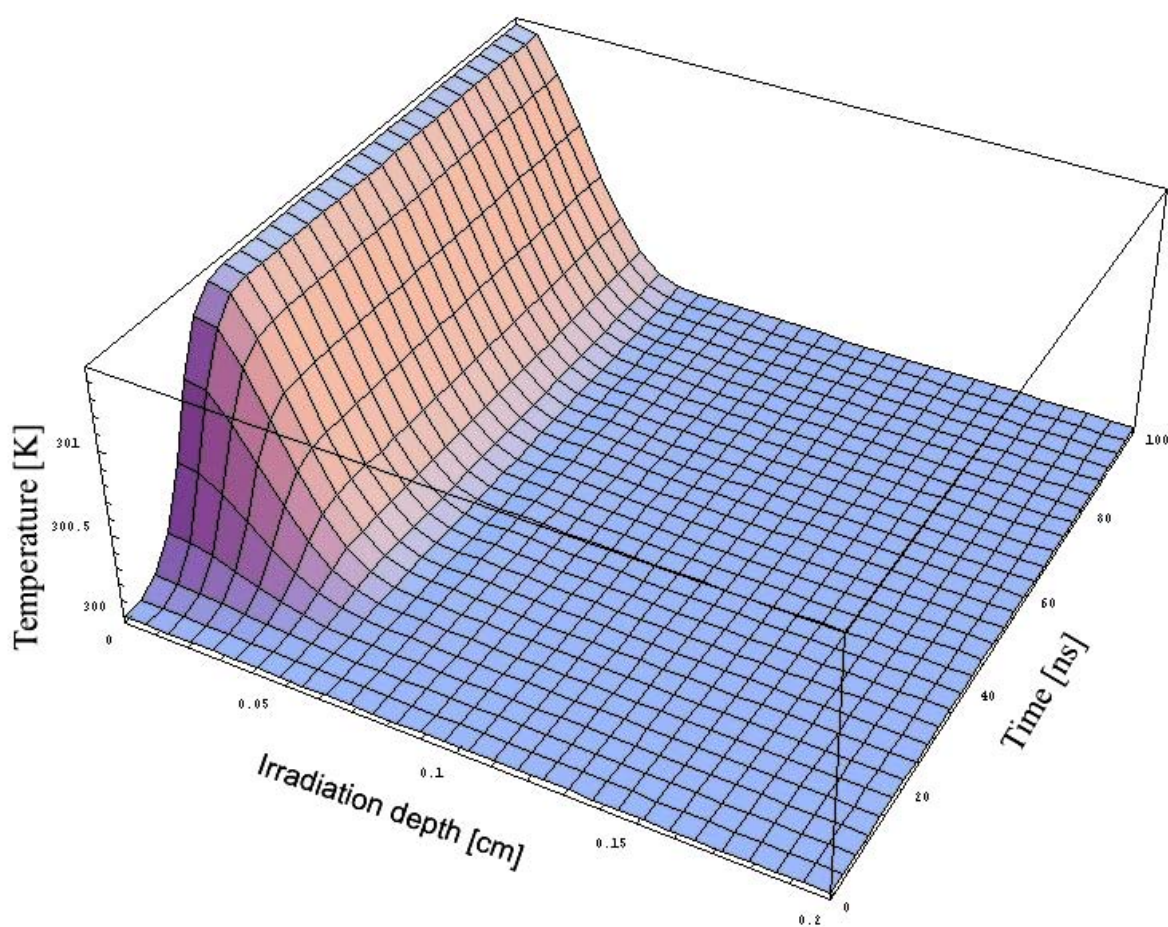


Fig. 56 Temperature evolution of the PC solution during laser irradiation (ρ : 0.889 g/cm³, α : 85 cm⁻¹, C_p : 1.72 J/(g·K), κ : 0.112 J/(m·K·s), energy density: 184 mJ/cm²)

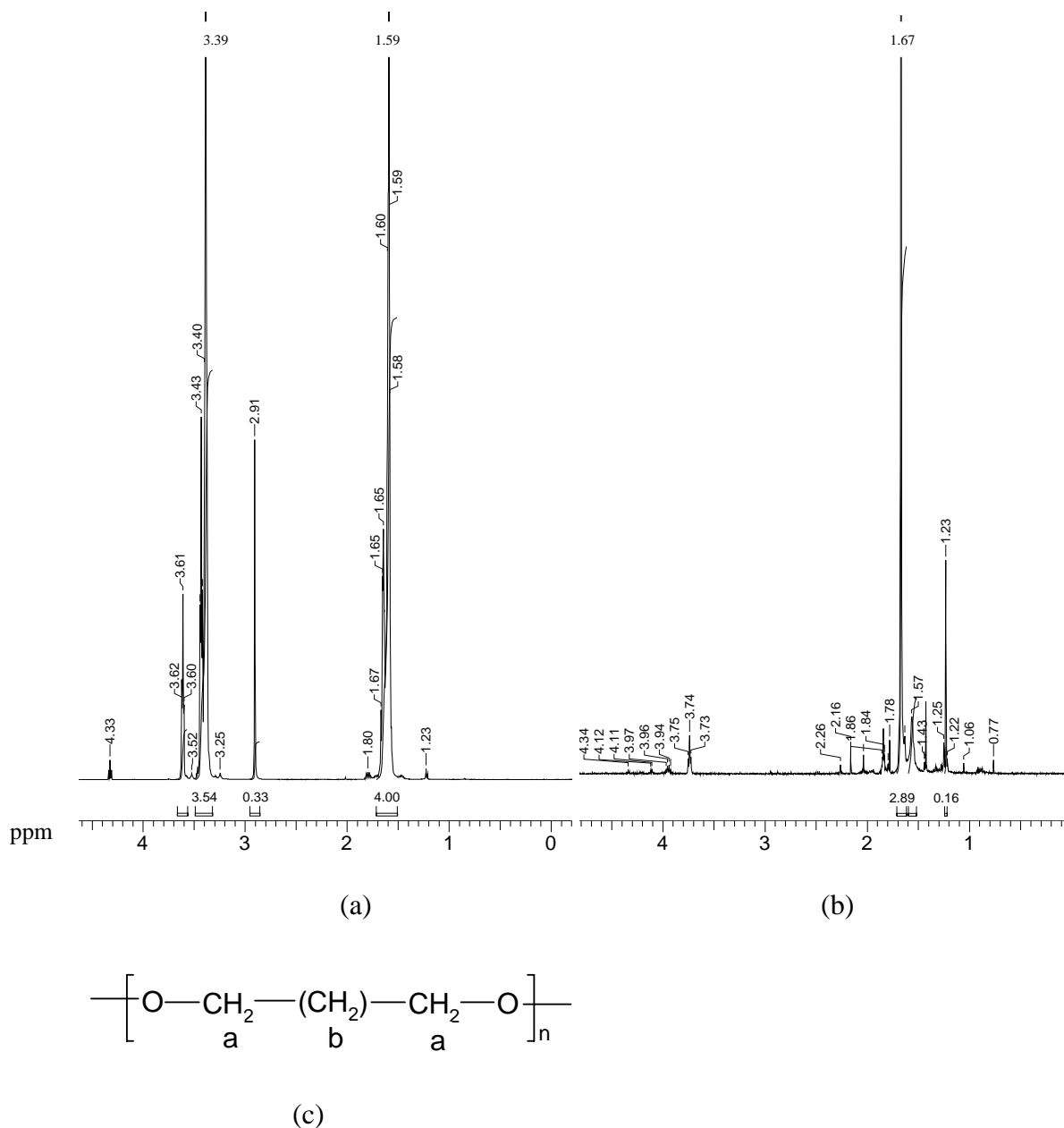


Fig. 57 NMR spectra of (a) PTHF received from Fluka, (b) PC ablated in THF and dried and (c) chemical structure of PTHF (δ for H-atom a: 3.39, for b 1.59)

Furthermore, the quantum efficiency of laser ablation is important to study laser ablation mechanisms. The number of main chain scission S per original molecule is related to $M_{n(0)}$ for undegraded polymer and $M_{n(F, p)}$ after p pulses irradiation at fluence F by equation

$$S = \frac{w}{M_{n(0)}} \left(\frac{M_{n(0)}}{M_{n(F,p)}} - 1 \right), \quad \text{Eq. 5-1}$$

where M_n is the number average molecular weight and w is the weight in grams of irradiated polymer. The quantum yield for main chain scission (ϕ_s) is given by

$$\phi_s = \frac{1}{M_{n(0)}} \frac{S}{E_s} = \frac{w}{E_s M_{n(0)}^2} \left(\frac{M_{n(0)}}{M_{n(F,p)}} - 1 \right), \quad \text{Eq. 5-2}$$

where E_s is the energy of irradiation absorbed for main chain scission in Einsteins per gram of polymer. From Fig. 31 and Eq. 5-2, the quantum yield is calculated and shown in Fig. 58. The quantum yield ϕ_s decreases with laser fluence, which is caused by recombination of the radicals. At low fluence, only a small number of radicals were produced, thus the possibility of a radical to recombine with neighbouring one is low. At high fluence, the quantum yield is reduced due to higher radical density and consequent high recombination possibility.

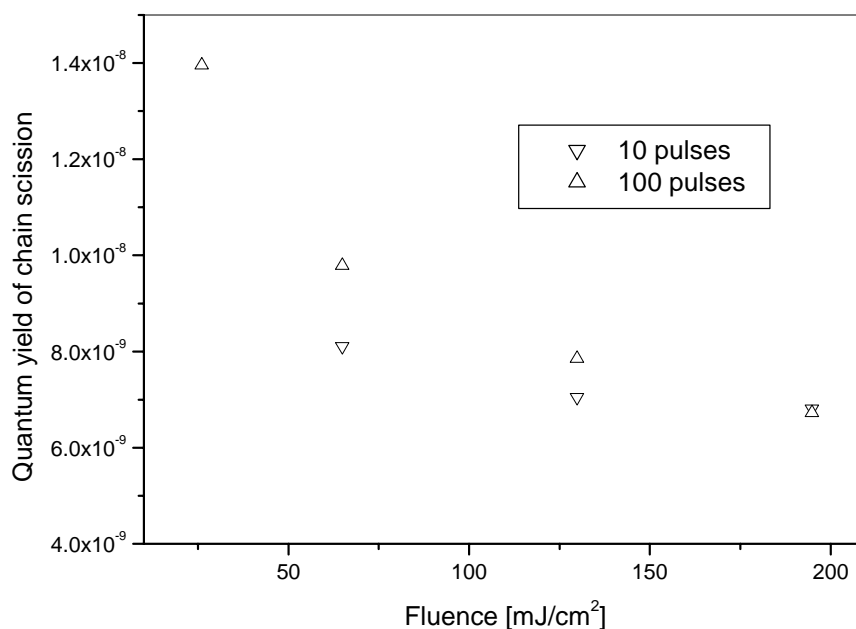


Fig. 58 Quantum yield of main chain scission of PC in THF treated by laser at 266 nm

The quantum yield varies between 1×10^{-8} and 6×10^{-9} , which is relatively small compared with results in the literature [25] in which ϕ_s is from 10^{-1} to 10^{-5} . Low ϕ_s suggests that the photochemical ablation contributes only finitely to the whole ablation effect in bulk materials. It is impossible to perform the same study with PET because PET has no suitable solvents.

5.2.6 Summary of laser ablation mechanisms and processes

According to the discussions above and reports from other authors, the mechanism of laser ablation of PC and PET at high fluence may be explained as a combination of photochemical, photothermal and mechanical effects which are associated with polymer chemical structures, laser wavelength and fluence.

Polymer chemical structure and laser wavelength

These two factors determine the OM transitions jointly. A polymer can be excited and ablated by a laser only when they match each other. A definite laser can excite different transitions in different polymers, and thus result in different ablation behavior, e.g. direct photochemical decomposition of PC excited by 266 nm laser occurs more readily than that of PET.

Laser fluence

For given polymer and laser, the fluence plays an important role on ablation mechanism if any modification occurs. At very low fluence, e.g. as low as sunshine or a lamp, radicals occur only spontaneously, which may initiate further reactions and cause crosslinking of macromolecules. The consequence is the same as the weathering of the polymers in normal conditions. This is why PET was also modified chemically by laser irradiation below the threshold [41]. Since there is no significant temperature increase, the process is a pure photochemical effect. Raising the fluence up to slightly below ablation threshold, the

chemical bonding breaks in a higher density, and CO₂ and CO may be emitted. At this point, photochemical effect still dominates the laser decomposition although the temperature may rise to play a definite role. Above the ablation threshold, photothermal effect plays a more and more important role because the temperature increases with laser fluence. Far above the ablation threshold, the temperature will be increased so high that the photothermal effect will dominate the ablation. Species, such as radicals, ions, polymer chain segment, as well as small melting drops, will be ejected out of the ablation crater with an ultrasonic velocity. At this time, bright plasma plume can be observed and clear cracks can be heard. The mechanical effect will also contribute to the final ablation effect. Furthermore, the nonlinear absorption may lead to direct chemical decomposition which is impossible under normal absorption.

5.3 Laser interference lithography

5.3.1 Mechanism

Micropatterning by LIL was performed normally at high laser fluence, far beyond ablation threshold. At least the laser fluence must exceed a definite value in order that the micropatterning can be detected. Slightly above this value, the ablation rate is still very small and the resulted pattern depth may be only several to tenth nanometer. On the other hand, the patterns are inhomogeneous and can't find any applications. For the sake to study contact guidance, the patterns with minimal depth of 0.5 μm are expected and the corresponding fluence is needed. As discussed above, photochemical, photothermal and mechanical effects contribute to micropatterning jointly. Fig. 59 demonstrates the process of the micropattern formation schematically. Similar to one-beam laser ablation, the polymer was excited, heated and ablated by photochemical and photothermal effects. Large amount of species were generated in form of plasma and vapor within several ns, which is limited between pattern

grooves. Because of the great pressure difference and high dynamic energy the species possess, they were ejected out of the grooves in very high velocity and simultaneously exerted large pressure against the adjacent bulk polymer. Meanwhile, the thermal energy diffuses into bulk material to melt a layer of polymer whose thickness depends on the position and laser fluence. Part of the melted polymer will be ejected out of the groove and solidify on the top of ridges.

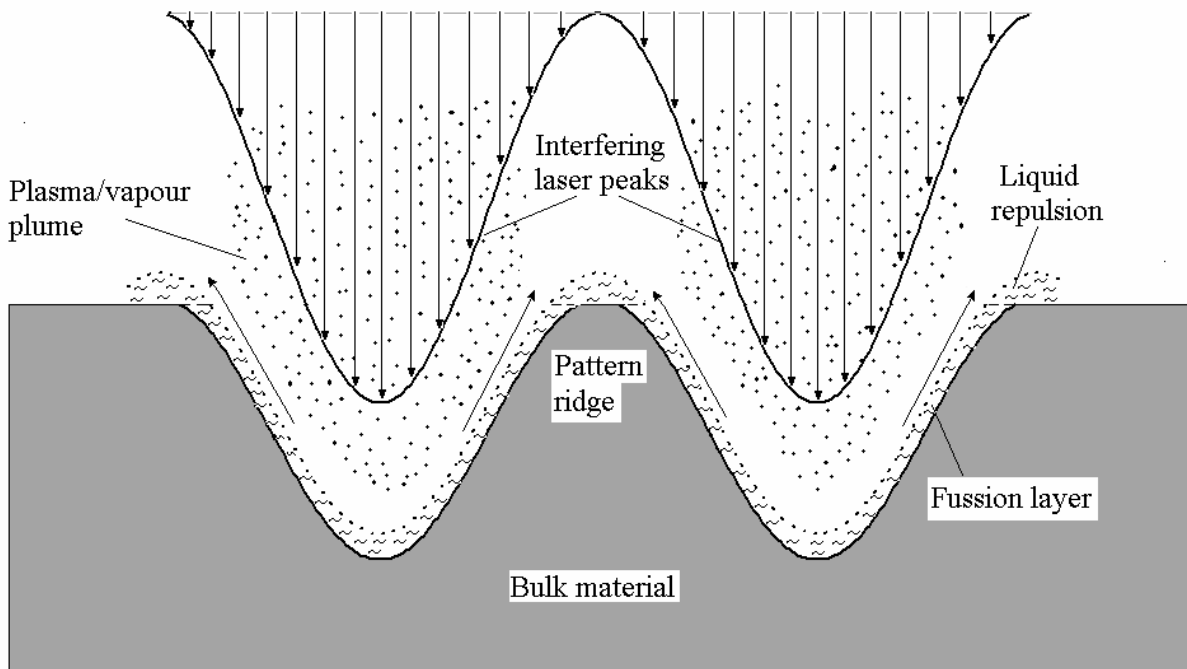


Fig. 59 Principle of laser interference lithography

5.3.2 Period and depth

According to Eq.2-30, the period can be varied from several hundred nanometers up to 20 μm . For example, the period can be as small as 200 nm when the angle is enlarged to 75°. However, the period can't be smaller than the thermal diffusion length l_d

$$l_d = \left(\frac{\kappa \cdot \Delta\tau}{\rho C_p} \right)^{1/2} \quad \text{Eq. 5-3}$$

where κ is the thermal conductivity, $\Delta\tau$ is pulse width, ρ is density and C_p is specific heat capacity.

Table 7 shows that l_d of PET and PC is smaller than the resolution of LIL so that the influence of thermal diffusion can be neglected with respect to achievable periods. However, the fusion layer caused by laser irradiation is much thicker. According to the calculation of Watanabe [40], the fusion layer is about 30 nm when a PET film was irradiated by 0.1 J/cm² KrF excimer laser. Considering the high energy density used by LIL, e.g. 0.4 J/cm² (0.8 J/cm² at interference peaks), the thickness of the total fusion layer from both side of a ridge can reach several hundred nanometers (ref. Fig. 59). Together with the mechanical effect, small period (<1 μm) is only feasible on thermosetting polymers [23] by which no fusion layer appears, or photosensitive polymers [63] by which low laser fluence is needed. Though the patterns with a period smaller than 1 μm were realized at relatively low fluence on PC, PET and TXL, but their depth (smaller than 0.5 μm) and homogeneity are not enough for the purpose of this study.

Table 7 Properties of PET and PC associated with thermal diffusion length

Property	κ [W/(m·K)] ¹	$\Delta\tau$ [ns]	ρ [g/cm ³] ¹	C_p [J/g·K] ¹	l_d [nm]
PET	0.15-0.4	10	1.35	1.3	29.2-47.7
PC	0.2	10	1.20	1.2	37.3

For large period (> 10 μm) with the experimental setup shown in Fig. 8, the angle between two laser beams must be smaller than 1.5°, which will result in difficulties to adjust the angle exactly because of the requisite long optical path and the limited work table. Thus, the suitable period extends from 1 to 10 μm , corresponding to the angle from 30° to 1.5° between two beams.

¹ According to the technical data of PET and PC from Goodfellow.

Laser ablation mechanisms influence also the pattern profile. The melted polymer rejected from the melting layer may resolidify on the top of ridges to heighten the pattern depth. The evidence can be found by a TXL pattern (Fig. 60b).

With one pulse, the pattern depth hasn't exceeded 1 μm on PET and PC, and 2 μm on Thermanox due to the saturation of the etching rate. Deeper patterns can only be obtained with several laser pulses and moderate fluence in order to avoid thicker fusion layer and strong mechanical effect.

5.3.3 Surface topography and chemical modification

The surface topography of the micropatterns is show in Fig. 60. The micropatterned TXL surface is much rougher than that of PET and PC, indicating more thermal influence on TXL.

This was confirmed by the results of one-beam ablation (Fig. 22).

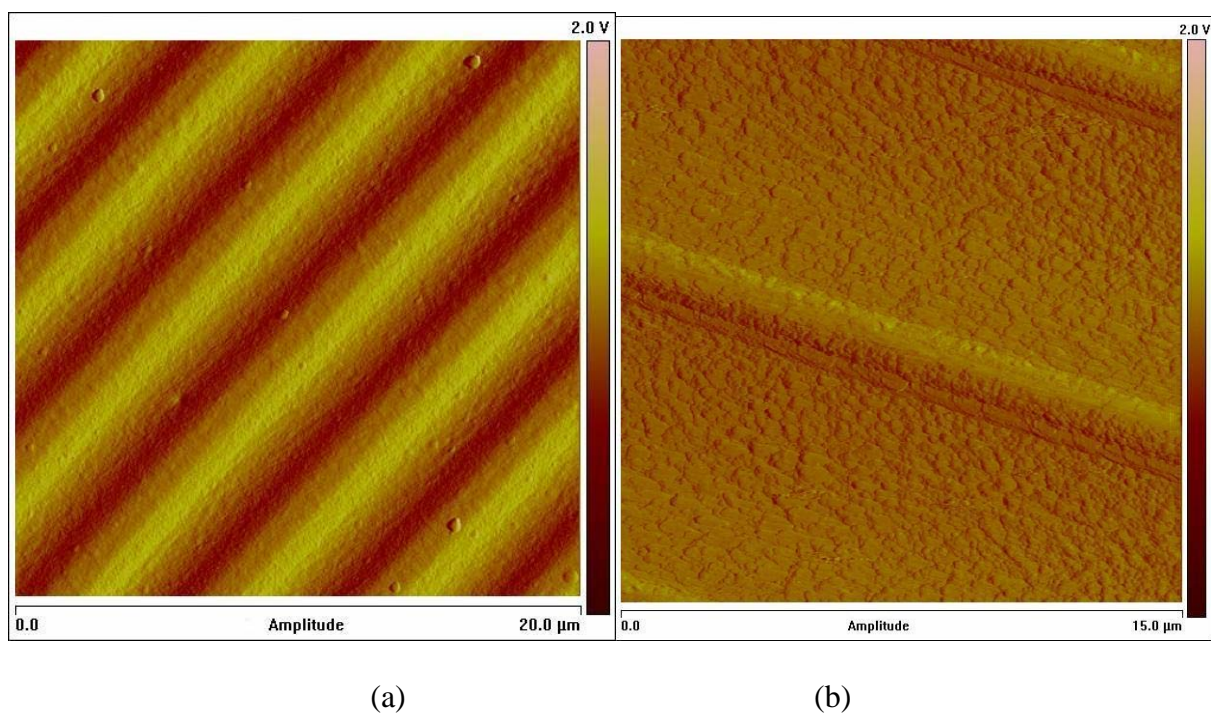


Fig. 60 AFM photographs of (a) PET with a period of 5 μm and depth of 0.89 μm and (b) TXL with a period of 9.7 μm and depth of 0.93 μm .

The XPS measurements have shown that the laser ablation resulted in chemical surface modification. The periodic energy distribution of the interference pattern will result in chemical surface modification with the same period as the micropatterns. The strongest influence occurs in the valley, but the top of the ridges is also modified because of the ejected plasma and resolidified species.

5.4 Cell adhesion on micropatterned polymer surface

5.4.1 Mechanism of contact guidance

Although the effects of micropatterned surface in vitro have been intensively investigated, the mechanism isn't very clear yet. The comparison of the results is very difficult because the experiments were performed with various cells on the micropatterns whose chemical properties and dimensions were not strictly controlled. Early explanations referred to the inflexibility of the cytoskeleton which prevents the total bending of cell protrusions [115]. It was found that protrusions were unable to bend over surface configurations with large angle, i.e., a change in inclination greater than 4° . In this way, the cells were forced to orientate in a direction parallel to the surface patterns. Certainly, it is not true. From Fig. 61 it can be observed that the protrusions of L929 cells have bended themselves more than 4° to accommodate the surface topography.

Recent investigations concentrated on the interactions between focal adhesions, ECM and surface textures. Cells in culture have many protrusions known as lamellopodia. These lamellopodia contain actin filaments, which interact with ECM protein through a transmembrane glycoprotein, integrin [1]; this complex is mainly responsible for the formation of cell morphology, cell movement and attachment to the underneath substrate. A microtextured surface was presumed to possess local differences in surface free energy that

promoted specific deposition pattern of attachment proteins [116-118]. Such difference in surface free energy was also measured in LIL-induced micropatterns, yet it isn't the critical factor that promotes cell orientation in this study since no differences were observed after surface was coated with collagen [119]. Nevertheless, local chemical differences can really lead to cell orientation. Dewez et al. [120] have treated PS surface with cold plasma so that patterns were prepared by difference in hydrophilicity. Mammalian cells adhered to these patterns selectively and orientated along the lines with higher hydrophilicity, where ECM proteins were selectively adsorbed.

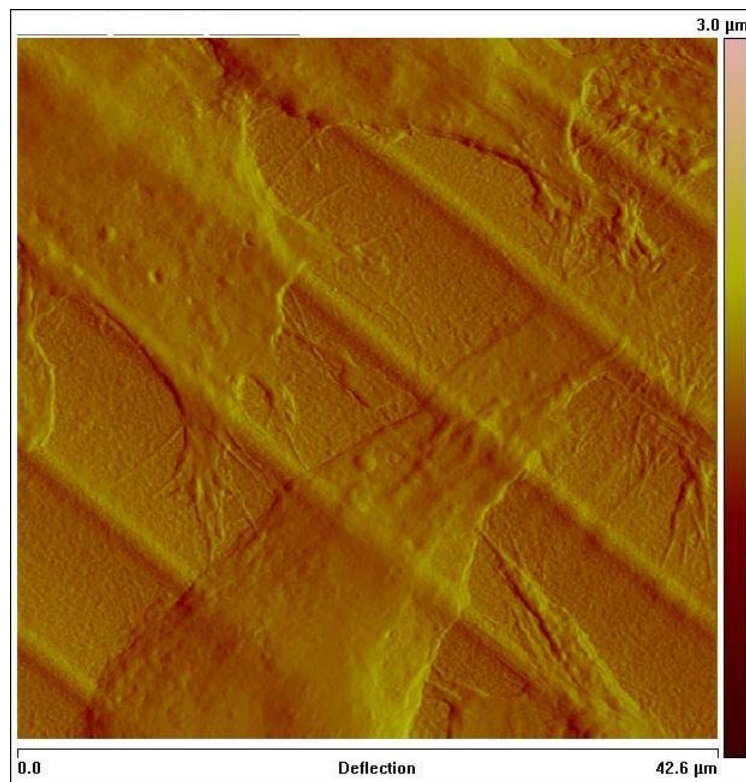


Fig. 61 L929 cells cultured on TXL micropattern with a period of $9.7\mu\text{m}$ and a depth of $0.93\mu\text{m}$. The cells have descended into the grooves and the lamellopodia can be observed.

Jansen et al. [84-121] proposed that micropatterns create a pattern of mechanical stress which influences cell spreading and causes cell alignment. They suggested that cells make

protrusions in all directions to explore their surrounding. The propagation of these structures is directed by the extension of filament actin. When an extension is faced with a surface ridge, propagation is hindered or simply impossible. Only extension along the pattern direction can propagate, and therefore, cell spreading is able to progress in this direction. The reaction to the force generated on action is the main factor that causes contact guidance. The function of the linear patterns lies in its hindrance to cell protrusion. This assumption can well explain why the cells orientate themselves and align along the line direction. However, this model can't explain following phenomena:

- a) Cells can also orientate and align along the chemically modified linear patterns nearly without topographical difference,
- b) Cells on point patterns show also some orientation, but not so clearly as on line patterns (Fig. 45 and Fig. 46),
- c) Cell behaviors differ on linear patterns with different period (Fig. 40).

To develop a model which can be generally used to explain all these phenomena, it is suggested the following extended theory: cell orientation and alignment are initiated by surface chemistry and guided by the patterns available and suitable for adhesion.

Cell orientation occurs as early as at attachment stage. As soon as the cells are seeded to the substrates, they are sensing the environment and searching the surface positions in favour of attachments through chemical and physical signalling. On chemical micropatterned surfaces, they will find these favourable positions within the chemically modified strips, while on topographical micropatterns the attachment is only possible on the top of ridges when the width is not large compared to the cell dimensions. Then, the cells will attach to the substrate, mainly on the area in favour of forming physicochemical linkages between cells and substrate. Protruding their plasma membrane to detect their environment, they will also find the next nearest position in pattern directions and extend along pattern features. This is the contact guidance initiated by surface chemistry. The alignment doesn't require the formation and

alignment of focal adhesion and stress fibres along patterns, which was confirmed by Teixeira et al. [123] with epithelial cells and topographically micropatterned substrates. With time laps microscopy, they observed that lamellopodia protruded preferentially along the pattern direction, although protrusions perpendicular to patterns were not prohibited.

Large amount of investigations reported that cell alignment was significantly influenced by the pattern depth [9, 84, 95, 122, 123]. Clark et al. [95] observed that cell alignment increased with the depth of patterns whose width was in micrometer range and depth was 0.5 μm or larger. On patterns with small period, cells mainly lay on the ridges [84, 123], and tended to descend into the grooves and fill the bottom with increasing lateral pattern features [84, 124].

The HPF cells on point patterns are also elongated as on linear patterns and show somewhat orientation (Fig. 45). It could be also explained with the availability of the attachment points, namely, the point patterns are giving relatively more “spaces” or “platforms” for the cells to attach to, yet limiting the free protrusion of lamellopodia in random directions. In other words, the HPF seeded on point-patterned PC films might experience a condition between “line pattern” and “unmodified surface”, and therefore having some properties of the cells seeded on line-patterned PC films while expressing some properties of the cells seeded on unmodified PC surface.

5.4.2 Cell inflammation on micropatterned polymer surface

Up to now, fewer researches have focused on further influence of surface micropatterns. During adhesion and orientation cells experience complicated interactions with the surface chemistry and topography. For example, the integrins are the major receptors responsible for the attachment of cells to the ECM. At two types of cell-matrix junctions (focal adhesions and hemidesmosomes), the integrins also interact with components of the cytoskeleton to provide a stable linkage between the ECM and adherent cells. In addition to this structural role, the

integrins serve as receptors that activate intracellular signalling pathways, thereby controlling gene expression and other aspects of cell behavior in response to adhesive interactions.

Pu et al. [125] have found that E-selectin expression significantly increased when human umbilical vein endothelial cells (HUVEC) were seeded on non-plasma treated PTFE. In addition, another group has demonstrated that expression of P-selectin rose considerably when endothelial cells were seeded on PET [126]. Since both E-selectin and P-selectin are involved in inflammatory response, it is suspected that biomaterials acting as the substrate of cell adhesion might stimulate inflammation.

How biomaterial surface affects the inflammatory response is not clear but one likely mechanism would be the release of material components from the implant surface [127]. This release can occur by, for instance, biodegradation, resorption or erosion, and the released material can vary from relatively large particles to molecules or even ions.

According to the quantity measurement by FACS, the level of E-selectin expression is strongly related to the period of the micropatterns. The reason behind this phenomenon was unclear. It has been reported that the behaviors of cells changed when the topography of the substrate underneath varied. One of these variations is their inflammatory response caused by the forced orientation. To demonstrate, narrow groove widths induced higher expression of E-selectin but the effect diminished when the groove widths became bigger. The narrow groove widths might establish some limitation for cellular functions such as cell adhesion and movement, which might also produce certain amount of stress to the cells, thus causing the cells to comprehend the substrate as a foreign substance, which might lead to foreign body reaction. In contrast, resulting stress and consequences are diminished when the groove widths are enlarged.

W.G. Brodbeck et al. [128] reported that the surface chemistry of biomaterials might have an effect on cytokine production such that the expression of interleukin 10 (IL-10) increased while the expression of IL-8 significantly decreased when human monocytes/macrophages

adhered to hydrophilic and anionic surface. In contrast, the expression of IL-8 was high when the cells adhered to cationic and hydrophobic surface. Referring to XPS measurement, the carbon content on the surface of the TXL increased while the oxygen content decreased with the increase of laser fluence, which might provide a new environment for cell growth. Nonetheless, the cause of relatively high expression of the inflammatory genes when HPFs were seeded on TXL with surface linear pattern is uncertain. It is sure that both surface chemistry and surface topography in terms of surface pattern might play an essential role in regulating the genes expression. Yet, future works must focus on investigating the surface pattern-induced proinflammatory cytokine expression in order to have a deep understanding of the circumstance.

6 Conclusion and outlook

In this work laser interference lithography was used to prepare different micropatterns on polymer surfaces for studying cell adhesion and orientation on different patterns. Since LIL is based on laser ablation of polymers, the ablation mechanisms were first studied using different methods. A combination process of photothermal and photochemical ablation was explained as the ablation mechanism at 266 nm. The MO calculation can help to understand the different excitations by the light near 266 nm and the laser ablation mechanisms. Especially, with thin polymer solution photochemical ablation was confirmed at 266 nm even under very low fluence. However, quantum yield of chain scission is very low showing that photothermal effect may dominate the ablation under high laser fluence. XPS and AFM measurements show that the surface topography and chemical properties were modified by laser treatment.

Different linear and point micropatterns were prepared with LIL. Adjusting the angle between laser beams, laser fluence and pulse number, the periods from about 1 to 10 μm and the depth up to 5 μm were achieved. The micropatterns are well-defined, reproducible, and of very good consistency. Compared with photolithography, LIL doesn't need expensive facilities and further wet development, but have difficulties to prepare suitable micropatterns with small periods (e.g. $<0.5 \mu\text{m}$) for cell adhesion. As a complementation the FIP (focused ion beam) can be alternative to prepare micropatterns as small as 100 nm or micropatterns with steps.

It is first reported that the micropatterns induced by LIL were successfully used to study cell-surface interactions. The cells oriented themselves on all linear patterns showing very good "contact guidance". However, they underwent inflammatory response which was neglected by nearly all of the similar studies. Mouse fibroblasts and human pulmonary fibroblasts cultured on linear micropatterns of Poly(ethylene terephthalate), ThermanoxTM and polycarbonate

were elongated, spindle-like, and oriented themselves along the line patterns with all different groove widths. In contrast, cells cultured on point patterns were also elongated and showed only some orientation. However, cells cultured on all of the micropatterns induced by LIL show inflammatory responses which were neglected by the most prior studies. It is not clear what results in the inflammation and how to overcome this problem.

Despite careful studies, the following questions still remain unclear and must be answered in future:

- The exact roles of the photothermal and photochemical effect in the ablation of PET, PC and other polymers. Understanding these mechanisms can help design tailored new polymers for scientific and industrial applications.
- Micropatterning of any polymer by using LIL by means of modification, e.g. using dopants or fillers, but without permanently changing the final properties.
- The mechanism of the inflammation caused by the LIL-induced micropatterns and the measures to avoid this response.

7 Reference

- [1] X. F. Walboomers, J. A. Jansen: Cell and tissue behavior on micro-grooved surfaces. *Odontology* **89** (2001) 2-11.
- [2] L. L. Hench, Biomaterials: a forecast for the future: *Biomaterials* **19** (1998) 1419-1423.
- [3] J. S. Temeno, A. G. Mikos: Review: tissue engineering for regeneration of articular cartilage. *Biomaterials* **21** (2000) 431-440.
- [4] H. Shin, S. Jo, Antonios G. Mikos: Biomimetic materials for tissue engineering. *Biomaterials* **24** (2003) 4353-4364.
- [5] G. R. Ramalanjaona, R. F. Kempczinski, J. D. Ogle, E. B. Silberstein: Fibronectin Coating of an Experimental PTFE Vascular Prosthesis. *J. Sur. Res.* **41** (1986) 479-483.
- [6] E. T. den Braber, J. E. de Ruijter, L. A. Ginsel, A. F. von Recum, J. A. Jansen: Quantitative analysis of fibroblast morphology on microgrooved surfaces with various groove and ridge dimensions. *Biomaterials* **17** (1996) 2037-2044.
- [7] A. M. Rajnicek, S. T. Britland, C. D. McCaig: Contact guidance of CNS neurites on grooved quartz: influence of groove dimensions, neuronal age and cell type. *J. Cell Sci.* **7110** (1997) 2905-2913.
- [8] E. T. den Braber, J. E. de Ruijter, H. T. J. Smiths, L. A. Ginsel, A. F. von Recum, J. A. Jansen: Quantitative analysis of cell proliferation and orientation on substrates with uniform parallel surface micro-grooves. *Biomaterials* **17** (1996) 1093-1099.
- [9] A. Curtis, C. Wilkinson: Topographical control of cells. *Biomaterials* **18** (1997) 1573-1583.
- [10] R. Singhvi, G. Stephanopoulos, D. I. C. Wang, Review: effects of substratum morphology on cell physiology. *Biotechnol. Bioeng. Mater.* **43** (1994) 764-71.
- [11] Y. Ito: Surface micropatterning to regulate cell functions. *Biomaterials* **20** (1999) 2333-2342.
- [12] M. Geissler, Y. Xia: Patterning: principles and some new developments. *Adv. Mater.* **16** (2004) 1249-1269.
- [13] G.L.-T. Chiu, J. M. Shaw: Optical lithography: Introduction. *IBM J. Res. Dev.* **41** (1997) 3-4.
- [14] S. D. Fewster, R. R. H. Coombs, J. Kitson, S. Zhou: Precise ultrafine surface texturing of implant materials to improve cellular adhesion and biocompatibility. *Nanobiology* **3** (1994) 210-210.
- [15] C. Satriano, C. E. Conte, G. Marletta: Surface chemical structure and cell adhesion onto ion beam modified polysiloxane. *Langmuir* **17** (2001) 2243-2250.

- [16] A. Oessl, M. D. Garrison, J. B. Lhoest, A. S. Hoffman: Plasma lithography-thin film patterning of polymeric biomaterials by RF plasma polymerization I: Surface preparation and analysis. *J. Biomater. Sci.-Polym. Ed.* **12** (2001) 721-738.
- [17] A. Tourovskaia, T. Barber, B. T. Wickes, D. Hirdes, B. Grin, D. G. Castner, K. E. Healy, A. Folch: Micropatterns of chemisorbed cell adhesion-repellent films using oxygen plasma etching and elastomeric masks. *Langmuir* **19** (2003) 4754-4764.
- [18] S. Srinivasan, W. J. Leigh: Ablative photodecomposition: action of far-ultraviolet (193 nm) laser radiation on poly(ethyleneterephthalate) films. *J. Am. Chem. Soc.* **104** (1982) 6784-6785.
- [19] C. Hallgren, H. Reimers, D. Chakarov, J. Gold, A. Wennerberg: An in vivo study of bone response to implants topographically modified by laser micromachining. *Biomaterials* **24** (2003) 701-710.
- [20] R. Vaidya, L. M. Tender, G. Bradley, M. J. O'Brien II, M. Cone, G. P. López: Computer-controlled laser ablation: a convenient and versatile tool for micropatterning biofunctional synthetic surfaces for applications in biosensing and tissue engineering. *Biotechnol. Prog.* **14** (1998) 371-377.
- [21] Z. Liu, X. K. Meng, T. Recktenwald, F. Mücklich: Patterned intermetallic reaction of Ni₃Al by laser interference structuring. *Mat. Sci. Eng. A* **342** (2003) 101-103.
- [22] C. Daniel, F. Mücklich, Z. Liu: Periodical micro-nano-structuring of metallic surfaces by interfering laser beams. *Appl. Surf. Sci.* **208-209** (2003) 317-321.
- [23] H. M. Phillips, D. L. Callahan, R. Sauerbrey: Sub-100 nm lines produced by direct laser ablation in polyimide. *Appl. Phys. Lett.* **58** (1991) 2761-63.
- [24] M. von Allmen, A. Blatter: *Laser-beam interactions with materials*, 2nd edition, Springer, 1995.
- [25] J. F. Rabek: *Photodegradation of polymers*, Springer, 1996.
- [26] P. Schaaf: Laser nitriding of metals. *Prog. Mater. Sci.*, **47** (2002) 1-161.
- [27] S. Ege: *Organic Chemistry*, 3rd Edition, D. C. Health and Company, 1994.
- [28] R. C. Denny, R. Sinclair: *Visible and ultraviolet spectroscopy*, John Wiley & Sons.
- [29] B. J. Garcia, J. Martinez, J. Piqueras: Laser melting of GaAs covered with thin metal layers. *Appl. Phys. A* **51** (1990) 437-455.
- [30] R. Srinivasan, V. Mayne-Banton: Self-developing photoetching of poly(ethylene terephthalate) films by far-ultraviolet excimer laser radiation. *Appl. Phys. Lett.* **41** (1982) 576-578.
- [31] Y. Kawamura, K. Toyota, and S. Namba: Effective deep ultraviolet photoetching of polymethylmethacrylate by an excimer laser. *Appl. Phys. Lett.* **40** (1982) 374-375.

- [32] P. E. Dyer: Excimer laser polymer ablation: twenty years on. *Appl. Phys. A* **77** (2003) 167-173.
- [33] R. Srinivasan, B. Braren, D. E. Seeger, R. W. Dreyfus: Photochemical cleavage of a polymeric solid: Details of the ultraviolet laser ablation of polymethylmethacrylate at 193 and 248 nm. *Macromolecules* **19** (1986) 916-921.
- [34] V. Srinivasan, M. A. Smrtic, S. V. Babu: Excimer laser etching of polymers. *J. Appl. Phys.* **59** (1986) 3861-3867.
- [35] L. S. Bennett, T. Lippert, H. Furutani, H. Fukumura, H. Masuhara: Laser induced microexplosions of a photosensitive polymer. *Appl. Phys. A* **63** (1996) 327-332.
- [36] D. Pham, L. Tonge, J. Cao, J. Wright, M. Papiernik, E. Harvey, D. Nicolau: Effects of polymer properties on laser ablation behavior. *Smart Mater. Struct.* **11** (2002) 668-674.
- [37] B. J. Garrison, R. Srinivasa: Ablative photodecomposition of polymers. *J. Vac. Sci. Technol. A* **3** (1985) 746-748.
- [38] P. E. Dyer, D. M. Karnakis, P. H. Key, J. P. Tait, Excimer laser ablation of low and high absorption index polymers. *Appl. Surf. Sci.* **96-98** (1996) 596-600.
- [39] W. Kesting, T. D. Bahners Knittel, E. Schollmeyer: Oberflächenstrukturierung polymerer Fasern durch UV-Laserbestrahlung, 14. Neue Modellvorstellungen und Simulation durch zelluläre Automaten. *Angew. Makromol. Chem.* **212** (1993) 129-146.
- [40] H. Watanabe, M. Yamamoto: Laser Ablation of Poly(ethylene terephthalate). *J. Appl. Polym. Sci.* **64** (1997) 1203-1209.
- [41] W. Wong, K. Chan, K. W. Yeung, K. S. Lau: Chemical surface modification of poly(ethylene terephthalate) by excimer irradiation of high and low intensities. *Mat. Res. Innovat.* **4** (2001) 344-349.
- [42] D. Feldmann, J. Kutzner, J. Laukemper, S. MacRobert, K. H. Welge: Mass spectroscopic studies of the ArF-laser photoablation of polystyrene. *Appl. Phys. B* **44** (1987) 81-85.
- [43] M. Tsunekawa, S. Nishio, H. Sato: Laser ablation of polymethylmethacrylate and polystyrene at 308 nm: Demonstration of thermal and photochemical mechanism by a time-of-flight mass spectroscopic study. *J. Appl. Phys.* **76** (1994) 5598-5600.
- [44] G. Gorodetsky, T. G. Kazyyaka, R. L. Melcher, R. Srinivasan: Calorimetric and acoustic study of ultraviolet laser ablation of polymers. *Appl. Phys. Lett.* **46** (1985) 828-830.
- [45] M. C. Castex, N. Biturin: Is the VUV laser ablation of polymers a pure photochemical process? *Appl. Surf. Sci.* **8114** (2002) 1-3.
- [46] M.C. Castex, N. Biturin, C. Olivero, S. Muraviov, N. Bronnikova, D. Riedel: VUV laser ablation of polymers photochemical aspect. *Appl. Surf. Sci.* **168** (2000) 175-177.
- [47] G. Hancock: Laser studies of gas-phase kinetics and photochemistry. *J. Chem. Soc. Faraday Trans.2* **84** (1988) 429-440.

- [48] R-L. Woodin, D. S. Bomse, J.-L. Beauchamp: Multiphoton dissociation of molecules with low power cw infrared lasers: collisional enhancement of dissociation probabilities. *Chem. Phys. Lett.* **63** (1979) 630-636.
- [49] T. Lippert, M. Hauer, C. R. Phipps, A. Wokaun: Fundamentals and applications of polymers designed for laser ablation. *Appl. Phys. A* **77** (2003) 259-264.
- [50] T. Lippert: Laser Application of Polymers. *Adv. Polym. Sci.* **168** (2004) 51-246.
- [51] T. Lippert, A. Yabe, A. Wokaun: Laser ablation of doped polymer systems. *Adv. Mater.* **9** (1997) 105-119.
- [52] K. P. Adhi, R. L. Owings, T. A. Railkar, W. D. Brown, A. P. Malshe: Chemical modifications in femtosecond ultraviolet (248 nm) excimer laser radiation-processed polyimide. *Appl. Surf. Sci.* **225** (2004) 324-331.
- [53] H. Niino, A. Yabe: Chemical surface modification of fluorocarbon polymers excimer laser processing. *Appl. Surf. Sci.* **96-98** (1996) 550-557.
- [54] M. Dadsetan, H. Mirzadeh, N. Sharifi-Sanjani, P. Salehian: In vitro studies of platelet adhesion on laser-treated polyethylene terephthalate surface. *J. Biomed. Mater.* **54** (2001) 540-546.
- [55] H. Mirzadeh, M. Dadsetan, N. Sharifi-Sanjani: Platelet Adhesion on Laser-Induced Acrylic Acid-Grafted Polyethylene Terephthalate. *J. Appl. Polym. Sci.* **86** (2002) 3191-3196.
- [56] P. Metayer, D. Davenas, J. M. Bureau: Ablation and carbon deposition induced by UV laser irradiation of polyamide: Application to the metallization of VIAs in high density printed circuit boards. *Nucl. Instr. Meth. B* **185** (2001) 156-162.
- [57] H. Niino, A. Yabe: Excimer laser polymer ablation: formation of positively charged surfaces and its application into the metallization of polymer films. *Appl. Surf. Sci.* **69** (1993) 1-6.
- [58] M. Charbonnier, M. Alami, M. Romand, J. P. Girardeau-Montaut, M. Afif: Laser-assisted grafting onto polycarbonate: application to metallization by chemical means. *Appl. Surf. Sci.* **109-110** (1997) 206-211.
- [59] S. Lazare, M. Bolle, A. Cros, L. Bellard: Periodic structuration of polymer surfaces with the excimer laser radiation. *Nucl. Instr. Meth. B* **105** (1995) 159-163.
- [60] B. J. Garrison, R. Srinivasan: Laser ablation of organic polymers: Microscopic models for photochemical and thermal process. *J. Appl. Phys.* **57** (1985) 2909-2914.
- [61] H. J. Booth: Recent applications of pulsed lasers in advanced materials processing. *Thin Solid Films* **453-454** (2004) 450-45.

- [62] M. Flury, A. Benatmane, P. Gérard, P. C. Montgomery, J. Fontaine: T. Engel, J. P. Schunck, E. Fogarassy, Excimer laser ablation lithography applied to the fabrication of reflective diffractive optics. *Appl. Sur. Sci.* **208-209** (2003) 238-244.
- [63] T. Lippert, T. Gerber, A. Wokaun: Single pulse nm-size grating formation in polymers using laser ablation with an irradiation wavelength of 355 nm. *Appl. Phys. Lett.* **75** (1999)1018-1020.
- [64] F. Yu, P. Li, H. Shen, S. Mathur, C.-M. Lehr, U. Bakowsky, F. Mücklich: Laser Interference Lithography as a New and Efficient Technique for Micropatterning of Biopolymer Surface. *Biomaterials* **26** (2005) 2307-2312.
- [65] F. Yu, F. Mücklich, P. Li, H. Shen, S. Mathur, C.-M Lehr, U Bakowsky: In Vitro Cell Response to Polymer Surface Micropatterned by Laser Interference Lithography. *Biomacromolecules* **6** (2005) 1160-1167.
- [66] M.C. Siebers, P.J. ter Brugge, X.F. Walboomers, J.A. Jansen: Integrins as linker proteins between osteoblasts and bone replacing materials. A critical review. *Biomaterials* **26** (2005) 137-146.
- [67] J. C. Adams: Fasin protrusion in cell interactions. *TCM* **14** (2004) 221-226.
- [68] J. R. Potts, I. D. Campbell: Fibronectin structure and assembly. *Curr. Opin. Cell Biol.* **6** (1994) 648-655.
- [69] S. A. Mitchell, N. Emmison, A. G. Shard: Spatial control of cell attachment using plasma micropatterned polymers. *Surf. Interface Anal.* **33** (2002) 742-747.
- [70] H.-H. Huang, Ch.-T Ho, T.-H. Lee, T.-L. Lee, K.-K. Liao, F.-L. Chen_ Effect of surface roughness of ground titanium on initial cell adhesion. *Biomolecular Eng.* **21** (2004) 93-97.
- [71] A. Huttenlocher, R. R. Sandborg, A. F. Horwitz: Adhesion in cell migration. *Curr. Opin. Cell Bio.* **7** (1995) 697-706
- [72] Ch. M. Sanderson, G. L. Smith: Cell motility and cell morphology: How some viruses take control. *Exp. Rev. Mol. Med.* 4 May, 1999. <http://www.expertreviews.org/99000629h.htm>.
- [73] H. Zimmermann, E. Richter, C. Reichle, I. Westphal, P. Geggier, U. Rehn, S. Rogaschewski, W. Bleiß, G.R. Fuhr: Mammalian cell traces-morphology, molecular composition, artificial guidance and biotechnological relevance as a new type of “bionanotube”. *Appl. Phys. A* **73** (2001)11-26.
- [74] P. Clark, P. Connolly, A.S. Curtis, J. A. Dow, C. D. Wilkinson: Topographical control of cell behavior: I. Simple step cues. *Development* **99** (1987) 439-448.
- [75] R. G. Harrison: The cultivation of tissues in extraneous media as a method of morphogenetic study. *Anat Rec.* **6** (1912) 182-93.

- [76] L. E. Weiss: Experiments on cell and axon orientation in vitro: the role of colloidal exudates in tissue organization. *J. Exp. Zool.* **100** (1945) 353-386.
- [77] Y. A. Rovensky, I. L. Slavnaja, J. M. Vasiliev: Behavior of fibroblast-like cells on grooved surfaces. *Exp. Cell Res.* **65** (1971)193-201.
- [78] L. Lu, L. Kam, M. Hasenbein, K. Nyalakonda, R. Bizios, A. Göpferich, J. F. Young, A. G. Mikos: Retinal pigment epithelial cell function on substrates with chemically micropatterned surfaces. *Biomaterials* **20** (1999) 2351-2361.
- [79] M. Winkelmann, J. Gold, R. Hauert, B. Kasemo, N.D. Spencer, D.M. Brunette, M. Textor: Chemically patterned, metal oxide based surfaces produced by photolithographic techniques for studying protein-and cell-surface interactions I: Microfabrication and surface characterization. *Biomaterials* **24** (2003) 1133-1145.
- [80] C.A. Scotchforda, M. Ball, M. Winkelmann, J. Vörös, C. Csucs, D.M. Brunette, G. Danuser, M. Textor: Chemically patterned, metal oxide based surfaces produced by photolithographic techniques for studying protein-and cell-surface interactions II: Microfabrication and surface characterization. *Biomaterials* **24** (2003) 1133-1145.
- [81] A. Magnani, A. Priamo, D. Pasqui, R. Barbucci: Cell behavior on chemically microstructured surfaces. *Mater. Sci. Eng. C* **23** (2003) 315–328
- [82] M. J. Dalby, M. O. Riehle, D. S. Sutherland, H. Agheli, A. S. G. Curtis: Changes in fibroblast morphology in response to nano-columnsproduced by colloidal lithography. *Biomaterials* **25** (2004) 5415-5422.
- [83] S. N. Bhatia, M. L. Yarmush, M. Toner: Controlling cell interactions by micropatterning in co-cultures: Hepatocytes and 3T3 fibroblasts. *J. Biom. Mater. Res.* **34** (1997) 189-199.
- [84] X. F. Walboomers, H. J. E. Croes, L. A. Ginse, J. A. Jansen: Growth behavior of fibroblasts on microgrooved polystyrene. *Biomaterials* **19** (1998) 1861-1868.
- [85] C. Oakley, N. A. F. Jaeger, D. M. Brunette: Sensitivity of Fibroblasts and Their Cytoskeletons to Substratum Topographies: Topographic Guidance and Topographic Compensation by Micromachined Grooves of Different Dimensions. *Exp. Cell Res.* **234** (1997) 413-424.
- [86] J. H. Fitton, B. A. Dalton, G. Beumer, G. Johnson, H. J. Griesser, J. G. Steele: Surface topography can interfere with epithelial tissue migration. *J. Biomed. Mater. Res.* **42** (1998) 245-257.
- [87] L. Lu, K. Nyalakonda, L. Kam, R. Bizios, A. Göpferich, A. G. Mikos: Retinal pigment epithelial cell adhesion on novel micropatterned surfaces fabricated from synthetic biodegradable polymers. *Biomaterials* **22** (2001) 291-297.
- [88] S. Saneinejad, M. S. Shoichet: Patterned poly(chlorotrifluoroethylene) guides primary nerve cell adhesion and neurite outgrowth. *J. Biomed. Mater. Res.* **50** (2000) 465-474.
- [89] H .G. E. Hentschel, A. van Ooyen: Dynamic mechanisms for bundling and guidance during neural network formation. *Physica A* **288** (2000) 369-379.

- [90] R. T. Tranquillo, T. S. Girton, B. A. Bromberek, T. G. Triebes, D. L. Mooradan: Magnetically oriented tissue-equivalent tubes-application to a circumferentially oriented media equivalent. *Biomaterials* **17** (1996) 349-357.
- [91] S. Lenhert, M.-B. Meier, U. Meyer, L. Chi, H. P. Wiesmann: Osteoblast alignment, elongation and migration on grooved polystyrene surfaces patterned by Langmuir-Blodgett lithography. *Biomaterials* **26** (2005) 563-570.
- [92] H. Liao, A.-S. Andersson, D. Sutherland, S. Petronis, B. Kasemo, P. Thomsen: Response of rat osteoblast-like cells to microstructured model surfaces in vitro. *Biomaterials* **24** (2003) 649-654.
- [93] M. E. Hasenbein, T. T. Andersen, R. Bizios: Micropatterned surfaces modified with select peptides promote exclusive interactions with osteoblasts. *Biomaterials* **23** (2002) 3937-3942.
- [94] P. Clark, P. Connolly, A. S. G. Curtis, J. A. T. Dow, and C. D. W. Wilkinson: Topographical control of cell behavior II: Multiple grooved substrata. *Development* **99** (1989) 439-448.
- [95] P. Clark, P. Connolly, A. S. G. Curtis, J. A. T. Dow, C. D. W. Wilkinson: Cell guidance by ultrafine topography in vitro. *J. Cell Sci.* **99** (1991) 73-77.
- [96] A. Webb, P. Clark, J. Skepper, A. Compston, A. Wood: Guidance of oligodendro-cytes and their progenitors by substratum topography. *J. Cell Sci.* **108** (1995) 2747-2760.
- [97] E. Eisenbarth, J. Meyle, W. Nachtigall, J. Breme: Influence of the surface structure of titanium materials on the adhesion of fibroblasts. *Biomaterials* **17** (1996) 1399-1403.
- [98] S.A. Mitchell, A.H.C. Poulsson, M.R. Davidson, N. Emmison, A.G. Shard, R.H. Bradley: Cellular attachment and spatial control of cells using micro-patterned ultra-violet/Ozone treatment in serum enriched media. *Biomaterials* **25** (2004) 4079-4086.
- [99] A. S. Blawas, W. M. Reichert: Protein Patterning. *Biomaterials* **19** (1998) 595-609.
- [100] C. D. McFarland, C. H. Thomas, C. DeFilippis, J. G. Steele, K. E. Healy: Protein adsorption and cell attachment to patterned surfaces. *J. Biomed. Mat. Res.* **49** (2000) 200-210.
- [101] M. E. Nimn: Review: polypeptide growth factors: targeted delivery systems. *Biomaterials* **18** (1997)1201-25.
- [102] M. Mrksich, C. S. Chen, Y. Xia, L. E. Dike, D. E. Ingber, G. M. Whitesides: Controlling cell attachment on contoured surfaces with self-assembled monolayers of alkanethiolates on gold. *PNAS* **93** (1996) 10775-10778.
- [103] M. J. Weber: *Handbook of Lasers*, CRC, 2001.
- [104] Nd:YAG laser Manuel, Quanta-Ray Pro-Series, Spectra-Physics Laser Inc. 1998.

- [105] B. Bowe, V. Toal: White light interferometric surface profiler, *Opt. Eng.* **37** (1998) 1796-9.
- [106] T. Muskat: Dissertation, Christian-Albrechts-Universität zu Kiel, 2004.
- [107] P. Laurens, M. Ould Bouali, F. Meducin, B. Sadras: Characterization of modifications of polymer surfaces after excimer laser treatments below the ablation threshold: *Appl. Surf. Sci.* **154-155** (2000) 211-216.
- [108] S. Küper, J. Brannon, K. Brannon: Threshold behavior in polyimide photo-ablation: single-shot rate measurements and surface-temperature modelling. *Appl. Phys. A* **56** (1993) 43-50.
- [109] S. Lazare, R. Srinivasan: Surface properties of poly(ethylene terephthalate) films modified by far-ultraviolet radiation at 193 nm (laser) and 185 nm (low intensity). *J. Phys. Chem.* **90** (1986) 2124-2131.
- [110] S. Baudach, J. Bonse, J. Kruger, W. Kautek: Ultrashort pulse laser ablation of polycarbonate and polymethylmethacrylate. *Appl. Surf. Sci.* **154-155** (2000) 555-560
- [111] R. E. Russo, X. L. Mao, H. C. Liu, J. H. Yoo, S. S. Mao: Time-resolved plasma diagnostics and mass removal during single-pulse laser ablation. *Appl. Phys. A* **69** (1999) 887-894.
- [112] S. S. Mao, X. Mao, R. Greif, R. E. Russo: Initiation of an early-stage plasma during picosecond laser ablation of solids. *Appl. Phys. Lett.* **77** (2000) 2464-2466.
- [113] P. Lemoine, K. Cazzini, LT. McGovern, W. J. Blau, P. Bätz, C. Ziegler, W. Göpel: X-ray photoelectron spectroscopy of KrF laser-irradiated polycarbonate films. *Chem. Phys. Lett.* **220** (1994) 177-18.
- [114] B. Jang, C. A. Wilkie: The thermal degradation of bisphenol a polycarbonate in air. *Thermochim Acta* **426** (2005) 73-84.
- [115] P. T. Ohara, R. C. Buck: Contact guidance in vitro. A light, transmission, and scanning electron microscopic study. *Exp. Cell Res.* **121** (1979) 235-249.
- [116] A. F. von Recum, T. G. van Kooten: The influence of micro-topography on cellular response and the implications for silicone implants. *J. Biomater. Sci. Polym. Ed.* **7** (1995) 181-198.
- [117] Y. A. Rovensky, SI. L. Lavnaja, J. M. Vasiliev: Behavior of fibroblast-like cells on grooved surfaces. *Exp. Cell Res.* **65** (1971) 193-201.
- [118] J. Meyle, H. Wolburg, A. F. von Recum: Surface micromorphology and cellular interactions. *J. Biomater. Appl.* **7** (1993) 362-374.
- [119] P. Li, U. Bakowsky, F. Yu, C. Loebach, F. Muecklich, C.-L. Lehr: Laser ablation patterning by interference induces directional cell growth. *IEEE T. Nanobiosci.* **2** (2003) 138-145.

- [120] J.-L. Dewez, J.-B. Lhoest, E. Detrait, V. Berger, C.C. Dupont-Gillain, L.-M. Vincent, Y.-J. Schneider, P. Bertrand, P. G. Rouxhet: Adhesion of mammalian cells to polymer surfaces: from physical chemistry of surfaces to selective adhesion on defined patterns. *Biomaterials* **19** (1998) 1441-1445
- [121] X. F Walboomers, J. A. Jansen: Early spreading events of fibroblasts on microgrooved substrates. *J. Biomed. Mater. Res.* **51** (2000) 529-534.
- [122] B. Wojciak-Stothard, A. Curtis, W. Monaghan, K. MacDonald, C. Wilkinson: Guidance and Activation of Murine Macrophages by Nanometric Scale Topography. *Exp. Cell Res.* **223** (1996) 426-435.
- [123] A. I. Teixeira, G. A. Abrams, P. J. Bertics, Ch. J. Murphy, P. F. Nealey: Epithelial contact guidance on well-defined micro- and nanostructured substrates. *J. Cell Sci.* **116** (2003) 1881-1892.
- [124] X. F. Walboomers, H. J. E. Croes, L. A. Gensel, J. A. Jansen: J. Contact guidance of rat fibroblasts on various implant materials. *J. Biomed. Mater. Res.* **47** (1999) 204-212.
- [125] F. R. Pu, R. L. Williams, T. K. Markkula, J. A. Hunt: Expression of leukocyte–endothelial cell adhesion molecules on monocyte adhesion to human endothelial cells on plasma treated PET and PTFE in vitro. *Biomaterials* **23** (2002) 4705-4718.
- [126] J. Guidollet, E. Chignier, R. Pillot, O. Gayet, J. MacGregor, P. Louisot: Enhanced expression of P-selectin (CD62/P) by endothelial cells seeded onto synthetic arterial prostheses (PET, Dacron) is correlated with leukocyte interactions. *J. Biomed. Mater. Res.* **44** (1999)156-161.
- [127] C. A. van Blitterswijk, D. Bakker, S. C. Hesselting, H. K. Koerten: Reactions of cells at implant surfaces. *Biomaterials* **12** (1991) 187-193.
- [128] W. G. Brodbeck, Y. Nakayama, T. Matsuda, E. Colton, N. P. Ziats, J. M. Anderson: Biomaterial surface chemistry dictates adherent monocyte/macrophage cytokine expression in vitro. *Cytokine* **18** (2002) 311-319.